Thermal-Hydraulic Analysis of Once-Through Steam Generators

EPRI

Keywords:
Thermal Hydraulic
Steam Generator
Computer Code

EPRI NP-1431
Project S131-1
Final Report
June 1980

Prepared by
The Babcock & Wilcox Company
Alliance, Ohio

ELECTRIC POWER RESEARCH INSTITUTE

Thermal-Hydraulic Analysis of Once-Through Steam Generators

NP-1431
Research Project S131-1

Final Report, June 1980
Work Completed, September 1979

Prepared by

THE BABCOCK & WILCOX COMPANY
Alliance Research Center
Research & Development Division
Alliance, Ohio 44601

Principal Investigators
R. T. Fortino
W. J. Oberjohn
J. G. Rice
D. K. Cornelius

Prepared for

Electric Power Research Institute
3412 Hillview Avenue
Palo Alto, California 94304

EPRI Program Manager
G. Hetsroni

EPRI Project Manager
D. A. Steininger

Steam Generator Project Office
Nuclear Power Division

ORDERING INFORMATION

Requests for copies of this report should be directed to Research Reports Center (RRC), Box 50490, Palo Alto, CA 94303, (415) 965-4081. There is no charge for reports requested by EPRI member utilities and affiliates, contributing nonmembers, U.S. utility associations, U.S. government agencies (federal, state, and local), media, and foreign organizations with which EPRI has an information exchange agreement. On request, RRC will send a catalog of EPRI reports.

NOTICE

Prepared by
The Babcock & Wilcox Company
Alliance, Ohio

EPRI PERSPECTIVE

PROJECT DESCRIPTION

It is becoming apparent in steam generator evaluation that local thermal-hydraulic conditions within the tube bundle play a significant role in some forms of damage (e.g., denting, tubesheet sludge buildup resulting in tube wastage and cracking, and erosion-wear) that have occurred in steam generators. In addition, local conditions of velocity and density need to be determined to evaluate the tube bundle design with respect to flow-induced tube vibration and consequent fretting, wear, and fatigue of the tubes over the 40-year design life of the steam generator. EPRI Research Project S131-1, for which this is a final report, is one of several Steam Generator Project Office projects that evaluate currently available computer codes for calculating thermal-hydraulic conditions in steam generators.

PROJECT OBJECTIVES

This report addresses a Babcock & Wilcox Company proprietary three-dimensional, thermal-hydraulic computer code called THEDA-1, used to model once-through steam generator (OTSG) designs unique to this company. Two once-through steam generator models (those at Three Mile Island-2 and Davis Besse-2) are analyzed. Analysis is performed to determine the sensitivity of the output to specific variations of input parameters. Additionally, the results are used to evaluate the performance of existing steam generator designs.

PROJECT RESULTS

In general, THEDA-1 predicts physically realistic and internally consistent trends of both overall and local steam conditions; however, enthalpy calculated for untubed regions of the steam generator is strongly influenced by the two-phase flow correlation chosen and by details of steam generator modeling. Despite these uncertainties, calculations show a beneficial effect on local enthalpy from blocking flow in the untubed regions. This study indicates several areas in which additional work would improve the accuracy and efficiency of the

THEDA-1 code. More importantly, because variations in modeling detail and correlation uncertainties can affect accuracy for local regions of a steam generator, THEDA-1 predictions should be verified by comparison with experimental data. This report should be of interest to steam generator designers, utility personnel responsible for steam generator reliability, and persons developing thermal-hydraulic codes.

D. A. Steininger, Project Manager
Steam Generator Project Office
Nuclear Power Division

ABSTRACT

The objective of this project is to provide EPRI with the best currently available estimates of the steady-state local thermal/hydraulic conditions for The Babcock and Wilcox Once-Through Steam Generator (OTSG). The sensitivity of the estimates to correlation uncertainties is also provided.

The best estimate analyses and sensitivity studies were carried out using a developmental multi-dimensional computer code, THEDA-1, which solves the non-linear conservation equations of mass, momentum, and energy using finite-difference techniques. The tube bundle and tube support plates are represented as a porous media with distributed resistance to flow and heat transfer.

Generally speaking, THEDA-1 provides physically realistic and internally consistent predictions of the trends in both overall and local steam conditions. The OTSG behaves essentially as a one-dimensional counter-current flow heat exchanger. Radial and circumferential gradients are significant only at the inlet and outlet and near untubed regions.

Overall performance parameters, such as outlet steam temperature, are only slightly affected by correlation uncertainties. Local conditions in untubed regions are more significantly affected, particularly by uncertainties in the two-phase flow void fraction correlations.

Blank Page

CONTENTS

CONTENTS (Cont'd)

ILLUSTRATIONS

ILLUSTRATIONS (Cont'd)

ILLUSTRATIONS (Cont'd)

ILLUSTRATIONS (Cont'd)

TABLES

Blank Page

NOMENCLATURE

Symbol	Description	Units
a	finite difference coefficient	lbm/sec
A	area	ft^2
b	finite difference source term including pressure gradient term	lbm-ft/sec^2*
b'	finite difference source term excluding pressure gradient term	lbm-ft/sec^2*
Bo	boiling number	
C_o	concentration parameter	
C_l	mixing coefficient	
C_p	specific heat	Btu/lbm-°F
d	tube outer diameter	ft
d_t	tube inner diameter	ft
D_r	hydraulic diameter of a tube support plate restriction	ft
D_h	tube bundle hydraulic diameter	ft
D_z	diffusion coefficient at control volume face z	lbm/sec
f	fine grid loss coefficient correction factor	
f'	cross-flow friction factor	
f_x	axial friction factor	
F	Chen's Reynolds number factor	
g	acceleration due to gravity =	32.2 ft/sec^2
g_c	gravitational constant =	32.2 lbm-ft/lbf-sec^2
G	mass velocity	lbm/hr-ft^2
h	enthalpy	Btu/lbm
h	heat transfer coefficient	Btu/hr-ft^2-°F
h_g	enthalpy of saturated vapor	Btu/lbm
h_L	enthalpy of saturated liquid	Btu/lbm
h_{Lg}	latent heat of fusion	Btu/lbm
h_{mac}	Chen's macroscopic heat transfer coefficient	Btu/hr-ft^2-°F

*Units for the momentum equations. The units are Btu/sec for the energy equation.

Symbol	Description	Units
h_{mic}	Chen's microscopic heat transfer coefficient	Btu/hr-ft^2-°F
h_{ex}	average enthalpy over an exit region	Btu/lbm
h_n	exit enthalpy for control volume n	Btu/lbm
j	total volumetric flux	ft/sec
j_g	volumetric flux of vapor	ft/sec
j_L	volumetric flux of liquid	ft/sec
j_{gL}	drift flux	ft/sec
k	Single phase thermal conductivity	Btu/hr-ft-°F
K	form loss coefficient	
K_S	ratio of mass of water flowing in the homogeneous mixture to total mass of water flowing	
ℓ	tube support plate thickness	ft
$\dot{m}$	mass flow rate	lbm/sec
N	total number of main control volumes	
N_ϕ	total number of momentum control volumes for variable ϕ	
Nu	Nusselt Number	
P	pressure	psia
P*	pressure at the previous iteration	lbm/ft-sec^2
P'	pressure correction	lbm/ft-sec^2
P_s	tube heated perimeter	ft
P_{sat}	saturation pressure	psia
ΔP_{sat}	difference between saturation pressure at the tube wall temperature and the saturation pressure	lbf/ft^2
Pr	Prandtl Number	
q	heat flux	Btu/hr-ft^2
Q	total heat transfer	Btu/hr
$\underline{Q}$	volumetric flow rate	ft^3/sec
r	radial dimension	ft

NOMENCLATURE (Cont'd)

Symbol	Description	Units
Δr	radial increment	ft
r_i	tube inner radius	ft
r_o	tube outer radius	ft
R	resistance	$lbm/ft^2\text{-}sec^2$
$\overline{R}$	average residual	
R_p	continuity residual for main control volume p	lbm/sec
Re	Reynolds Number	
s	characteristic subchannel dimension	ft
S	slip ratio	
S	Chen's suppression factor	
S_ϕ	source term for conservation equation variable ϕ	$lbm/ft^2\text{-}sec^2$ **
t_p	tube pitch	ft
T	temperature	°F
ΔT_{sat}	difference between the tube wall temperature and saturation temperature	°F
U	axial velocity	ft/sec
U_i	U, V, and W velocities	ft/sec
U_i^*	U, V, and W velocities obtained with pressure field P*	ft/sec
U_i'	U, V, and W velocity corrections	ft/sec
$\overline{U}$	average velocity in adjacent subchannels	ft/sec
$\underline{U}$	velocity vector	ft/sec
$\lvert\underline{U}\rvert$	velocity vector magnitude	ft/sec
$\overline{U}_{gj}$	weighted mean drift velocity	ft/sec
U_{gL}	relative velocity between phases	ft/sec
U_t	overall heat transfer coefficient	$Btu/hr\text{-}ft^2\text{-}°F$
U_{tr}	terminal rise velocity	ft/sec
V	radial velocity	ft/sec
W	circumferential velocity	ft/sec

**Units for the momentum equations. For S_h the units are $Btu/ft^3\text{-}sec$.

Symbol	Description	Units
x	axial dimension	ft
Δx	axial increment	ft
X_t	ratio of transverse pitch to tube diameter	
$y\ (P_{sat})$	parameter in Chen's nucleate boiling correlation	
Δz	Δx, Δr, or $r\Delta\theta$	ft
GREEK SYMBOLS		
α	void fraction	
α_H	homogeneous void fraction	
β	porosity	
γ	Thom void fraction correlation parameter	
Γ_t	eddy diffusivity	lbm/ft-sec
θ	circumferential dimension	radians
$\Delta\theta$	circumferential increment	radians
μ	viscosity	lbm/ft-sec
μ_t	eddy viscosity	lbm/ft-sec
ρ	density	lbm/ft^3
ρ_α	volume weighted density	lbm/ft^3
ρ_m	momentum equation density	lbm/ft^3
$\delta\rho$	$\rho - \rho_m$	lbm/ft^3
σ	surface tension	lbf/ft
ϕ	variable ϕ equal to U, V, W, h, or P	
$\overline{\phi}$	value of variable ϕ at a control volume face	
ϕ_{fo}^2	two-phase friction multiplier	
χ	flow quality	
χ_{tt}	Martinelli parameter	

Symbol	Description
SUBSCRIPTS	
b	bundle
B	bleed
DO	dryout
ex	exit
fr	friction
FB	film boiling
FGSP	fine grid support plate
FW	feedwater
g	vapor phase (evaluated at saturation conditions in THEDA-1)
L	liquid phase (evaluated at saturation conditions in THEDA-1)
ℓo	liquid only
m	tube metal
max	maximum
n	control volumes
NB	nucleate boiling
p	point p
p	primary side
r	restriction
r	radial
RSP	regular support plate
s	secondary side
S	steam
SH	superheat
SG	steam generator
t	tube
tsp	tube support plate
x	axial
z	point z
z	control volume face between point p and point z
θ	circumferential

SUMMARY

BACKGROUND

The proprietary computer code THEDA-1 has been developed by Babcock & Wilcox (B&W) to calculate thermal/hydraulic conditions within the B&W Once-Through Steam Generator (OTSG). THEDA-1 is based on a quasi-continuum model of the three-dimensional, two-phase flow of the secondary or shell side fluid in the OTSG. The tube bundle and the tube support plates are represented as a porous media with distributed resistance to flow and heat transfer. With this approach, it is possible to model a 15,000 tube OTSG including local features such as tube support plates and untubed inspection lanes.

This report presents the results of best estimate analyses of the Three Mile Island Unit 2 (TMI-2) and the Davis-Besse Unit 2 (DB-2) steam generators. These steam generators were selected because they represent the range of geometrical features found in B&W OTSGs. The major difference in geometry is that untubed regions are totally blocked to axial flow in the DB-2 OTSG at each tube support plate, while the TMI-2 support plates only partially block the flow. The effectiveness of blocking the flow can be evaluated by comparing the performance of the TMI-2 and DB-2 steam generators.

Three-dimensional thermal/hydraulic analyses techniques are relatively new and have not been verified by comparison with experimental data. In fact, almost no data are available that represents the two-phase flow conditions within an OTSG. Therefore, a study was also conducted to determine how sensitive TMI-2 predictions are both to correlation uncertainties and to the number of control volumes used in the model. The results should be helpful for establishing the degree of uncertainty associated with the predictions of particular overall performance characteristics of the TMI-2 OTSG such as outlet steam superheat. They can also be used as guidelines for selecting conservative correlations for worst case analyses and for selecting the number of control volumes required to adequately model local features of the OTSG.

THEDA-1 numerically solves the non-linear conservation equations of mass, momentum, and energy using finite-difference techniques. For each analysis, the rate of convergence of the solutions was examined as well as the magnitude of the residuals of the finite-difference equation solutions. As part of the sensivity study, the predicted response of the steam generator thermal/hydraulics to positive and negative correlation perturbations was also examined to determine if THEDA-1 predictions are reasonable and consistent. Generally speaking, THEDA-1 was found to provide physically realistic and internally consistent predictions of both overall and local steam conditions.

STEAM GENERATOR DESCRIPTION

The B&W OTSG (Figure 1) is a vertical, straight-tube, straight-shell, once-through counterflow heat exchanger with shell side boiling. Primary reactor coolant enters the steam generator through a nozzle in the upper head, flows down through more than 15,000 Alloy 600 tubes, and exits the bottom head through two outlet nozzles. On the secondary side, subcooled feedwater is sprayed downward into the annulus between the shell and the tube bundle shroud where it is heated to saturation by direct contact with steam aspirated from the tube bundle. The saturated feedwater enters the bottom of the tube bundle where nucleate boiling begins. After reaching 100% quality at about the mid-bundle elevation, the steam is superheated in the upper half of the bundle, flows down through the steam annulus, and exits through two steam outlet nozzles.

The tubes are located on a triangular pitch and the spacing between tubes is maintained along the length of the bundle by the tube support plates. The plates support each tube at three equally spaced points around the circumference while allowing most of the tube surface to be contacted by the secondary fluid.

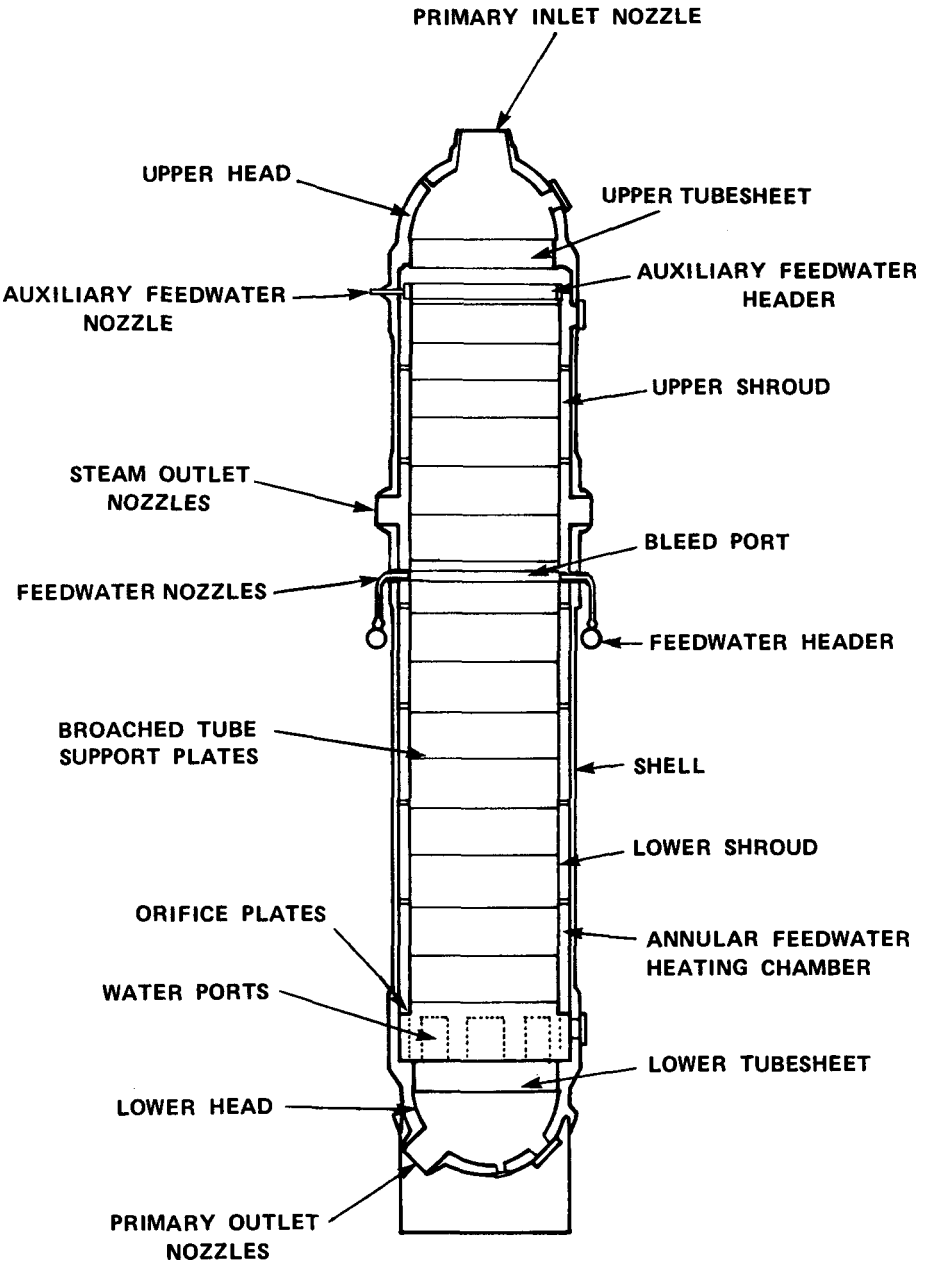

FIGURE 1 177 SERIES ONCE–THROUGH STEAM GENERATOR

There are two differences between the TMI-2 and DB-2 steam generators which affect local steam conditions (Figures 2 and 3):

- The approximately 0.2-inch gap between the tube support plate and the shroud is open to flow (except for the bottom and top support plate) for TMI-2 while this gap is blocked at every support plate for DB-2.

- TMI-2 has one radial lane of tubes omitted to provide an inspection lane. All tube supports were drilled and broached in the inspection lane. DB-2 is fully tubed (no inspection lane) except for an approximately circular lane of tubes omitted at the manway cover. However, the holes in the tube support plates at this location were omitted providing a flow blockage at each support plate.

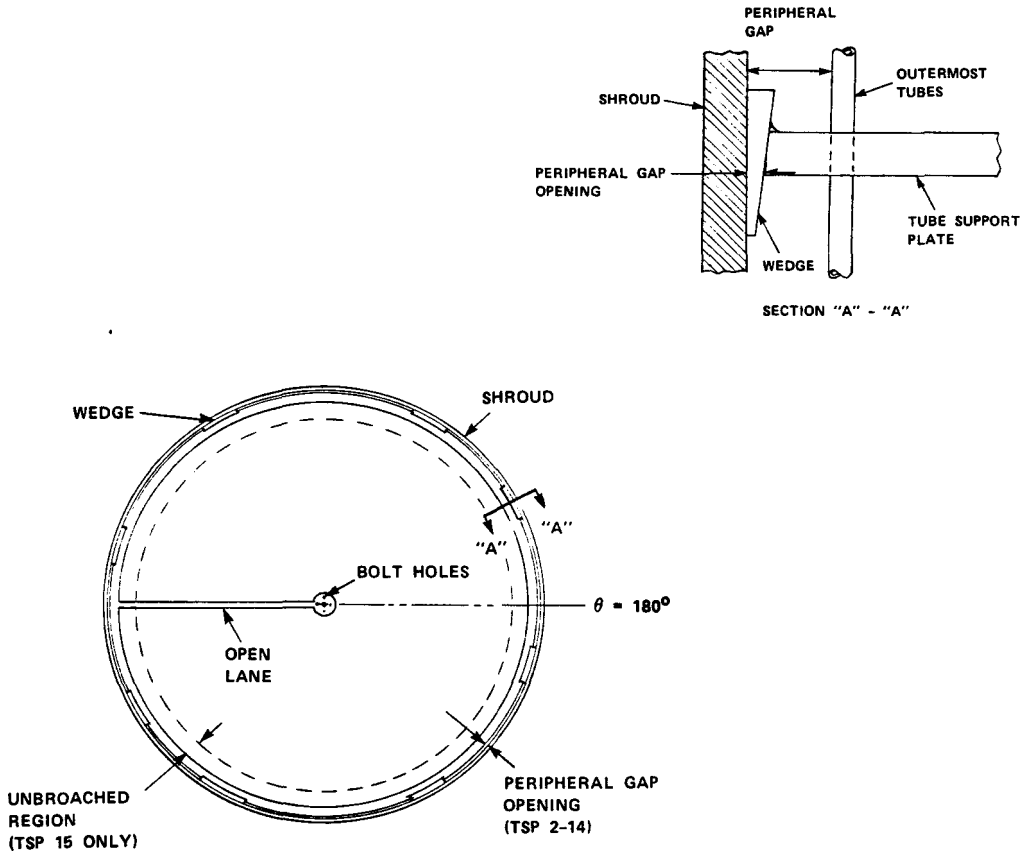

FIGURE 2 TMI–2 OTSG CROSS–SECTION

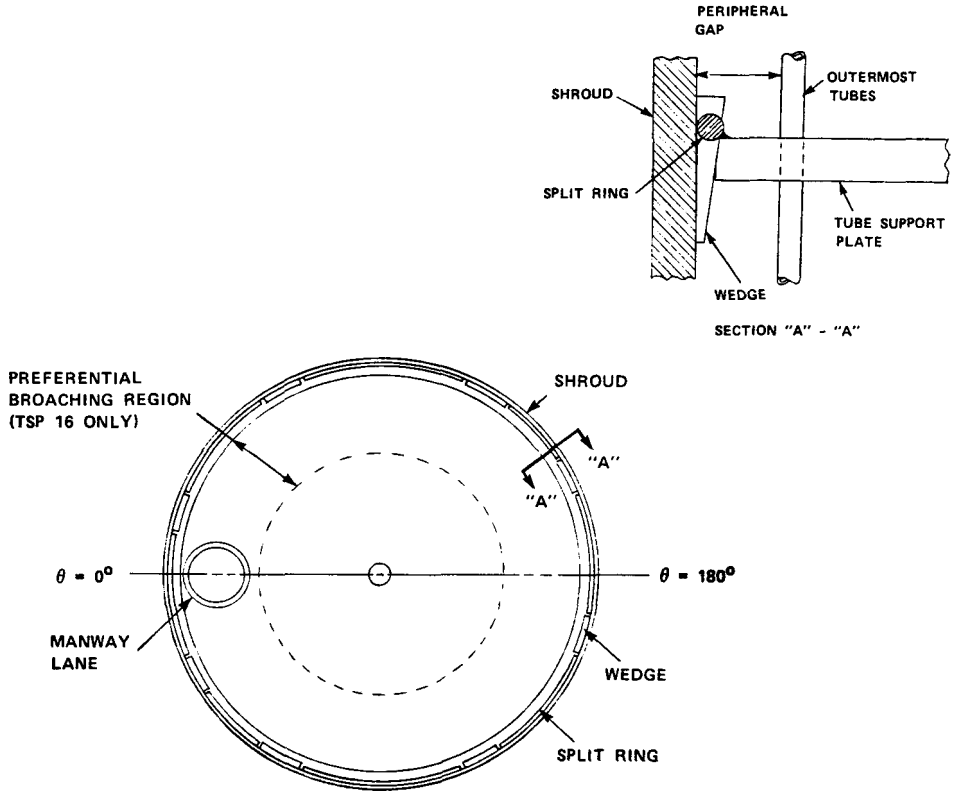

FIGURE 3 DB–2 OTSG CROSS–SECTION

BEST ESTIMATE ANALYSES

For the best estimate analyses, both the TMI-2 and DB-2 OTSGs were modeled in three dimensions so that the TMI-2 inspection lane and the DB-2 manway cover lane could be represented. The control volume sizes were varied so that larger control volumes were used to represent the tube bundle and smaller control volumes to represent the untubed lanes, the tube support plates, and the untubed peripheral gap between the tube bundle and the shroud. Steam conditions were calculated at 7260 points for TMI-2 and at 8580 points for DB-2. Performance was predicted at three load levels -- 15%, 67%, and 100%. These represent the nominal range of automatically controlled operating conditions.

Table 1 presents the specified operating conditions for each steam generator and also the THEDA-1 predictions of outlet steam temperature, secondary side pressure drop, aspirated steam flow, and primary outlet temperature.

Figure 4 compares lines of constant quality for TMI-2 and DB-2 at 100% load.

TABLE 1

OTSG OVERALL PERFORMANCE

	THREE MILE ISLAND UNIT 2			DAVIS-BESSE UNIT 2		
	% of 2787 MWT			% of 2788 MWT		
	15%	67%	100%	15%	67%	100%
Primary Side						
Inlet temperature, °F	586	599	607.5	586	600	608.6
Inlet pressure, psia	2200	2200	2200	2200	2200	2200
Flow rate, 10^6 lbm/hr	68.95	68.95	68.95	65.65	65.65	65.65
Outlet temperature, °F*	577.4	564.4	556.9	576.1	563.6	555.6
Secondary Side						
Feedwater temperature, °F	282	420	466	282	425	465
Steam pressure, psia	900.5	909.3	924.9	885.7	902.5	925
Steam flow rate, 10^6 lbm/hr	0.80	3.75	5.916	0.865	3.76	5.95
Outlet steam temperature, °F*	585.5	595.0	593.2	585.6	596.9	598.4
Secondary pressure drop, psia*	1.08	6.44	12.2	1.24	7.93	15.3
Bleed flow rate, 10^6 lbm/hr*	0.309	0.756	0.946	0.325	0.667	0.803

*THEDA-1 predictions

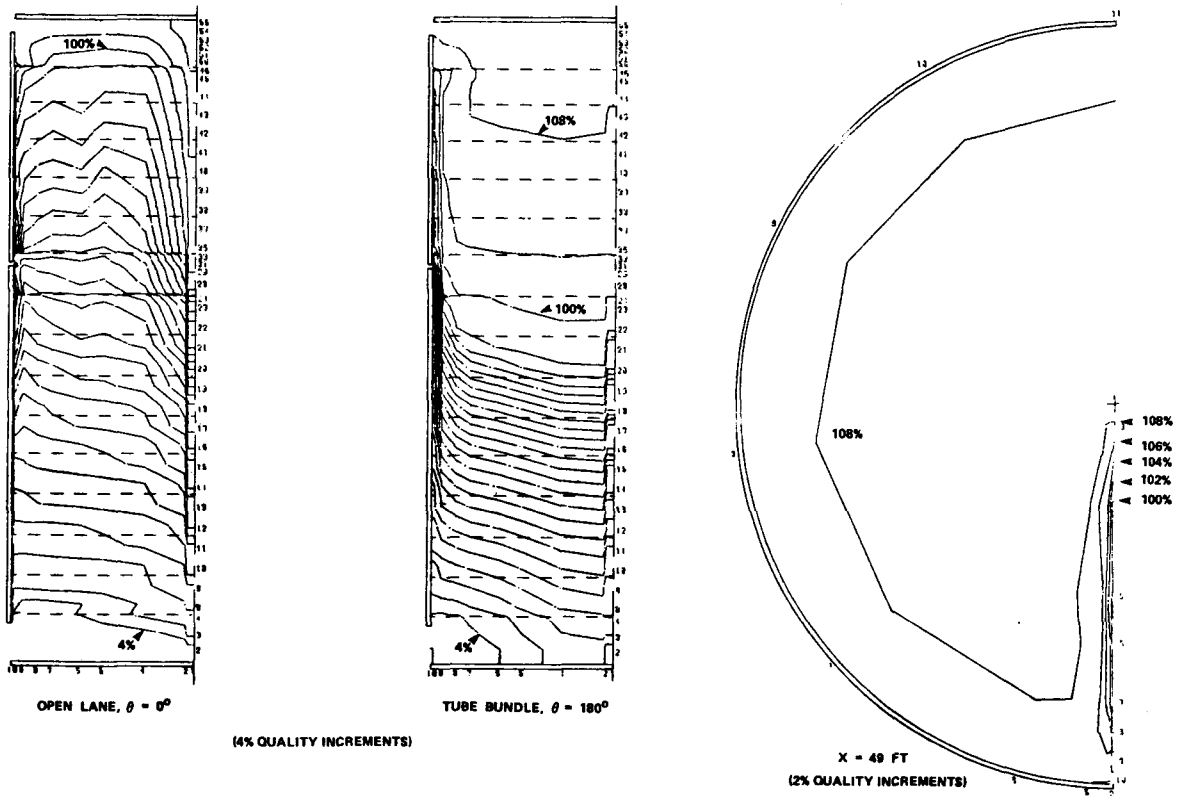

TMI-2 100% POWER QUALITY CONTOURS

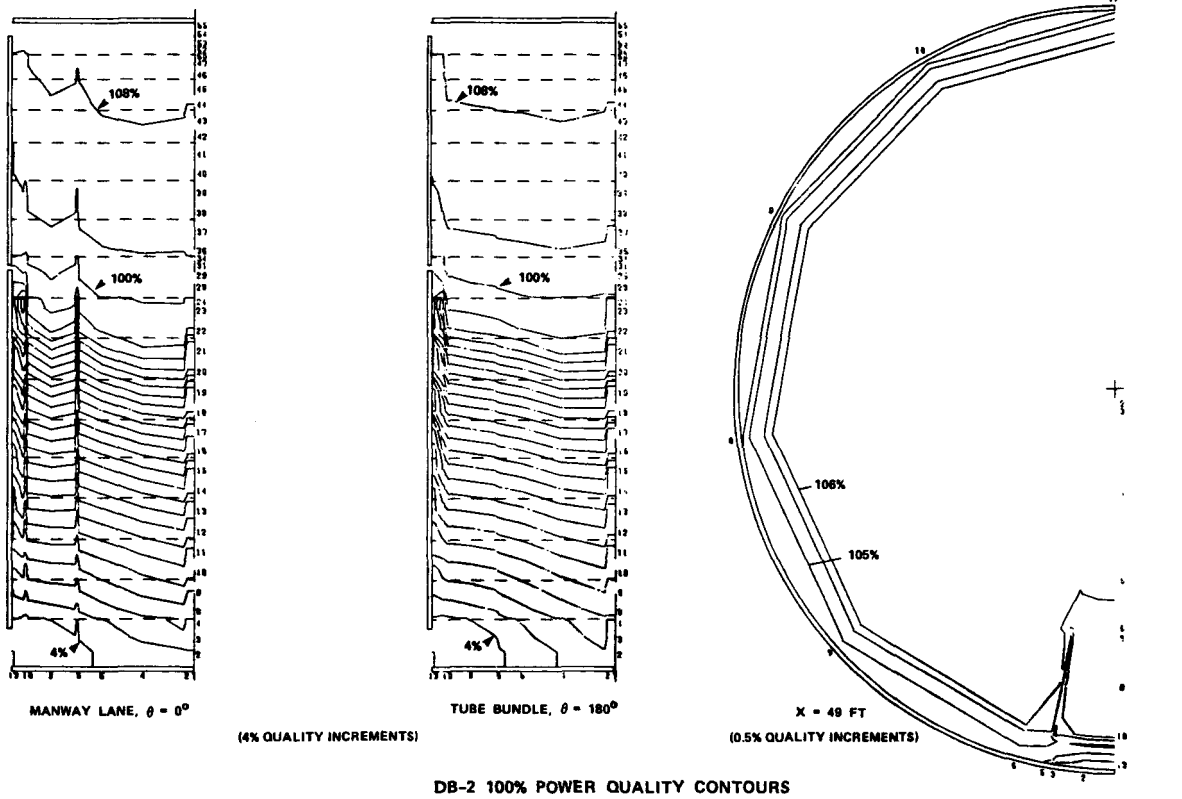

DB-2 100% POWER QUALITY CONTOURS

FIGURE 4 COMPARISON OF TMI–2 AND DB–2 QUALITY CONTOURS

The most significant result of the best estimate analyses is the variation in local steam conditions caused by untubed regions. As shown by Figure 4, the predicted steam quality in the TMI-2 inspection lane is significantly lower than the quality in the tube bundle at the same elevation. The steam quality in the TMI-2 untubed peripheral gap is also significantly lower than bundle quality. However, most of this lower quality steam is discharged to the feedwater annulus at the bleed port elevation. On the other hand, the blockages at the tube support plate minimize the effect of the DB-2 untubed periphery and manway cover lane.

The area of the untubed regions is relatively small and the lower steam quality in these areas has a minor effect on outlet steam temperature (Table 1). TMI-2 and DB-2 steam temperatures are about equal at 15% and 67% load and at 100% load, the predicted TMI-2 steam superheat is about 58°F -- only 5°F lower than for DB-2.

SENSITIVITY STUDY

The conservation equations in THEDA-1 model the steam-water mixture in the OTSG as a homogeneous fluid except that the gravity term in the momentum equation is based on an empirical void fraction model rather than the void fraction for a homogeneous mixture of steam and water. Empirical correlations are also required to complete the description of flow and heat transfer. They are used to calculate the distributed fluid flow and heat transfer resistances, the void fraction, and the turbulent diffusion coefficients for heat and momentum transfer between control volumes. In many cases, the correlations were developed from one-dimensional flow data and are applied in THEDA-1 for three-dimensional calculations. The uncertainty involved in this procedure was evaluated by perturbing a correlation and noting the effect on local and overall steam conditions.

The accuracy of the finite-difference solution is also affected by the number of control volumes used to model the steam generator. Economic considerations, as well as computer memory size, limit the number of control volumes. Runs were performed to determine the number of axial and radial nodes required to obtain accurate predictions.

All of the sensitivity runs were based on the TMI-2 steam generator geometry and 100% load operating conditions. The radial inspection lane was not included so that the geometry would be symmetrical about the centerline. This reduced the cost of the computations compared to the 3-D best estimate. The results are

summarized in Table 2. Presented are outlet steam temperature (T_S), total bundle pressure drop (ΔP), steam bleed flow ($\dot{m}_B$), and dryout height for the nominal TMI-2 100% load calculation, based on the "best estimate" correlations. Also shown are the changes that resulted from perturbations in seven of these correlations. In general, the changes had an insignificant effect on overall performance. The exception occurred when the Chen boiling heat transfer correlation was substituted for the B&W proprietary correlation developed from laboratory data at OTSG conditions. The 15°F lower steam temperature predicted using the Chen correlation is inconsistent with the measured steam temperature of operating OTSGs and indicates the importance of using a boiling correlation based on data at OTSG conditions. Overall performance was only slightly affected by the number of axial and radial nodes.

TABLE 2

NOMINAL RESULTS AND PERTURBATIONS*

	T_S (°F)	ΔP (psia)	$\dot{m}_B$ (10^6 lbm/hr)	Dryout Height (ft)
Nominal	593.4	10.4	0.9314	25.376
Thom Void Fraction	-1.0	-1.0	0.126	-0.115
Homogeneous Void Fraction	-1.9	-1.4	0.187	-0.332
Turbulent Mixing x 0.2	-0.3	0.0	0.007	-0.023
Turbulent Mixing x 5.0	0.4	0.0	-0.037	-0.023
Turbulent Mixing x 15.0	1.3	0.1	-0.090	-0.159
Turbulent Mixing x 50.0	2.3	0.4	-0.156	0.027
Tube Support Plate K x 0.75	0.2	-1.0	-0.022	0.085
Tube Support Plate K x 1.25	-0.2	1.0	0.019	-0.127
Cross-Flow Resistance Coeff. x 0.5	0.3	-0.6	-0.034	-0.023
Cross-Flow Resistance Coeff. x 3.0	-0.5	1.9	0.081	-0.166
Chen Nucleate Boiling Coeff.	-15.6	0.2	0.313	8.573
B&W Proprietary Coeff. x 0.5	-1.8	0.1	0.039	1.846
Steam Convection Coeff. x 0.9	-2.0	0.0	-0.0011	-0.103
Steam Convection Coeff. x 1.1	2.7	0.1	-0.0007	0.054
Dryout Quality = 0.92	-1.5	0.0	0.002	-0.506
Dryout Quality = 0.98	1.4	0.1	-0.004	0.301
41 Axial Nodes	-1.2	0.0	0.014	0.682
115 Axial Nodes	0.6	0.3	-0.033	-0.319
11 Radial Nodes	0.3	0.0	-0.011	0.011
21 Radial Nodes	0.5	0.1	0.023	0.181

*The perturbation is defined as the change case minus the nominal case.

Local steam conditions in untubed regions of the steam generator were affected to a larger extent than the overall performance which is dominated by the performance of the tube bundle. For the TMI-2 steam generator, the flow and steam quality in the untubed regions appears to be affected most strongly by the void fraction model used to calculate the two-phase fluid density appearing in the buoyancy term of the axial momentum equation. This effect is shown in Figure 5 which indicates that steam quality in the peripheral gap between the bundle and the shroud is about 12% lower when the homogeneous void fraction model is used in place of the "best estimate" or nominal correlation. It was found that the most significant terms in the axial momentum balance for control volumes in the two-phase region of the untubed gap are the gravity head and the axial pressure gradient. The steam quality in the peripheral gap can be estimated with reasonable accuracy by determining the quality that is necessary to provide a gravity head gradient in the gap that balances the tube bundle axial pressure drop gradient (exclusive of the tube support plate pressure drop). This indicates that uncertainties in modeling the two-phase flow tube bundle pressure drop and the two-phase density in both tubed and untubed regions can affect the predicted quality in the unblocked peripheral gap of the TMI-2 steam generator.

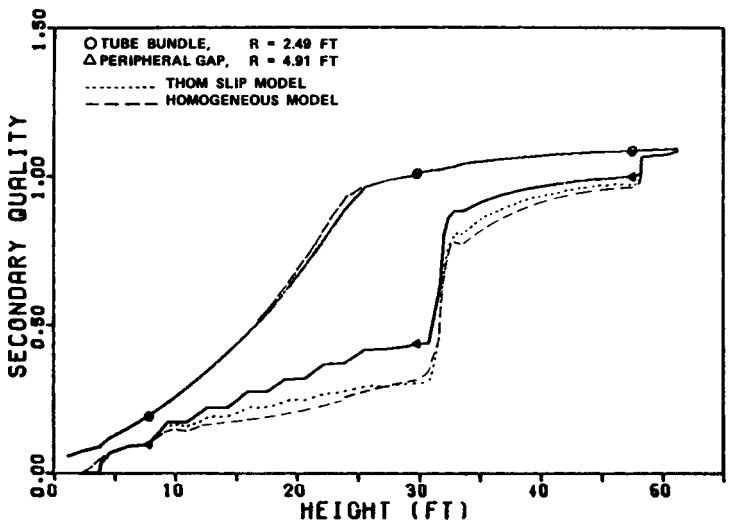

FIGURE 5 EFFECT OF CHANGES IN VOID FRACTION CORRELATION ON QUALITY PROFILES

A limited sensitivity study of conditions in an unblocked radial lane was also conducted. The TMI-2 radial inspection lane was modeled as a circumferential open lane (COL) thus maintaining axial symmetry. Since a large number of nodes in the circumferential direction were not required, as would be for a radial lane model, additional axial nodes were available to model the tube support plates. Figure 6 shows that changes in the void fraction correlation have an effect on quality in the COL similar to that in the peripheral gap. The steam quality in the COL was compared (Figure 7) with steam quality at the mid-radius of the TMI-2 radial lane as predicted by best estimate analysis. The results are similar enough so that the COL model could be used to determine the effect of blocking the open lane at one or more support plates.

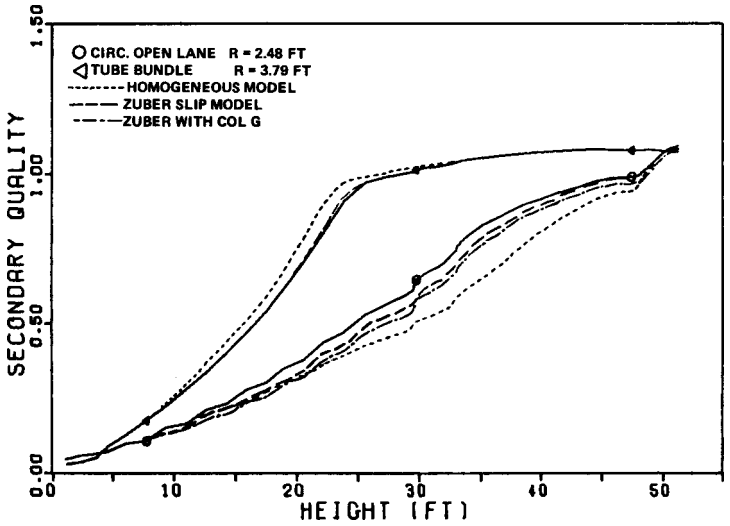

FIGURE 6 EFFECT OF CHANGES IN VOID FRACTION ON QUALITY PROFILES

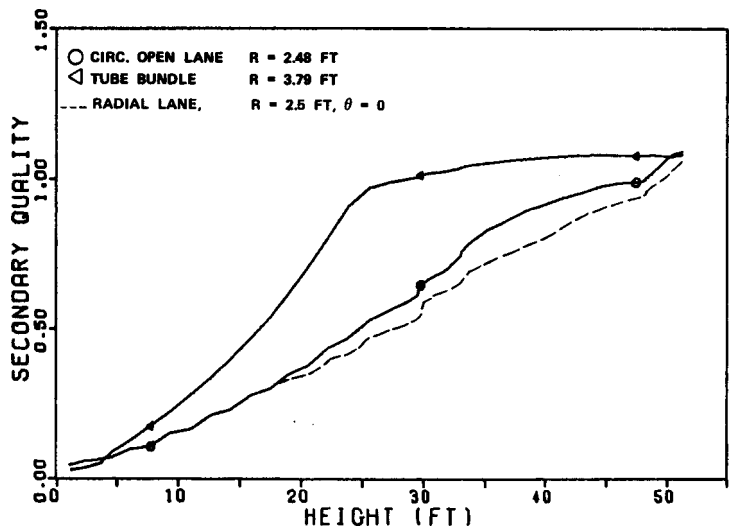

FIGURE 7 COMPARISON OF COL AND TMI-2 RADIAL OPEN LANE QUALITY PROFILES

For the majority of the sensitivity study runs as well as the best estimate analyses, the tube support plates were represented by the "regular" support plate (RSP) model. The RSP model is used when the axial spacing of control volumes is much larger than the thickness of a tube support plate. The axial flow resistance of the support plates is distributed over the entire height of the control volume. The radial and circumferential flow resistance of the tube support plate is not modeled.

Several sensitivity study runs were made with a fine grid support plate (FPSP) model using an axial grid spacing at the support plates which is on the same order as the tube support plate thickness. The radial and circumferential flow resistances are set to very large values in this model. However, the results of the FGSP runs were inconsistent so that it was not possible to determine if the FGSP model affects predicted local steam conditions as compared to the RSP model.

CONCLUSIONS

THEDA-1 predictions of both overall and local steam conditions are physically realistic and internally consistent. The OTSG functions primarily as a one-dimensional axial flow heat exchanger. Except near untubed regions and at the inlet and outlet, gradients in the radial and circumferential directions are much smaller than axial gradients.

The enthalpy in untubed regions is less than the bundle enthalpy at the same elevation. This enthalpy difference is less for DB-2 than for TMI-2 because the DB-2 tube support plates totally block the flow in untubed regions while the TMI-2 support plates do not.

Heat transfer and pressure drop correlation uncertainties and the number of control volumes used to model the OTSG have a relatively small effect on predicted outlet steam temperature and other overall performance parameters. Local thermal/hydraulic conditions, however, are more significantly affected. For the TMI-2 geometry, steam quality in untubed regions is affected by uncertainties in tube bundle axial pressure drop and the two-phase flow density.

The steam quality in untubed regions could not be accurately predicted using a model that distributes the tube support plate axial flow resistance uniformly over the length of the steam generator. A discrete control volume must be used at each

support plate. The effect of neglecting the radial and circumferential flow resistance of the tube support plates could not be conclusively demonstrated.

RECOMMENDATIONS

Although THEDA-1 provides reasonable predictions of the trends in local and overall thermal/hydraulic conditions, variations in modeling detail and correlation uncertainties, especially for two-phase flow, can affect accuracy. THEDA-1 predictions should be verified by comparison with experimental data.

Until such a comparison is available, the results of this study can be used to establish requirements for modeling detail and to evaluate the effect of correlation uncertainties.

Additional work in the following areas would improve the accuracy and efficiency of OTSG thermal/hydraulic analysis:

- Code Development
- Refined Two-Phase Flow Model (supported by experimental data)
- Refined Tube Support Plate Models
- Sensitivity Studies

Section 1

INTRODUCTION

The proprietary computer code THEDA-1 has been developed by Babcock & Wilcox (B&W) to calculate the thermal/hydraulic conditions for the B&W once-through steam generator (OTSG). This code performs a numerical analysis of the three-dimensional, steady-state thermal/hydraulics of the OTSG (1).

Specifically, the secondary side flow in and around the tubes and through the support plates is modeled using a "distributed resistance" concept. The steam generator geometry is described in a cylindrical coordinate system and two-phase flow is modeled with an algebraic slip flow model. This allows the liquid and vapor phases to be represented by one set of conservation equations: continuity, x, r, and θ momentum; and two energy equations: one for the secondary side fluid and the other for the primary side fluid.

The conservation equations contain many empirical parameters which are known to only a limited accuracy, such as void fraction, cross-flow resistance, and turbulent mixing. In many cases, these correlations were developed for one-dimensional flow and are being used in a multi-dimensional calculation. Therefore, a specific objective of this report is to determine the sensitivity of overall and local conditions to changes in empirical correlations. In particular, the correlations that yield the largest changes in local and overall conditions are identified.

Another aspect of the model that can limit the accuracy of the solution is the coarseness of the finite-difference grid. THEDA-1 does not use secondary storage and the total number of grid points is limited to about 9700 by the in-core storage of the B&W CDC 7600 computer. The computational expense of performing the calculations in full three-dimensional detail is also a consideration. Another objective of the study is, therefore, to determine if 9700 nodes are adequate to model the OTSG. This is accomplished by evaluating the sensitivity of local conditions to changes in the grid system.

In addition to the sensitivity study, best estimates of steam conditions are presented for two 177 Fuel Assembly (FA) Nuclear Steam Supply System OTSGs. The first is the Three Mile Island Unit 2 (TMI-2) steam generator. It contains geometrical features such as an open lane and an open peripheral gap that are typical of all but the most recent 177 Series OTSGs. The second is the steam generator for Davis-Besse Unit 2 (DB-2) which incorporates design features that differ from the TMI-2 units. Specifically, the open lane has been eliminated and the peripheral gap openings have been blocked. Although DB-2 is a 177 Series OTSG, these features are common to the OTSGs for B&W's 205 FA Nuclear Steam Supply Systems. Overall and local conditions for each steam generator are presented at 15%, 67%, and 100% plant load.

A description of the two steam generators, a discussion of the THEDA computer model, and the results from the best estimate analysis and sensitivity study are presented in this report.

Section 2

DESCRIPTION OF THE ONCE-THROUGH STEAM GENERATOR

The B&W 177 Series Once-Through Steam Generators (OTSGs) are used in both the Three Mile Island Unit 2 (TMI-2) and Davis-Besse Unit 2 (DB-2) Nuclear Steam Supply Systems. The overall geometry of the TMI-2 OTSG is very similar to the more recent DB-2 OTSG as well as other operating OTSGs in the 177 Series. Each unit does, however, contain different internal features that result in different local thermal/hydraulic conditions. These features are described in Sections 2.1 and 2.2. The operating conditions are listed in Section 2.3. Although all B&W 177 Series OTSGs are similar, there are minor differences in geometry and operating conditions. Therefore, the results presented in this report should be used with caution for 177 Series OTSGs other than TMI-2 and DB-2.

The 177 Series OTSG is a tube and shell, counterflow heat exchanger with straight vertical tubes. Primary reactor coolant flows downward through approximately 15,600 tubes and transfers heat to the secondary coolant flowing upward on the shell side. As shown in Figure 2.1, the primary side coolant boundary includes the hemispherical inlet and outlet heads, tubesheets, and inner tube surfaces. The secondary coolant is bounded by the shell, tubesheets, and outer tube surfaces.

Within the shell, the secondary coolant is divided into three regions by the upper and lower cylindrical shrouds. The space between the lower shroud and shell is the annular feedwater heating chamber. A second annulus is formed by the space between the upper shroud and shell to form the steam outlet annulus. The upper and lower shrouds also surround the tubes to form the main tube bundle.

Direct contact feedwater heating takes place in the annular feedwater heating chamber. Feedwater enters the chamber through the feedwater nozzles which provide a downward spray of water. Steam is drawn off by aspiration from the

main tube bundle through a gap between the upper and lower cylindrical shrouds. After mixing, the feedwater reaches the saturated liquid state. It then proceeds to the main tube bundle by passing through inlet ports at the bottom of the lower shroud.

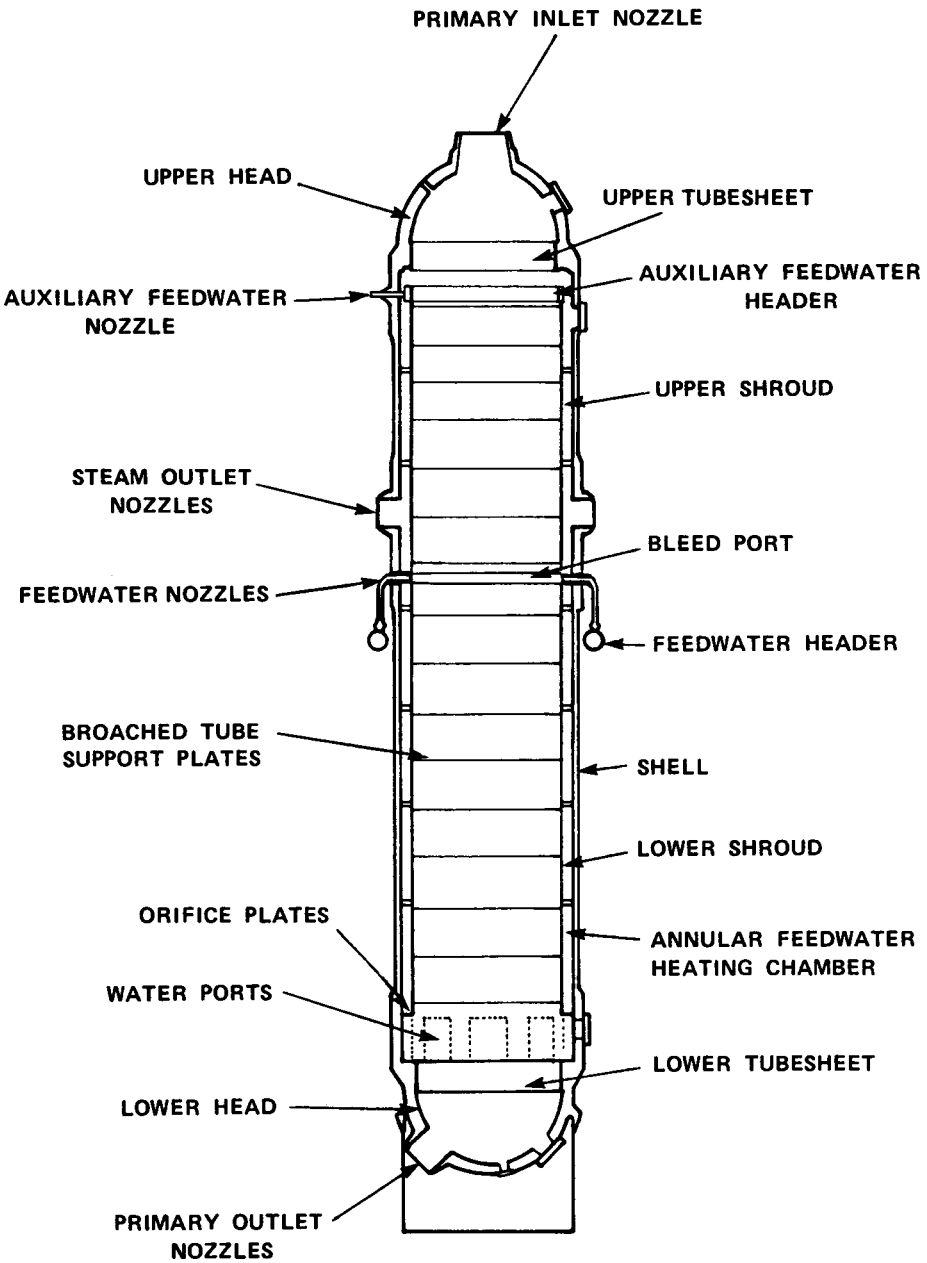

FIGURE 2.1A 177 SERIES ONCE-THROUGH STEAM GENERATOR

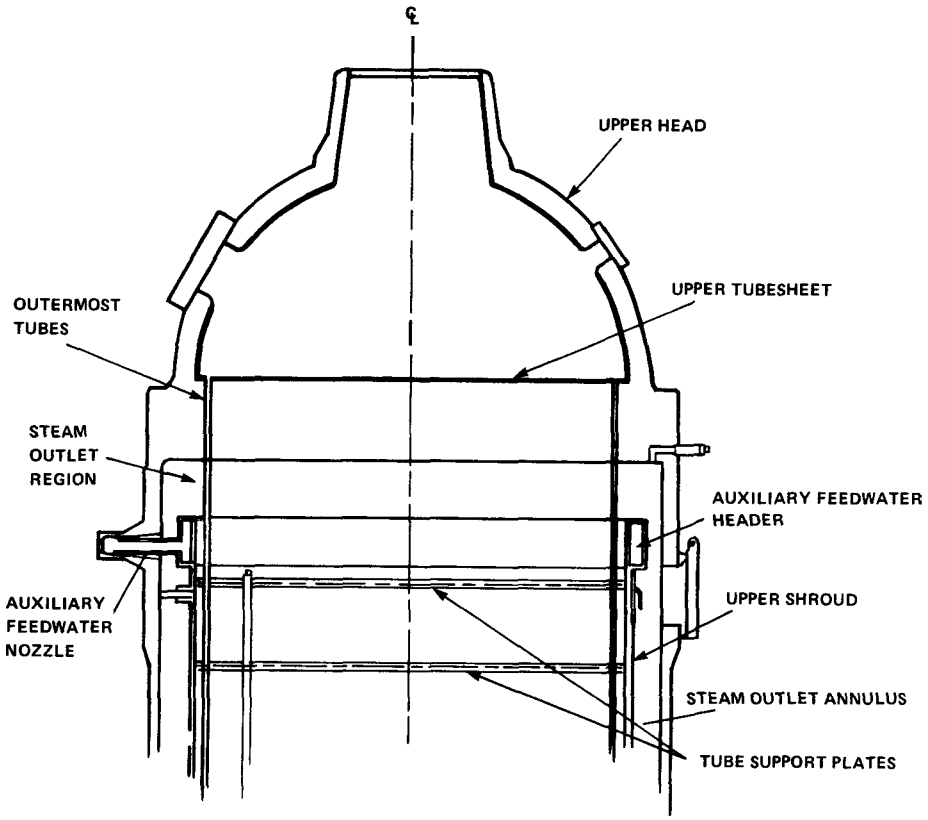

FIGURE 2.1B STEAM OUTLET REGION

In the tube bundle, broached tube support plates are fastened to the shroud and keep the tubes straight and at a uniform pitch. As secondary coolant travels upward, it passes through three heat transfer regimes. Starting at the lower tubesheet, they are:

1) Nucleate Boiling - In this region, the secondary side heat transfer coefficient is at its maximum. The vapor content of the two-phase mixture increases almost uniformly until film dryout occurs at about 95% quality. The boiling length is directly proportional to load.

2) Film Boiling - After film dryout, the heat transfer coefficient reduces to form the film boiling region. Here, saturated steam is produced.

3) Superheated Steam - Saturated steam is raised to its final exit temperature in the superheater region. The amount of tube surface area available for superheat varies inversely with load. As load decreases, the superheat section gains surface area from the nucleate and film boiling regions.

At the top of the tube bundle just below the upper tubesheet, superheated steam flows radially outward into the steam outlet annulus. From there, it flows downward and exits through the steam outlet nozzles.

2.1 THREE MILE ISLAND UNIT 2 INTERNAL FEATURES

There are several features inside the main tube bundle of the TMI-2 OTSG that are modeled. These features dictate the locations of the node points as described in Section 5.3.

The TMI-2 steam generators have an open lane to facilitate tube bundle inspection. The open lane consists of a row of 63 missing tubes that extend from the center of the tube bundle out to the periphery as shown in Figure 2.2. There are a total of 15 tube support plates in the TMI-2 steam generators which have the triangular pitch and broaching pattern used on all B&W OTSGs. Figure 2.3 shows that in the open lane the tube support plates are open to secondary flow since the missing tube locations are both drilled and broached.

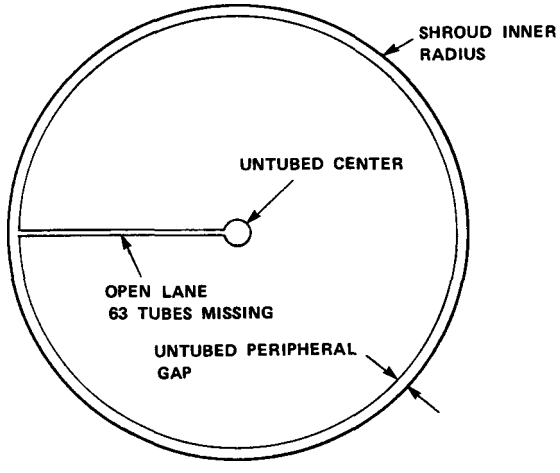

FIGURE 2.2 TMI-2 TUBE BUNDLE CROSS-SECTION

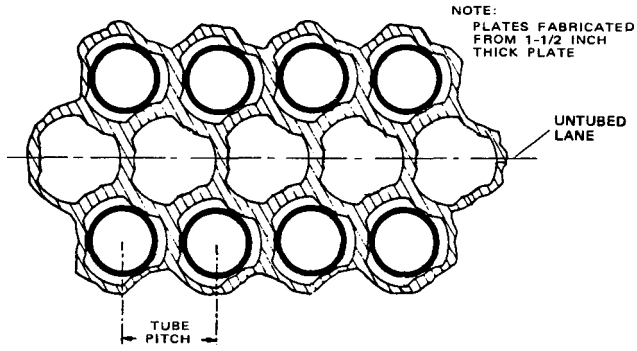

FIGURE 2.3 OPEN LANE WITH BROACHED TUBE SUPPORT PLATE (ENLARGED VIEW)

Other untubed regions include the untubed peripheral gap and the center untubed region as shown in Figure 2.2. The center region is untubed out to a radius of about three inches. The region is mostly blocked to flow at the support plates since the missing tube locations are neither drilled nor broached. There are, however, five bolt holes that remain from the manufacturing process which allow some flow to pass through. The total area of holes is small compared to the blocked area of the center untubed region.

The untubed peripheral gap is the space between the outermost boundary of tubes and the inner surface of the shroud. The gap is partially open to flow at the tube support plates 2 through 14 on TMI-2. As shown in Figure 2.4, the opening is the space between the outer edge of the tube support plate and the inner surface of the shroud. The open area is somewhat reduced by eight wedges that are used to align the tube support plates within the shroud. On tube support plates 1 and 15, the opening is almost totally blocked with 30 wedges instead of 8. A further blockage to flow near the peripheral gap is also provided with an outer rim of unbroached tube holes on the top (15th) tube support plate as shown in Figure 2.4.

In summary, the following features are found on the TMI-2 OTSG:

1) an open lane,
2) 15 tube support plates,
3) peripheral gap that is partially open at tube support plates 2-14 and is blocked at 1 and 15,
4) unbroached outer rim of tubes on tube support plate 15, and
5) center untubed region.

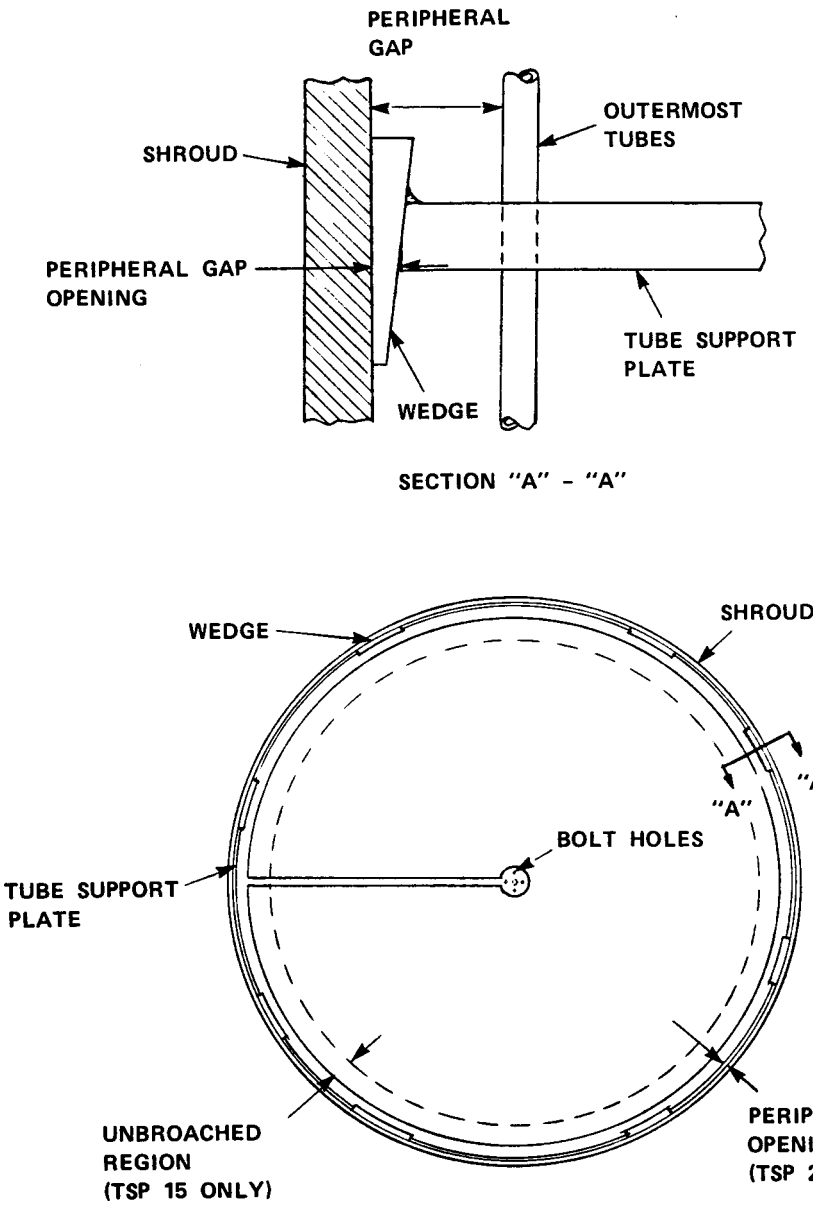

FIGURE 2.4 TMI-2 PERIPHERAL GAP GEOMETRY AND TOP TUBE SUPPORT PLATE UNBROACHED REGION

2.2 DAVIS-BESSE UNIT 2 INTERNAL FEATURES

The overall geometry of the DB-2 steam generators is very similar to that of the TMI-2 units. The tube bundle height, shroud inner radius, steam outlet opening, and feedwater inlet geometries are identical. The main differences are in the tube bundle open regions and tube support plates.

DB-2 does not have the TMI-2 open inspection lane. It does, however, have a circular lane of missing tubes that are at the boundary of the manway cover plate shown in Figure 2.5. The manway cover plates when removed from each of the tube support plates allow access to the steam generator internals during construction. The plates are drilled and broached so that they can be tubed along with the rest of the tube support plate upon re-insertion. On the boundary, the cover plate is either not drilled or is drilled but not broached as shown in Figure 2.5. The undrilled locations form a circular lane that is blocked to flow at each tube support plate.

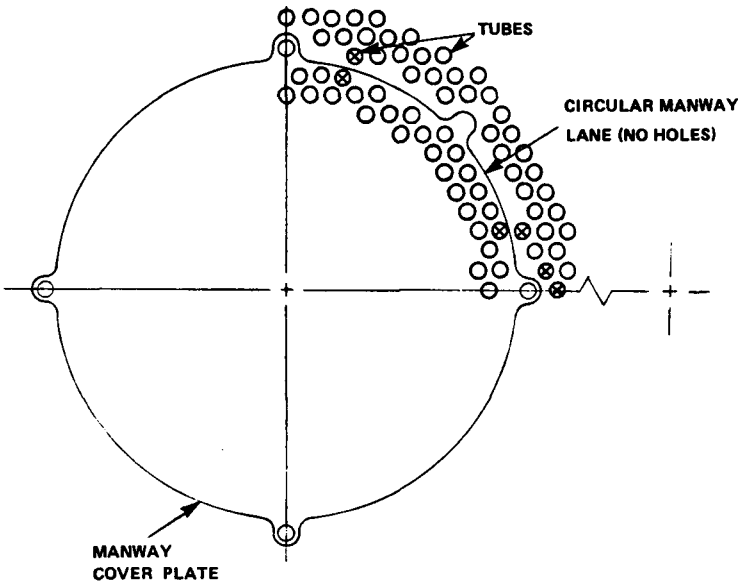

FIGURE 2.5 DB-2 MANWAY LANE

There are a total of 16 tube support plates in the DB-2 OTSG. At each support plate, the peripheral gap opening has been blocked with split rings as shown in Figure 2.6. The split ring segments are positioned at the peripheral gap openings between the eight wedges shown in Figure 2.6. They are welded into place on the top of the tube support plate.

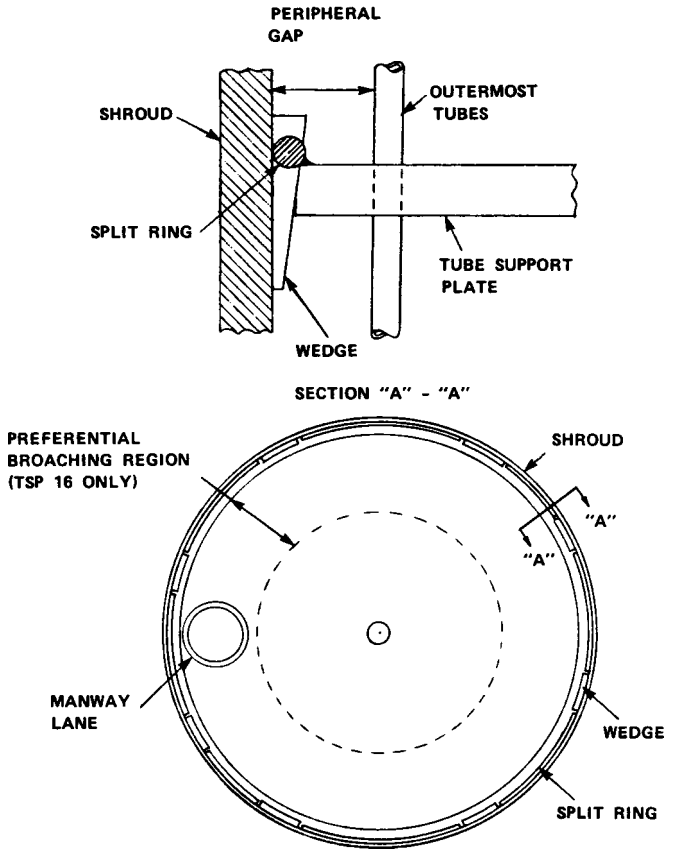

FIGURE 2.6 DB-2 PERIPHERAL GAP, MANWAY LANE, AND PREFERENTIAL BROACHING

On the top (16th) tube support plate, a preferential broaching pattern is used. The broaching area around each tube is smaller in the outer region shown in Figure 2.6. This reduces the tendency for the flow to bypass the center of the steam generator. The flow area per tube is approximately one-half the flow area per tube in the center. The larger broaching area in the center is the same as the broaching areas on all the remaining tube support plates.

The DB-2 steam generators also have a center untubed region that is identical to that on the TMI-2 units as discussed in Section 2.1. In addition, the DB-2 OTSG has a five-inch high steam bleed port (location shown in Figure 2.1) rather than the four-inch bleed port used on the TMI-2 OTSG.

In summary, the following features are found on the DB-2 OTSG:

1) circular lane,
2) 16 tube support plates,
3) a peripheral gap that is blocked at all tube support plates,
4) preferentially broached top tube support plate,
5) center untubed region, and
6) 5-inch bleed port rather than 4 inches on TMI-2.

2.3 DESIGN DATA AND OPERATING CONDITIONS

Steam generator design data and operating conditions obtained from the TMI-2 and DB-2 reactor coolant system functional specifications are given in Tables 2.1 and 2.2. The primary and secondary side thermal/hydraulic data are required as input to the THEDA Code at the three load levels analyzed. The 100% load case was selected for analysis because the highest secondary side cross-flow velocities and the lowest superheat occur at this load. Predicted overall performance is also most severely affected by uncertainies in empirical correlations at this load. The 67% load case roughly corresponds to the power level at which the maximum oscillations in steam generator flow, pressure, and temperature have been observed for operating units. The 15% load is the minimum load at which the reactor coolant average temperature is maintained constant by the automatic control system. This load is of interest because the short boiling length and high local heat fluxes produce rather large deviations from one-dimensional flow.

The design data includes overall dimensions and tube bundle specifications that are necessary as inputs to the analysis.

TABLE 2.1
OPERATING CONDITIONS

	THREE MILE ISLAND UNIT 2			DAVIS-BESSE UNIT 2		
	% of 2787 MWT			% of 2788 MWT		
	15%	67%	100%	15%	67%	100%
Primary Side						
Inlet temperature, °F	586	599	607.5	586	600	608.6
Inlet pressure, psia	2200	2200	2200	2200	2200	2200
Flow rate, 10^6 lbm/hr	68.95	68.95	68.95	65.65	65.65	65.65
Secondary Side						
Feedwater temperature, °F	282	420	466	282	425	465
Steam pressure, psia	900.5	909.3	924.9	885.7	902.5	925
Steam flow rate, 10^6 lbm/hr	0.80	3.75	5.916	0.865	3.76	5.95

TABLE 2.2
DESIGN DATA*

Distance between tubesheets, ft	52.115
Shroud inner radius, ft	4.932
Average bundle radius, ft	4.756
Water port height, ft	3.063
Steam outlet opening height, ft	1.094
Bleed port elevation**, ft	31.985
Bleed port openings, inches	4.0 - (TMI-2) 5.0 - (DB-2)
Tube outer diameter, inches	0.625
Tube metal thickness, inches	0.038
Tube pitch, inches	0.875
Tube support plate flow area per tube, sq. inch	0.156
Preferential broaching TSP flow area per tube, sq. inch	0.084
Radial lane width, inches	0.891

NOTES:

* Refer to Appendix A for the locations of the main grid points used to model the TMI-2 and DB-2 OTSGs.

** Distance from the bottom tubesheet to the top edge of the lower shroud.

Section 3

THEDA STEAM GENERATOR MODEL

The THEDA computer code (Three-Dimensional Steam Generator Thermal/Hydraulics Analysis) was originally developed by Dr. S. V. Patankar of the University of Minnesota for Babcock & Wilcox(1, 2, 3). The analysis is based on modeling the flow in and around the tubes, shrouds, support plates, etc., using a distributed resistance concept as opposed to modeling the subchannel flow in detail. The present version of THEDA uses an approximate algebraic slip flow model described in Section 3.2. It contains a set of conservation equations that are similar to those for a purely homogeneous flow with no slip between the phases. This approach allows the modeling of a steam generator in three-dimensions in an economically feasible manner.

3.1 CONSERVATION EQUATIONS

As mentioned previously, the flow in the secondary region, i.e. within the tube bundle, is treated as flow through a distributed resistance, similar to flow in a porous medium. The conservation equations are modified by the porosity, β (the ratio of the volume occupied by the fluid to the total nominal volume). In general, β varies with position. When there are no tubes or other solid obstructions in a particular flow region, β reduces to unity. Porosity enables the use of velocities based on the actual flow areas so that velocities do not have to be modified in the conservation equations to account for flow area changes.

The resistance of the tubes to flow is obtained from empirical correlations for the tube bundle configurations. Tube support plates are included as additional resistances. (Section 3.3).

A cylindrical coordinate system is employed to describe the system. The velocity components in this system are denoted by U, V, W in the x, r, and θ directions, respectively. The flow is described by the continuity equation,

the axial, radial, and tangential momentum equations, and the two energy equations for the secondary and primary side fluids. The secondary side equations for the steady-state flow are:

The Continuity Equation

$$\frac{\partial}{\partial x}(\beta\rho U) + \frac{1}{r}\frac{\partial}{\partial r}(\beta\rho rV) + \frac{1}{r}\frac{\partial}{\partial \theta}(\beta\rho W) = 0 \tag{3.1}$$

The Axial Momentum Equation

$$\frac{1}{\beta}\left[\frac{\partial}{\partial x}(\beta\rho U^2) + \frac{1}{r}\frac{\partial}{\partial r}(\beta\rho rVU) + \frac{1}{r}\frac{\partial}{\partial \theta}(\beta\rho WU)\right]$$

$$= -\frac{\partial P}{\partial x} - \rho_\alpha g + R_x$$

$$+ \frac{1}{\beta}\left[\frac{\partial}{\partial x}(\beta\mu_t\frac{\partial U}{\partial x}) + \frac{1}{r}\frac{\partial}{\partial r}(\beta r\mu_t\frac{\partial U}{\partial r}) + \frac{1}{r}\frac{\partial}{\partial \theta}(\beta\frac{\mu_t}{r}\frac{\partial U}{\partial \theta})\right] \tag{3.2}$$

The Radial Momentum Equation

$$\frac{1}{\beta}\left[\frac{\partial}{\partial x}(\beta\rho UV) + \frac{1}{r}\frac{\partial}{\partial r}(\beta\rho rV^2) + \frac{1}{r}\frac{\partial}{\partial \theta}(\beta\rho WV)\right]$$

$$= -\frac{\partial P}{\partial r} + \rho\frac{W^2}{r} + R_r$$

$$+ \frac{1}{\beta}\left[\frac{\partial}{\partial x}(\beta\mu_t\frac{\partial V}{\partial x}) + \frac{1}{r}\frac{\partial}{\partial r}(\beta r\mu_t\frac{\partial V}{\partial r}) + \frac{1}{r}\frac{\partial}{\partial \theta}(\beta\frac{\mu_t}{r}\frac{\partial V}{\partial \theta})\right] \tag{3.3}$$

The Tangential Momentum Equation

$$\frac{1}{\beta}\left[\frac{\partial}{\partial x}(\beta\rho UW) + \frac{1}{r}\frac{\partial}{\partial r}(\beta\rho rVW) + \frac{1}{r}\frac{\partial}{\partial \theta}(\beta\rho W^2)\right]$$

$$= -\frac{1}{r}\frac{\partial P}{\partial \theta} - \rho\frac{VW}{r} + R_\theta$$

$$+ \frac{1}{\beta}\left[\frac{\partial}{\partial x}(\beta\mu_t\frac{\partial W}{\partial x}) + \frac{1}{r}\frac{\partial}{\partial r}(\beta r\mu_t\frac{\partial W}{\partial r}) + \frac{1}{r}\frac{\partial}{\partial \theta}(\beta\frac{\mu_t}{r}\frac{\partial W}{\partial \theta})\right] \tag{3.4}$$

Secondary Side Energy Equation

$$\frac{1}{\beta}\left[\frac{\partial}{\partial x}(\beta\rho Uh) + \frac{1}{r}\frac{\partial}{\partial r}(\beta\rho rVh) + \frac{1}{r}\frac{\partial}{\partial \theta}(\beta\rho Wh)\right] = S_h$$

$$+ \frac{1}{\beta}\left[\frac{1}{r}\frac{\partial}{\partial r}(\beta r\Gamma_t\frac{\partial h}{\partial r}) + \frac{1}{r}\frac{\partial}{\partial \theta}(\frac{\beta\Gamma_t}{r}\frac{\partial h}{\partial \theta})\right] \tag{3.5}$$

where

ρ = density
ρ_α = volume weighted density
P = pressure
h = enthalpy
β = porosity
μ_t = turbulent viscosity
Γ_t = μ_t/Pr_t
Pr_t = turbulent Prandlt number

Several features of this system of equations should be noted. The momentum equations are written in the conservative form. Since the x-direction is assumed to be vertically upward, the gravitational acceleration g, appears in the axial momentum equation only. All terms appearing on the left-hand side of the equations are the convective transport terms. The definitions of density ρ, used in the convective transport terms, and volume weighted density ρ_α, used in the buoyancy term, are discussed in Section 3.2 in connection with the slip flow model. The terms R_x, R_r, and R_θ are the distributed resistances. These terms represent the forces exerted by the flow obstructions, i.e., tubes, baffles, or tube support plates, per unit volume occupied by the fluid.

The second group of terms on the right-hand side of the radial and tangential momentum equations is the centrifugal and Coriolis forces per unit volume, respectively. Each term arises automatically on the transformation from rectangular to cylindrical coordinates. The centrifugal force is the effective force in the radial direction resulting from fluid motion in the tangential direction. The Coriolis force is the effective force in the tangential direction when there is flow in both the radial and tangential directions.

S_h in the energy equation represents the heat transfer to the fluid per unit volume. Also, in the energy equation axial diffusion, kinetic energy, potential energy, and dissipation have been neglected since the transport of these quantities is small compared to the convective transport of enthalpy.

All quantities appearing in these equations are assumed to be time averaged representations of the turbulent flow. Turbulent mixing is modeled by using an effective or eddy viscosity concept. It is assumed that a turbulent mixing

process, analogous to laminar diffusion, can be used in both the single-phase and two-phase regions. Thus, the turbulent transport terms on the right-hand side of the momentum equations are in the same form as laminar diffusion terms except that the laminar viscosity has been replaced by an effective turbulent viscosity, μ_t. The turbulent viscosity is calculated from a mixing length correlation. Similarly, thermal diffusivity has been introduced into the energy equation through Γ_t which is related to the effective turbulent viscosity via the turbulent Prandtl number, Pr_t.

On the primary side, the energy equation for the tube fluid is

$$- G_t \frac{\partial h_t}{\partial x} = \frac{4q_t}{d_t} \tag{3.6}$$

where

h_t = tube fluid enthalpy

G_t = tube fluid mass velocity

q_t = heat flux at the tube inner surface

d_t = tube inner diameter

The continuity equation for the tube flow is simply that G_t is constant. Since the tube flow pressure drop is small compared to the total primary side pressure, it is assumed that the pressure of the single-phase fluid is constant along the length of the tube. With this assumption, the solution of the momentum equation is not required. In the energy equation, it is assumed that G_t is known for a given tube or cluster of tubes that are enclosed by a control volume. q_t is obtained with an overall heat transfer coefficient, U_t, based on the tube inner area by the expression

$$q_t = U_t (T_p - T_s) \tag{3.7}$$

where

$$U_t = \left(\frac{1}{h_p} + \frac{r_i \ln (r_o/r_i)}{k_m} + \frac{r_i}{r_o} \frac{1}{h_s} \right)^{-1} \tag{3.8}$$

h_p = primary side heat transfer coefficient

h_s = secondary side heat transfer coefficient

k_m = tube metal thermal conductivity

r_i = tube inner radius

r_o = tube outer radius

T_p = primary side temperature

T_s = secondary side temperature

The heat transfer coefficients, h_p and h_s, and tube metal thermal conductivity, k_m, are determined by empirical correlations discussed in Section 3.3.

Coupling of the secondary side thermal/hydraulic equations with the primary fluid equation given by Eq. 3.6 is accomplished by the source term S_h in the secondary energy equation. The heat flux q_s on the outer side tube surface is given by

$$q_s = \frac{r_i}{r_o} \quad q_t \tag{3.9}$$

S_h in Eq. 3.5 is then defined as

$$S_h = \frac{P_s}{A_s} \quad q_s \tag{3.10}$$

where

P_s = heated perimeter = $2\pi\ r_o$

A_s = secondary flow area per tube

3.2 RELATIONSHIP BETWEEN SLIP FLOW AND HOMOGENEOUS FLOW

As discussed in Section 3.1, the conservation equations in THEDA-1 are based on a homogeneous two-phase flow model. In this section, it will be shown that the equations for a homogeneous fluid (Eq. 3.1 through 3.4) also approximately represent the mixture conservation equation for separated flow subject to the following assumption:

- The vapor/liquid velocity ratio (slip) is the same in all three directions and can be defined by an algebraic slip correlation.

In the remainder of Section 3.2, it is shown how the homogeneous model used in THEDA-1 is approximately equivalent to an algebraic slip model based on this assumption. The convective term of the mixture conservation equations is written as a function of the individual liquid and vapor velocities, densities, and enthalpies. Each mixture conservation equation is then equated to the equivalent homogeneous fluid conservation equation as used in THEDA-1. Expressions are derived for the mixture density and enthalpy that satisfy each of the mixture conservation equations. The density and enthalpy so defined are compared to the density and enthalpy used in the conservation equations (Eq. 3.1 through 3.4) contained in THEDA-1. The differences between the homogeneous model and the approximate algebraic slip model are pointed out.

The development of the three-dimensional mixture conservation equation closely follows the method presented in Reference 4 (Page 177) for one-dimensional flow. To begin, the liquid and vapor velocities are defined as $\underline{U}_L$ and $\underline{U}_g$, respectively. The vector magnitudes $|\underline{U}_L|$ and $|\underline{U}_g|$ may be different. This difference is expressed by the velocity ratio defined as

$$S = \frac{|\underline{U}_g|}{|\underline{U}_L|} \tag{3.11}$$

In general, S is greater than unity for conditions encountered in the OTSG. If we assume that the velocity ratio is the same in all directions, the two-phase velocites can be represented as

$$\underline{U}_L = |\underline{U}_L| \ \hat{u} \tag{3.12}$$

$$\underline{U}_g = |\underline{U}_g| \ \hat{u} \tag{3.13}$$

where $\hat{u}$ is a direction vector of unit length. If $U_{i,g}$ and $U_{i,L}$ are the U, V, and W components of the vapor and liquid velocities, respectively, then the assumption of equal slip in all directions can be expressed as

$$S = \frac{U_{i,g}}{U_{i,L}} \tag{3.14}$$

Using Eq. 3.14, the conservation equations written in terms of individual phase velocites can be reduced to a form similar to that for single-phase flow.

Void fraction, α, is defined as the ratio of vapor volume to the total volume of two-phase fluid. This may also be envisioned as the ratio of vapor area, A_g, to total area A in a plane perpendicular to the velocity vectors as shown in Figure 3.1.

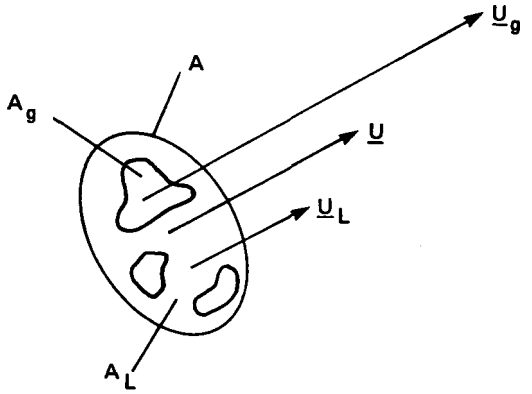

FIGURE 3.1 TWO-PHASE VELOCITIES

The void fraction can thus be defined as

$$\alpha = \frac{A_g}{A_g + A_L} = \frac{A_g}{A} \tag{3.15}$$

where

A_g = vapor area

A_L = liquid area

The average velocity $\underline{U}$ can be defined as the total volumetric flow rate of liquid and vapor passing through area A. If $\underline{Q}_L$ and $\underline{Q}_g$ are the volumetric flow rates, then

$$\underline{U} = \frac{\underline{Q}_g + \underline{Q}_L}{A} \tag{3.16}$$

From Figure 3.1, it is apparent that

$$\underline{Q}_g = A_g \underline{U}_g \tag{3.17}$$

$$\underline{Q}_L = A_L \underline{U}_L \tag{3.18}$$

Therefore, the average velocity may be written in terms of void fraction and phase velocities as

$$\underline{U} = \alpha \underline{U}_g + (1-\alpha) \underline{U}_L \tag{3.19}$$

As a result of the assumption of equal velocity ratio in all directions, the average velocity has the same direction vector $\hat{u}$ as the phase velocites.

The flow quality, χ, is the ratio of mass flow rate of vapor to the total mass flow rate passing through area A. It can be expressed as

$$\chi = \frac{\alpha \rho_g |\underline{U}_g|}{\alpha \rho_g |\underline{U}_g| + (1-\alpha) \rho_L |\underline{U}_L|} \tag{3.20}$$

where

ρ_g = vapor density

ρ_L = liquid density

This equation can be rearranged to give void fraction as a function of flow quality and slip ratio as

$$\alpha = \frac{\chi}{\chi + S \frac{\rho_g}{\rho_L} (1 - \chi)} \tag{3.21}$$

This equation is commonly referred to as the S-α-χ relation in the one-dimensional slip flow model. In general, void fraction is not known since the slip ratio in Eq. 3.21 can vary for different flow regimes. Empirical correlations are, therefore, necessary to evaluate α. These correlations, which are presented in Section 3.3, are usually given as a function of flow quality and other fluid properties for one-dimensional flows in tubes and annuli.

With void fraction given by a correlation, the volume weighted density ρ_α in Eq. 3.2 can then be calculated by the equation

$$\rho_\alpha = \alpha \rho_g + (1-\alpha) \rho_L \tag{3.22}$$

The density, ρ, used in the convective terms of the continuity, energy, and momentum equations remain to be defined. The derivation is accomplished by applying the constant velocity ratio assumption to the convective terms for each conservation equation written in terms of separate phase velocities.

For the continuity equation, the convective term is the divergence of the sum of the mass flow rates given by

$$\nabla\cdot(\beta\rho\underline{U}) = \nabla\cdot\left[\beta\left(\alpha\rho_g \underline{U}_g + (1 - \alpha) \rho_L \underline{U}_L\right)\right] \tag{3.23}$$

Since it has been assumed that $\underline{U}_g$ and $\underline{U}_L$, and therefore $\underline{U}$, have the same direction vector $\hat{u}$, it follows that ρ appearing in Eq. 3.23 is defined by

$$\rho = \frac{\alpha\rho_g U_{i,g} + (1 - \alpha) \rho_L U_{,i,L}}{\alpha U_{i,g} + (1 - \alpha) U_{i,L}} \tag{3.24}$$

Combining Eq. 3.14 and 3.21 with Eq. 3.24 yields

$$\rho = \frac{\rho_g \rho_L}{\chi \rho_L + (1 - \chi)\, \rho_g} \tag{3.25}$$

Thus, the convective term in the continuity equation can be expressed in terms of density ρ (Eq. 3.25) and average velocity $\underline{U}$ (Eq. 3.16) rather than the individual phase velocities and densities.

Note that in THEDA-1, the two phases are assumed to be in thermal equilibrium at saturation conditions and the steady-state mixture continuity equation for separated flow is satisfied by the same mixture density as the homogeneous continuity equation.

For the special case of homogeneous flow (velocity ratio equal to unity), it can be shown by applying Eq. 3.21 that ρ and ρ_α are identical. But, in general, ρ is less than ρ_α for a given quality and a slip ratio greater than one.

The mixture enthalpy in the energy equation can be obtained in the same manner as the mixture density was obtained in the continuity equation. The convective term in the energy equation can be expressed as the divergence of the energy flow rate of both phases as

$$\nabla \cdot (\beta \rho h \underline{U}) = \nabla \cdot \left[\beta \left(\alpha \rho_g h_g \underline{U}_g + (1 - \alpha)\, \rho_L h_L \underline{U}_L \right) \right] \tag{3.26}$$

Again by assuming a constant velocity ratio in all directions, it follows that

$$h = \frac{\alpha \rho_g h_g U_{i,g} + (1 - \alpha)\, \rho_L h_L U_{i,L}}{\alpha U_{i,g} + (1 - \alpha)\, U_{i,L}} \; \frac{1}{\rho} \tag{3.27}$$

Combining this with Eq. 3.14 and 3.21, and defining ρ so that continuity is satisfied (Eq. 3.25) yields

$$h = \chi\, h_g + (1 - \chi)\, h_L \tag{3.28}$$

Thus, flow quality given by Eq. 3.20 is readily calculated from the average enthalpy by

$$\chi = \frac{h - h_L}{h_g - h_L} \tag{3.29}$$

In THEDA-1, thermal equilibrium is assumed and the flow quality (Eq. 3.29) is identical to the thermodynamic quality, where h_L and h_g are evaluated at saturation conditions.

For the momentum equations, a momentum density, ρ_m, in the mixture equation can be defined so that the following expression is satisfied for the convective transport of momentum

$$\nabla\cdot(\beta\rho_m \underline{U}\underline{U}) = \nabla\cdot\left[\beta\left(\alpha\rho_g \underline{U}_g\underline{U}_g + (1-\alpha)\,\rho_L \underline{U}_L\underline{U}_L\right)\right] \tag{3.30}$$

In this equation, $\underline{U}\,\underline{U}$, $\underline{U}_g\,\underline{U}_g$, and $\underline{U}_L\,\underline{U}_L$ are tensors with elements U_iU_j, $U_{i,g}$ $U_{j,g}$ and $U_{i,L}$ $U_{j,L}$, respectively. Since THEDA-1 approximates the convective term by $\nabla\cdot(\beta\,\rho\,\underline{U}\,\underline{U})$ where $\underline{U}$ and ρ are given by Eq. 3.16 and 3.25, it is necessary to find the neglected amount of density $\delta\rho$ such that

$$\rho_m = \rho - \delta\rho \tag{3.31}$$

To solve for $\delta\rho$, Eq. 3.19 and 3.21 can be combined in two different ways to give

$$U_{i,g} = \frac{\chi}{\rho_g\,\alpha}\,\rho\,U_i \tag{3.32}$$

$$U_{i,L} = \frac{(1-\chi)}{\rho_L\,(1-\alpha)}\,\rho\,U_i \tag{3.33}$$

By applying Eq. 3.31, 3.32, and 3.33 to Eq. 3.30, the following expression can be obtained

$$\delta\rho = (\alpha - \chi)\left[\frac{\chi}{\rho_g \alpha} - \frac{(1-\chi)}{\rho_L (1-\alpha)}\right]\rho^2 \tag{3.34}$$

or written in terms of slip ratio

$$\delta\rho = (\alpha - \chi)\left(\frac{\chi}{\alpha}\right)\left(\frac{S - 1}{S}\right)\frac{\rho^2}{\rho_g} \tag{3.35}$$

Since, in general, the slip ratio is greater than unity, $\delta\rho$ is positive and ρ_m is less than ρ. For purely homogeneous flow, S = 1, $\delta\rho$ = 0, and $\rho_m = \rho$.

The approximation of ρ for ρ_m in the momentum equations in THEDA-1 implies that the quantities expressed by

$$\frac{1}{\beta}\ \nabla\cdot(\beta\ \delta\rho\ \underline{U}\ \underline{U}) \tag{3.36}$$

have been neglected on the right-hand side of Eq. 3.2, 3.3, and 3.4.

The error represented by Eq. 3.36 has a small effect on velocity when the flow is predominantly in the axial direction because $\nabla\cdot(\beta\delta\rho\ \underline{U}\ \underline{U})$ is small compared to other terms in the momentum equations. However, in untubed regions where cross-flow is important $\nabla\cdot(\beta\delta\rho\ \underline{U}\ \underline{U})$ could be significant. However, the assumption of equal velocity ratios in all directions is probably not valid in these regions and it may not be worthwhile to further refine the analysis.

Transformation to cylindrical coordinates also implies that the true centrifugal and Coriolis force terms, $\rho_m \frac{W^2}{r}$ and $\rho_m \frac{VW}{r}$, respectively, have been approximated by $\rho \frac{W^2}{r}$, and $\rho\frac{VW}{r}$ in the momentum equations. For the two-dimensional sensitivity studies, W is zero and the substitution of ρ and ρ_m causes no error in the centrifugal and Coriolis force terms. For the three-dimensional, best-estimate analysis, W is small so that the approximation of the Coriolis and centrifugal forces probably does not cause a significant error.

In summary, the THEDA-1 homogeneous two-phase flow mixture equations for conservation of mass and energy are equivalent to the mixture equations derived from a separated flow model, assuming that the velocity ratio between the phases is identical in all three directions. The THEDA-1 conservation of momentum equations are a reasonable approximation of the separated flow mixture equations.

3.3 EMPIRICAL CORRELATIONS

In addition to the governing equations, empirical correlations are required to complete the description of the fluid flow and heat transfer. The correlations come into the solution process through the source terms and diffusion terms in the conservation equations. Correlations are used to calculate distributed resistances for the momentum equations and heat transfer for the primary and secondary side energy equations. Void fraction correlations are used to calculate two-phase density for the gravitational pressure drop in the axial momentum equation. A correlation is also used to calculate the turbulent diffusion coefficients in the momentum and energy equations.

Void Fraction

Several empirical correlations for void fraction were examined to determine the sensitivity of local thermal/hydraulic conditions to changes in the two-phase volume weighted density. The study included the correlations of Smith (5), Thom (6), and Zuber (7), and the homogeneous void fraction model. The Smith correlation has been used previously to predict conditions in a laboratory 19-tube once-through steam generator.

The following assumptions were made by Smith:

1) The flow is separated (annular) with a homogeneous mixture phase and a liquid phase.
2) The homogeneous mixture phase and the liquid phase have the same velocity head, i.e., $\rho_L U_L^2 = \rho_{mix} U_{mix}^2$.
3) The homogeneous mixture behaves as a single-phase fluid with a variable density.
4) Thermal equilibrium exists.

With these assumptions, the void fraction can be defined as

$$\alpha = \frac{\frac{\rho_L}{\rho_g} \chi}{\chi_1 + (1-K_S)(1-\chi)\left[\frac{\chi_1}{\chi + K_S(1-\chi)}\right]^{1/2}} \qquad (3.37)$$

where

$$\chi_1 = \frac{\rho_L}{\rho_g} \chi + K_S (1-\chi)$$

$$K_S = \frac{\text{mass of water flowing in homogeneous mixture}}{\text{total mass of water flowing}} \qquad 0 \leq K_S \leq 1$$

Smith recommends $K_S = 0.4$ for correlating most data; however, Babcock & Wilcox (B&W) has found that using $K_S = 0.0$ resulted in best agreement between measured and predicted 19-tube OTSG pressure drop data. $K_S = 0$ implies that no liquid is entrained in the flowing vapor. Eq. 3.37 then becomes

$$\alpha = \frac{\chi}{\chi + (1-\chi)\left(\frac{\rho_g}{\rho_L}\right)^{1/2}} \tag{3.38}$$

This form of Smith's correlation was used as the nominal void fraction correlation in the sensitivity study to which all others were compared.

The homogeneous model is obtained by setting K_S equal to unity. The homogeneous void fraction thus becomes

$$\alpha_H = \frac{\chi}{\chi + (1-\chi)\left(\frac{\rho_g}{\rho_L}\right)} \tag{3.39}$$

The void fraction correlation of Thom (6) is given in terms of a parameter γ as

$$\alpha = \frac{\gamma\chi}{1 + (\gamma-1)\chi} \tag{3.40}$$

where

$$\gamma = \frac{\rho_L}{S\,\rho_g} \tag{3.41}$$

Thom found that for vertical flow in a tube, γ is a function of phase densities and saturation pressure. His tabular values for γ can be represented by the following curve fit

$$\gamma = \left(\frac{\rho_L}{\rho_g}\right)^{0.8294 - 1.1672/P_{sat}} \tag{3.42}$$

The correlation of Zuber (7) is based on the drift flux model. In this model, the relative velocity between the phases, U_{gL}, can be expressed as

$$U_{gL} = \frac{j_g}{\alpha} - \frac{j_L}{1-\alpha} \tag{3.43}$$

where

j_g = the volumetric flux of the vapor (Q_g/A)

j_L = the volumetric flux of the liquid (Q_L/A)

The drift flux can then be defined as

$$j_{gL} = U_{gL}\ \alpha(1-\alpha) = j_g\ (1-\alpha) - j_L\alpha \tag{3.44}$$

The total volumetric flux is defined as

$$j = j_g + j_L \tag{3.45}$$

The drift flux, j_{gL}, phsically represents the volumetric rate per unit area at which vapor is passing forward (in up-flow) or backwards (in down-flow) through a plane normal to the channel axis and traveling with the flow of a velocity j. To preserve continuity, an equal and opposite drift flux of liquid, j_{Lg}, must also pass across the same plane.

By combining Eq. 3.44 and 3.45 and averaging over the flow channel cross-sectional area (denoted by bars), it can be shown that

$$\bar{j}_g = (\overline{\alpha j}) + \bar{j}_{gL} \tag{3.46}$$

Zuber then defines a concentration parameter, C_o, and a weighted mean drift velocity, $\bar{U}_{gj}$, such that

$$C_o = \frac{(\overline{\alpha j})}{\bar{\alpha}\,\bar{j}} \tag{3.47}$$

$$\bar{U}_{gj} = \frac{\bar{j}_{gL}}{\bar{\alpha}} \tag{3.48}$$

The average void fraction is then obtained by combining Eq. 3.46, 3.47, and 3.48 so that

$$\bar{\alpha} = \frac{\bar{j}_g}{C_o\,\bar{j} + \bar{U}_{gj}} \tag{3.49}$$

By noting that $\bar{j}_g$ and $\bar{j}_L$ are equal to αU_g and $(1-\alpha)\,U_L$ in Eq. 3.32 and 3.33, it can be shown that (with bars dropped for consistency with the previous notation)

$$\alpha = \frac{x}{C_o\left[x + \frac{\rho_g}{\rho_L}(1-x)\right] + \frac{\rho_g \bar{U}_{gj}}{G}} \tag{3.50}$$

where

G = mass velocity

The values of concentration parameter and drift velocity were found by Zuber to be a function of flow regime. B&W has obtained good agreement between predicted and measured boiler liquid inventories in the 19-tube steam generator during loss of feedwater flow tests by using the following expressions

$$C_o = 1.13 \qquad \alpha<\alpha_c$$

$$C_o = 1.13 - \frac{(\alpha - \alpha_c)\ (1.13 - 1.0)}{(1.0 - \alpha_c)} \qquad \alpha_c \leq \alpha \leq 1 \qquad (3.51)$$

and

$$\bar{U}_{gj} = U_{tr} \qquad \alpha<\alpha_c$$

$$\bar{U}_{gj} = U_{tr} - \frac{\alpha - \alpha_c}{1.0 - \alpha_c}\ U_{tr} \qquad \alpha_c \leq \alpha \leq 1 \qquad (3.52)$$

where α is calculated from Eq. 3.50 and

$$U_{tr} = 1.41 \left[\frac{\sigma g g_c\ (\rho_L - \rho_g)}{\rho_L} \right]^{1/4}$$

α_c = 0.8

σ = surface tension

g = gravitational acceleration

g_c = gravitational constant

This void fraction interpolation scheme (Eq. 3.51 and 3.52) was used for the high void fractions encountered in the OTSG so that $C_o \rightarrow 1$ and $\bar{U}_{gj} \rightarrow 0$ as $\alpha \rightarrow 1$. If these conditions are not satisfied, α would not equal 1 at χ equal 1.

C_o and $\bar{U}_{gj}$ are void fraction dependent with this scheme, and to avoid a somewhat complex iteration scheme, the homogeneous void fraction was used in place of Eq. 3.51 as follows

$$C_o = 1.13 \qquad \alpha_H < \alpha_{CH}$$

$$C_o = 1.13 - \frac{(\alpha_H - \alpha_{CH})(1.13 - 1.0)}{(1.0 - \alpha_{CH})} \qquad \alpha_{CH} \leq \alpha_H \leq 1 \qquad (3.53)$$

and

$$\left.\begin{aligned} \overline{U}_{gj} &= U_{tr} && \alpha_H < \alpha_{CH} \\ \overline{U}_{gj} &= U_{tr} - \frac{\alpha_H - \alpha_{CH}}{1.0 - \alpha_{CH}} U_{tr} && \alpha_{CH} \leq \alpha_H \leq 1 \end{aligned}\right\} \quad (3.54)$$

where

α_H = homogeneous void fraction, Eq. 3.39

α_{CH} = 0.93

Eq. 3.50 was used to determine the quality at which $\alpha = \alpha_c$ at 100% load. α_{CH} was calculated at the same quality. Below this quality where the two-phase density is most strongly dependent on void fraction, both interpolation schemes give identical void fractions. Above this quality the difference between the two schemes is insignificant.

A second approximation made in applying Zuber's correlation was that G in Eq. 3.50 is equal to the average mass velocity in the steam generator rather than the locally computed axial mass velocity, ρU. The average mass velocity is

$$G = \frac{\dot{m}_B + \dot{m}_{SG}}{A_{SG}} \qquad X < X_{BP} \qquad (3.55)$$

$$G = \frac{\dot{m}_{SG}}{A_{SG}} \qquad X \geq X_{BP} \qquad (3.56)$$

where

$\dot{m}_{SG}$ = steam flow rate

$\dot{m}_B$ = bleed flow rate

A_{SG} = steam generator cross-sectional area

X_{BP} = bleed port elevation

This definition of G was used as a simple way to prevent unrealistic values of void fraction from being computed near tube support plate obstructions where G is very small or even negative.

Turbulent Exchange

The turbulent exchange between adjacent control volumes is modeled as a diffusion process. The turbulent diffusion coefficient used in this analysis is

$$\Gamma_t = C_i \rho \bar{U} s \tag{3.57}$$

where

C_i = mixing coefficient

$\bar{U}$ = average velocity between subchannels

s = characteristic subchannel dimension or dimension of gap between tubes

This model is commonly used in reactor core thermal/hydraulic analysis (8). B&W rod bundle data indicates that C_i is on the order of 0.01 for single-phase flow. We have taken this value of C_i as an order of magnitude estimate for the OTSG tube bundle and used it as a nominal value. It is considered to be only a crude estimate with high uncertainty.

The effective turbulent viscosity is obtained with the turbulent Prandtl taken as unity so that

$$\mu_t = Pr_t \Gamma_t = \Gamma_t = (0.01) \rho |\underline{U}| t_p / \sqrt{3} \tag{3.58}$$

where

$$|\underline{U}| = \sqrt{U^2 + W^2 + V^2} \tag{3.59}$$

t_p = tube pitch

Axial Resistance

The axial resistance, R_x, includes friction losses in the tube bundle and tube support plate form losses. If a control volume contains a tube support plate, then the total resistance is given by

$$R_x = R_{fr} + R_{tsp} \tag{3.60}$$

where

R_{fr} = axial tube friction resistance

R_{tsp} = tube support plate resistance

When a control volume is without a tube support plate, the resistance is given by R_{fr} only.

The frictional resistance is calculated by

$$R_{fr} = - 2 f_x \frac{\rho U | \underline{U} |}{D_h} \phi_{fo}^2 \tag{3.61}$$

where

D_h = hydraulic diameter = $\frac{4 A_s}{P_s}$

ϕ_{fo}^2 = two-phase friction multiplier

The Blassius friction factor, f_x, (9) is given by

$$f_x = \frac{16}{Re} \qquad Re < 2000 \tag{3.62}$$

and

$$\frac{1}{\sqrt{f_x}} = 4 \log_{10} \left(Re \sqrt{f_x} \right) - 0.4 \qquad Re \geq 2000 \tag{3.63}$$

where

$$Re = \frac{\rho | \underline{U} | D_h}{\mu}$$

When film dryout occurs, a vapor film surrounds the tube; therefore, the vapor viscosity is used in the Reynolds number. If the film dryout quality is χ_{DO}, then

$$\left.\begin{aligned} \mu &= \mu_g \quad \text{for} \quad \chi > \chi_{DO} \\ \mu &= \mu_L \quad \text{for} \quad \chi \leq \chi_{DO} \end{aligned}\right\} \tag{3.64}$$

where

μ_g = vapor viscosity

μ_L = liquid viscosity

The Thom two-phase friction multiplier ϕ^2_{fo} is given by a curve fit of Thom's data (6) by

$$\phi^2_{fo,T} = \left[\left(0.97303(1-\chi) + \chi\,(\rho_L/\rho_g)\right)^{1/2}\left(0.97303(1-\chi) + \chi\right)^{1/2} + 0.027\,(1-\chi)\right]^2 \tag{3.65a}$$

The two-phase multiplier as used in Eq. 3.61 is related to the Thom two-phase multiplier by

$$\phi^2_{fo} = \phi^2_{fo,T}\ \frac{\rho}{\rho_L} \tag{3.65b}$$

The tube support plate resistances are calculated from

$$R_{tsp} = -\frac{K}{2}\ \frac{\rho\, U\, |\, \underline{U}\, |}{\Delta x} \tag{3.66}$$

where

K = form loss coefficient

Δx = axial increment

The form loss coefficients are a function of the restriction geometry. There are four regions in the tube support plate that require special values of K. They are 1) the main bundle with regular or preferential broaching, 2) the open lane or the circular lane, 3) the peripheral gap, and 4) the center untubed region. The values are obtained from Idelchick (10) for a thick orifice where K is given in tables which are functionally represented by

$$K = K\left(\frac{\ell}{D_r} , \frac{A_r}{A_o}\right) \tag{3.67}$$

where

ℓ = thickness of the restriction

= 1.5 inches for the tube support plate

D_r = hydraulic diameter of the restriction

A_r = restriction flow area

A_o = area downstream of the restriction

The values of K are given in Section 5.2 in connection with the regular and fine tube support plate models.

Cross-Flow Resistance

The resistance to flow in the radial and circumferential directions is given by

$$R_{r \text{ or } \theta} = -4 f' \frac{G_{max} |\underline{U}| \phi_{fo}^2}{t_p} \tag{3.68}$$

The factor f′ is given by the correlation of Jakob (11)

$$f' = \left[0.23 + \frac{0.11}{(X_t - 1)^{1.08}}\right] Re^{-0.15} \tag{3.69}$$

where

$X_t = \frac{\sqrt{3}\, t_p}{d}$ = ratio of transverse pitch to tube diameter d

$Re = \frac{\rho |\underline{U}| d}{\mu}$

The transverse pitch is the distance between identical tube rows perpendicular to the direction of flow. It can take on several values ranging from t_p to $\sqrt{3}\ t_p$ for triangular array of tubes. In this analysis, the maximum traverse pitch of $\sqrt{3}\ t_p$ was used.

G_{max} is the maximum cross-flow component of mass velocity. It occurs at the minimum flow opening with width equal to $t_p - d$. It is approximated by

$$G_{max} = \frac{\rho\ U_i\ \beta_b\ t_p}{t_p - d} \tag{3.70}$$

where

β_b = tube bundle porosity

U_i = V or W velocity

Heat Transfer Correlations

Correlations for the nucleate boiling, film boiling, and single-phase convection heat transfer coefficients are used to calculate the overall heat transfer coefficient given by Eq. 3.8. The thermal conductivity used in the overall heat transfer coefficient is given for Inconel 600 tubing by

$$k_m = 6.67 + 0.00642\ T_m : \text{Btu/ft-hr-°F} \tag{3.71}$$

where

T_m = average metal temperature, °F

$$T_m \approx \frac{T_p + T_s}{2}$$

Single-Phase Heat Transfer Coefficient

The single-phase heat transfer correlation is used for the primary side tube fluid and secondary side superheated steam regions. The correlation of Kays (12) is given by

$$\left.\begin{aligned} Nu &= 0.022\ Re^{0.8}\ Pr^{0.6} && Pr < 1 \\ Nu &= 0.0155\ Re^{0.83} Pr^{0.5} && Pr \geq 1 \end{aligned}\right\} \quad (3.72)$$

where

$$Nu = \frac{h_s\ D_h}{k}$$

$$Re = \frac{\rho\ |\underline{U}|\ D_h}{\mu}$$

$$Pr = \frac{C_p\ \mu}{k}$$

Nucleate Boiling Coefficient

Two nucleate boiling correlations were used in the analysis. A B&W proprietary correlation was applied to give the best estimate of overall thermal/hydraulic conditions. This correlation has been specifically developed from data obtained for the 19-tube once-through steam generator operating at flow conditions encountered in the actual operating units. The data is correlated in terms of boiling number Bo, the Martinelli parameter χ_{tt}, and liquid convective heat transfer coefficient, $h_{\ell o}$ expressed functionally as

$$h_{NB} = h_{NB}\ (Bo,\ \chi_{tt},\ h_{\ell o}) \quad (3.73)$$

where

$$Bo = \frac{q_s}{G\ h_{Lg}}$$

$$\chi_{tt} = \left(\frac{1 - x}{x}\right)^{0.9} \left(\frac{\rho_g}{\rho_L}\right)^{0.5} \left(\frac{\mu_L}{\mu_g}\right)^{0.1}$$

$$h_{\ell o} = 0.022\ \frac{k}{D_h} \left(\frac{G\ D_h\ (1 - x)}{\mu_L}\right)^{0.8} Pr^{0.6} \qquad Pr < 1$$

$$h_{\ell o} = 0.0155\ \frac{k}{D_h} \left(\frac{G\ D_h\ (1 - x)}{\mu_L}\right)^{0.83} Pr^{0.5} \qquad Pr \geq 1$$

The Chen(13) correlation was used for comparison with the B&W proprietary correlation. The correlation includes the contributions to the total boiling coefficient from two parts by

$$h_{NB} = h_{mic} + h_{mac} \tag{3.74}$$

h_{mic} accounts for nucleate boiling which occurs in the liquid film that surrounds the tube surface. h_{mac} accounts for forced convection vaporization which is prevalent at higher qualities when the liquid film becomes thinner. Under thin film conditions, the heat transfer is interpreted as forced convection through the film with rapid vaporization occurring at the liquid vapor interface.

h_{mic} is given by Chen as

$$h_{mic} = y\,(P_{sat})\,(\Delta T_{sat})^{0.24}\,(\Delta P_{sat})^{0.75}\,S \tag{3.75}$$

where

$$y\,(P_{sat}) = 0.00122\,\frac{k_L^{0.79}\,C_{PL}^{0.45}\,\rho_L^{0.49}\,g_c^{0.25}}{\sigma^{0.5}\,\mu_L^{0.29}\,h_{Lg}^{0.24}\,\rho_g^{0.24}}\text{, British Units} \tag{3.76}$$

ΔT_{sat} = $T_{wall} - T_{sat}$, F

ΔP_{sat} = difference in vapor pressure corresponding to ΔT_{sat}, lbf/sq. ft.

S = Chen's suppression factor which is a function of $(Re_L \cdot F^{1.25})$

$y\,(P_{sat})$ was computed in the units given by Chen for steam at various pressures and are given below.

P_{sat} (psia)	$y\,(P_{sat})$
200	3.85
500	3.72
700	3.74
900	3.83
1000	3.88
1200	4.06
1600	4.54

h_{mac} is defined by

$$h_{mac} = 0.023 \frac{k_L}{D_h} (Re_L)^{0.8} (Pr_L)^{0.4} F \tag{3.77}$$

where

$$Re_L = \frac{\rho |\underline{U}| (1-\chi)}{\mu_L}$$

$$Pr_L = \frac{C_{PL} \mu_L}{k_L}$$

The factors F and S are provided in graphical form by Chen. They are obtained from the following equations:

$$\left.\begin{aligned} F &= 2^{\exp\left[1.146596 \ell n \left(\frac{1}{\chi_{tt}}\right) + 0.408962\right]}, \quad \frac{1}{\chi_{tt}} \leq 0.7 \\ F &= \exp\left[0.723177 \ell n \left(\frac{1}{\chi_{tt}}\right) + 0.951086\right], \quad \frac{1}{\chi_{tt}} > 0.7 \end{aligned}\right\} \tag{3.78}$$

and

$$\left.\begin{aligned} S &= 1.0 - 0.2\left[\frac{\ell n\ (Re)}{9.903488}\right]^{9.575930}, && 1 < Re < 2 \times 10^4 \\ S &= -0.260577 \ell n\ (Re) + 3.380618, && 2 \times 10^4 \leq Re \leq 2 \times 10^5 \\ S &= 0.2\left[\frac{12.20607}{\ell n\ (Re)}\right]^{9.575930}, && Re > 2 \times 10^5 \end{aligned}\right\} \tag{3.79}$$

where

$$Re = Re_L \cdot F^{1.25}$$

Film Boiling

The film boiling coefficient is obtained from a linear interpolation with respect to quality of the secondary side heat transfer resistances from the nucleate boiling and single-phase steam correlations by

$$\frac{1}{h_{FB}} = \frac{1}{h_{NB}} + \left(\frac{1}{h_{SH}} - \frac{1}{h_{NB}}\right)\left(\frac{\chi - \chi_{DO}}{1 - \chi_{DO}}\right) \tag{3.80}$$

where

h_{NB} = nucleate boiling coefficient at $\chi = \chi_{DO}$

h_{SH} = single-phase heat transfer coefficient at $\chi = 1.0$

This simple correlation provides good agreement with data obtained from laboratory steam generator tests.

Film Dryout Quality

Experimental data for the laboratory once-through steam generators has indicated film dryout occurs at a constant quality of 95%, thus

$$\chi_{DO} = 0.95 \tag{3.81}$$

Section 4

NUMERICAL SOLUTION METHOD

4.1 FINITE-DIFFERENCE GRID

The solution procedure is a finite-difference method which is described in References 1, 2, and 3. An orthogonal grid is constructed by specifying surfaces of constant x, constant r, and constant θ. The points of intersection of the user specified surfaces are the main grid points or nodes as illustrated in Figure 4.1. The solution method aims at calculating the values of all the dependent variables at the grid points. This is done by converting the differential equations into algebraic finite-difference equations and solving the resulting set of algebraic equations.

The finite-difference equations are constructed by integrating the partial differential equations for conservation of mass, momentum, and energy over several distinct control volumes. A main control volume shown in Figure 4.1A is used for both the continuity and energy equations. The six faces of the main control volume are positioned half-way between the neighboring main grid points. The values of fluid properties such as enthalpy, pressure, and density are defined at the main grid points. The velocities U, V, and W, however, are staggered and are thus defined at the faces of the main control volumes.

The use of a staggered grid is a particular feature of the solution procedure. As shown in Figures 4.1B through 4.1D, the axial, radial, and circumferential momentum equation control volumes are staggered in the x, r, and θ directions, respectively. With this scheme, the U, V, and W velocities are situated within the momentum equation control volumes in the same manner as density and enthalpy are situated within the main control volumes for the continuity and energy equations. With a staggered grid, the difference in pressure between any two adjacent nodes can be envisioned as driving the velocity component lying between them which closely approximates the real physical situation.

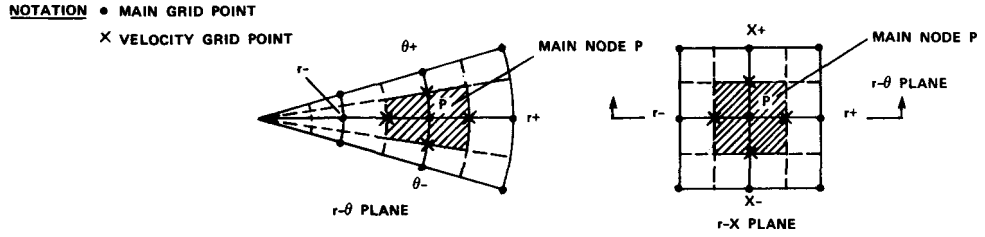

FIGURE 4.1A CROSS-SECTIONS OF THE MAIN CONTROL VOLUME FOR THE CONTINUITY AND ENERGY EQUATIONS (SHADED AREAS)

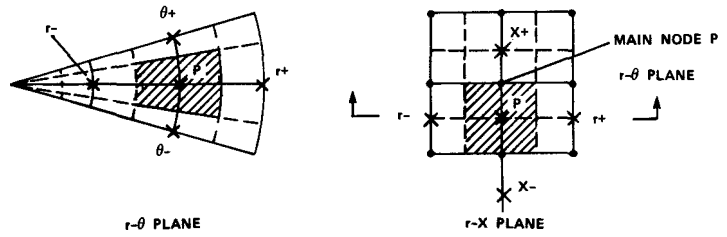

FIGURE 4.1B CROSS-SECTIONS OF THE AXIAL MOMENTUM EQUATION CONTROL VOLUME (SHADED AREAS)

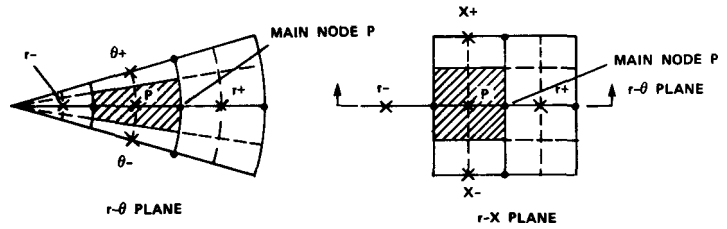

FIGURE 4.1C CROSS-SECTIONS OF THE RADIAL MOMENTUM EQUATION CONTROL VOLUME (SHADED AREAS)

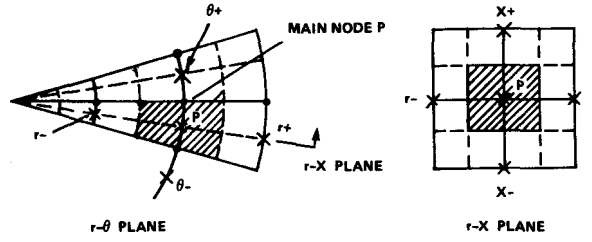

FIGURE 4.1D CROSS-SECTIONS OF THE CIRCUMFERENTIAL MOMENTUM EQUATION CONTROL VOLUME (SHADED AREAS)

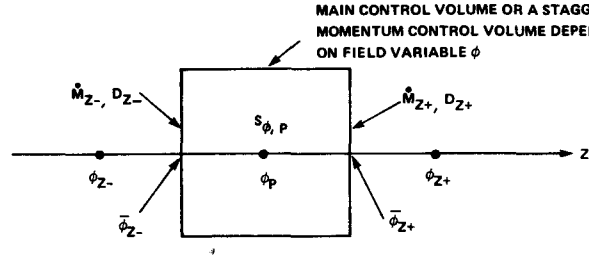

FIGURE 4.1E LOCATIONS OF FINITE-DIFFERENCE GRID VARIABLES USED IN EQUATION 4.3 (z = x, r, or θ)

4.2 SOLUTION METHODS FOR THE CONSERVATION EQUATIONS

Each of the six conservation equations can be put into the general form

$$\nabla\cdot(\beta\rho\underline{U}\phi) = \nabla\cdot(\beta\Gamma_\phi\nabla\phi) + S_\phi \tag{4.1}$$

where Γ_ϕ is the diffusion coefficient, S_ϕ is the source term, and ϕ is the dependent variable in question. For example, if the dependent variable is axial velocity, then Eq. 4.1 becomes

$$\nabla\cdot(\beta\rho\underline{U}\,U) = \nabla\cdot(\beta\mu_t\nabla U) + S_U \tag{4.2}$$

Here, the source term, S_U, includes the pressure gradient, gravitational force, and resistance terms. Verbally, the conservation equations can be expressed as

convection = diffusion + source terms

It should also be noted that Eq. 4.1 can also represent the continuity equation with $\phi = 1$ and $S_\phi = 0$.

The convenience in expressing the governing equations in one common form lies in the fact that a single approach can be used to obtain the finite-difference equations. If each of the conservation equations are integrated over their respective control volumes shown in Figure 4.1E, then the general form of the finite-difference equations becomes

$$z = \sum_{x,r,\theta} (\dot{m}_{z+}\,\overline{\phi}_{z+} - \dot{m}_{z-}\,\overline{\phi}_{z-}) \tag{4.3}$$

$$= \sum_{z=x,r,\theta} \left[D_{z+}\,(\phi_{z+} - \phi_p) - D_{z-}\,(\phi_p - \phi_{z-})\right] + S_{\phi,p}\,(Vol)_p$$

where

ϕ_z = value of ϕ at point z

$\overline{\phi}_z$ = a weighted average of ϕ at the control volume face z

$\dot{m}_z = (\beta\rho U_i)_z\,A_z$ = mass flow rate passing through control volume face z

$D_z = \frac{(\beta\Gamma_\phi)_z A_z}{\Delta z}$ = diffusion coefficient at control volume face z

A_z = control volume surface area perpendicular to direction z

Δz = distance between point p and any of the six adjacent nodes
= Δx, Δr, and $r\Delta\theta$

$S_{\phi,p}$ = source term for control volume p

$(Vol)_p$ = volume of control volume p

By observing the control volumes and noting the locations where velocities and fluid properties are defined, it can be readily seen that interpolation is required to evaluate the $\dot{m}_z$ and D_z terms. The use of a staggered grid makes it convenient to calculate $\dot{m}_z$ for the continuity and energy equations since velocities are defined at the main control volume faces. In THEDA, a linear interpolation scheme is used to evaluate $\dot{m}_z$ and D_z for the momentum equations. In this scheme, mass flow rates and diffusion coefficients are first calculated for the faces of the main control volumes; then a linear interpolation of the main control volume values yields $\dot{m}_z$ and D_z for the faces of the staggered momentum control volumes.

Another important feature of the solution method is hybrid differencing which combines both central and upwind differencing for the evaluation of $\overline{\phi}_z$ in Eq. 4.3. By the central difference approximation, the values of ϕ at the z+ and z- faces of the control volumes are

$$\overline{\phi}_{z+} = \frac{\phi_{z+} + \phi_p}{2} \tag{4.4}$$

$$\overline{\phi}_{z-} = \frac{\phi_p + \phi_{z-}}{2} \tag{4.5}$$

The weighting factor of one-half in these equations is appropriate for the energy equation since the location of $\bar{\phi}$ is half-way between the enthalpy grid points (main grid points). For the momentum equations, this weighting is appropriate for four of the six faces of each momentum equation control volume. For the two faces that are perpendicular to the staggered direction, this weighting is only an approximation when the grid spacing is non-uniform since $\bar{\phi}$ in this case is not half-way between the velocity grid points.

It has been shown that when convective transport is of a much larger magnitude than diffusion (large local cell Reynolds and Peclet numbers), it is required for a stable solution procedure that the convection term can only be influenced by the value of the variable upstream of the node location. Thus, if

$$\left| \frac{\dot{m}_{z+}}{D_{z+}} \right| >> 0 \quad \text{and} \quad \left\{ \begin{array}{lll} \dot{m}_{z+} > 0, & \bar{\phi}_{z+} = & \phi_p \\ \dot{m}_{z+} < 0, & \bar{\phi}_{z+} = & \phi_{z+} \end{array} \right\} \tag{4.6}$$

and if

$$\left| \frac{\dot{m}_{z-}}{D_{z-}} \right| >> 0 \quad \text{and} \quad \left\{ \begin{array}{lll} \dot{m}_{z-} > 0, & \bar{\phi}_{z-} = & \phi_{z-} \\ \dot{m}_{z-} < 0, & \bar{\phi}_{z-} = & \phi_p \end{array} \right\} \tag{4.7}$$

Here, $\dot{m}_z/D_z$ represents a local cell Reynolds number for the momentum equations and a local Peclet number for the energy equation. Note also that the cell Reynolds and Peclet numbers are based on a turbulent rather than laminar diffusion coefficient.

Both the central and upwind differencing methods are combined into a hybrid differencing method. With this method, central differencing provides a stable and accurate solution for local cell Reynolds and Peclet numbers with absolute values less than 2. For Reynolds and Peclet numbers greater than 2 and less than -2, central differencing is replaced by upwind differencing and the diffusion term is neglected. Using these assumptions and applying the continuity equation, the finite-difference equations for momentum and energy can be written in the form

$$a_p\phi_p = a_{x-}\phi_{x-} + a_{x+}\phi_{x+} + a_{r-}\phi_{r-} + a_{r+}\phi_{r+} + a_{\theta-}\phi_{\theta-} + a_{\theta+}\phi_{\theta+} + b \tag{4.8}$$

where

$$a_p = \sum_z a_z = a_{x-} + a_{x+} + a_{r-} + a_{r+} + a_{\theta-} + a_{\theta+}$$

With hybrid differencing

$$a_{z+} = D_{z+} - \frac{\dot{m}_{z+}}{2} \quad , \quad -2 < \frac{\dot{m}_{z+}}{D_{z+}} < 2 \tag{4.9a}$$

$$a_{z+} = 0 \quad , \quad \frac{\dot{m}_{z+}}{D_{z+}} \geq 2 \tag{4.9b}$$

$$a_{z+} = -\dot{m}_{z+} \quad , \quad \frac{\dot{m}_{z+}}{D_{z+}} \leq -2 \tag{4.9c}$$

$$a_{z-} = D_{z-} + \frac{\dot{m}_{z-}}{2} \quad , \quad -2 \leq \frac{\dot{m}_{z-}}{D_{z-}} < 2 \tag{4.10a}$$

$$a_{z-} = \dot{m}_{z-} \quad , \quad \frac{\dot{m}_{z-}}{D_{z-}} \geq 2 \tag{4.10b}$$

$$a_{z-} = 0 \quad , \quad \frac{\dot{m}_{z-}}{D_{z-}} \leq -2 \tag{4.10c}$$

$$b = S_{\phi,p} (Vol)_p = \text{source term}$$

Each of the "a" coefficients thus represents the convection and diffusion transport across one of the faces of the control volume. When the flow is dominated by convective transport, Eq. 4.9b and 4.10c imply that downstream values cannot influence the value of a variable at a grid point.

For each of the governing equations, there is an algebraic finite-difference equation at each node of the form given by Eq. 4.8. To solve the problem, each of those equations must be solved simultaneously. Note, that the problem is very non-linear and the "b" term in Eq. 4.8 usually contains functions of ϕ itself. Thus, the problem cannot be solved by a direct procedure, but must be solved by an iterative technique. The technique used is called a line-by-line (LBL) method. In the LBL solution, the set of equations for one variable along a single coordinate

line is solved simultaneously. All variables other than that under consideration for the particular line are treated as known values. A tri-diagonal matrix algorithm and the boundary conditions presented in Section 5.1 are then applied to solve the resulting set of equations. This procedure is repeated for every line in the first coordinate direction and then repeated in the second and finally the third coordinate direction.

4.3 PRESSURE SOLUTION METHOD

The governing equations in Section 3.1 form a complete set of six partial differential equations in terms of six unknown quantities -- U, V, W, P, h, and h_t. It should be noted that all six variables do not appear explicitly in all six equations. The problem is to solve for all six variables and satisfy all six equations simultaneously. In particular, the three momentum equations must be solved for all three velocities, and the continuity equation must be simultaneously satisfied and the unknown pressure determined. The method used to solve this problem is outlined in References 1, 2, and 3.

The procedure is as follows: First, initial values are assumed for all variables. These initial estimates can be, for example, the results from a one-dimensional analysis or the results from a previous analysis. Refer to Section 4.4 for further discussion of the effect of initial estimates on convergence. The three momentum equations are then solved for the velocities U*, V*, and W*. It should be noted that no information has yet been included from the continuity equation and, in general, these velocities do not satisfy continuity. The initial velocities are then corrected by amounts U', V', and W' such that the continuity equation is satisfied, i.e.

$$U = U^* + U' \tag{4.11}$$

$$V = V^* + V' \tag{4.12}$$

$$W = W^* + W' \tag{4.13}$$

or in general notation

$$U_i = U_i^* + U_i' \tag{4.14}$$

To solve for the velocity corrections, pressure corrections P' defined by

$$P = P^* + P' \tag{4.15}$$

are determined so that both the continuity and momentum equations are satisfied.

A system of equations for the pressure corrections are obtained by combining the continuity and momentum equations. First, the momentum equations defined by Eq. 4.8 can be written as

$$a_p U^*_{i,z-} = \sum_z a_z U^*_{i,z} - \beta_{z-} A_{z-} (P^*_p - P^*_{z-}) + b' \tag{4.16}$$

Here, the source term b has been broken up into the pressure gradient term and the remaining source terms which are contained in b'. Eq. 4.16 has been written for U, V, and W momentum equation control volumes that are centered about three z- faces of the main control volume as shown in Figure 4.2. A similar expression can be written for the U, V, and W momentum equation control volumes centered about the three z+ faces of the main control volume.

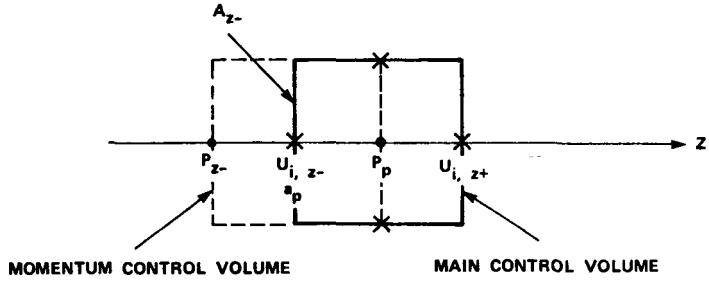

FIGURE 4.2 LOCATIONS OF PRESSURES AND VELOCITY IN THE PRESSURE CORRECTION SCHEME

To obtain a system of equations that can be used to solve for pressure, an approximate form of each momentum equation is used. The approximation is made by assuming that the six neighboring velocities and b' can be approximated with previous iteration values. The velocity centered within the momentum control volume and the pressure difference are taken as improved values. The momentum equations can then be written as

$$a_p U_{i,z-} \simeq \sum_z a_z U^*_{i,z} - \beta_{z-} A_{z-} (P_p - P_{z-}) + b' \qquad (4.17)$$

By subtracting Eq. 4.16 from Eq. 4.17, the following expression is obtained

$$U'_{i,z-} \simeq - \frac{\beta_{z-} A_{z-}}{a_p} (P'_p - P'_{z-}) \qquad (4.18)$$

or verbally, the velocity correction is proportional to the difference in the pressure corrections. Another way of viewing this equation is that the pressure correction "drives" the velocity correction.

The velocity corrections are then substituted into the continuity equation to obtain an algebraic finite-difference equation for the pressure corrections. The continuity equation for the main control volume in Figure 4.2 is written in terms of velocity corrections as

$$\sum_{z = x,r,\theta} (\beta_{z+} \rho_{z+} A_{z+} U'_{i,z+} - \beta_{z-} \rho_{z-} A_{z-} U'_{i,z-}) = -R_p \qquad (4.19)$$

It can be readily seen that insertion of the velocity corrections given by Eq. 4.18 into Eq. 4.19 yields a finite-difference equation for pressure corrections of the same form as Eq. 4.8. The continuity equation residual R_p becomes a source term for each pressure correction equation. It is explicitly calculated by

$$R_p = \sum_{z = x,r,\theta} (\beta_{z+} \rho_{z+} A_{z+} U^*_{i,z+} - \beta_{z-} \rho_{z-} A_{z-} U^*_{i,z-}) \qquad (4.20)$$

With R_p known, the finite-difference equations for pressure corrections are then solved and the velocities are updated with Eq. 4.18.

Note that the assumed direct relationship between the velocity and pressure corrections is only an approximation due to Eq. 4.17, but making this assumption allows the linkage of the velocity and pressure solutions. With this procedure, both the continuity and momentum equations are satisfied as U'_i and P' approach zero as the solution converges.

The overall solution procedure is illustrated in Figure 4.3. Note that after the pressure and velocity corrections are made, the primary and secondary side energy equations are solved and the next iteration can begin.

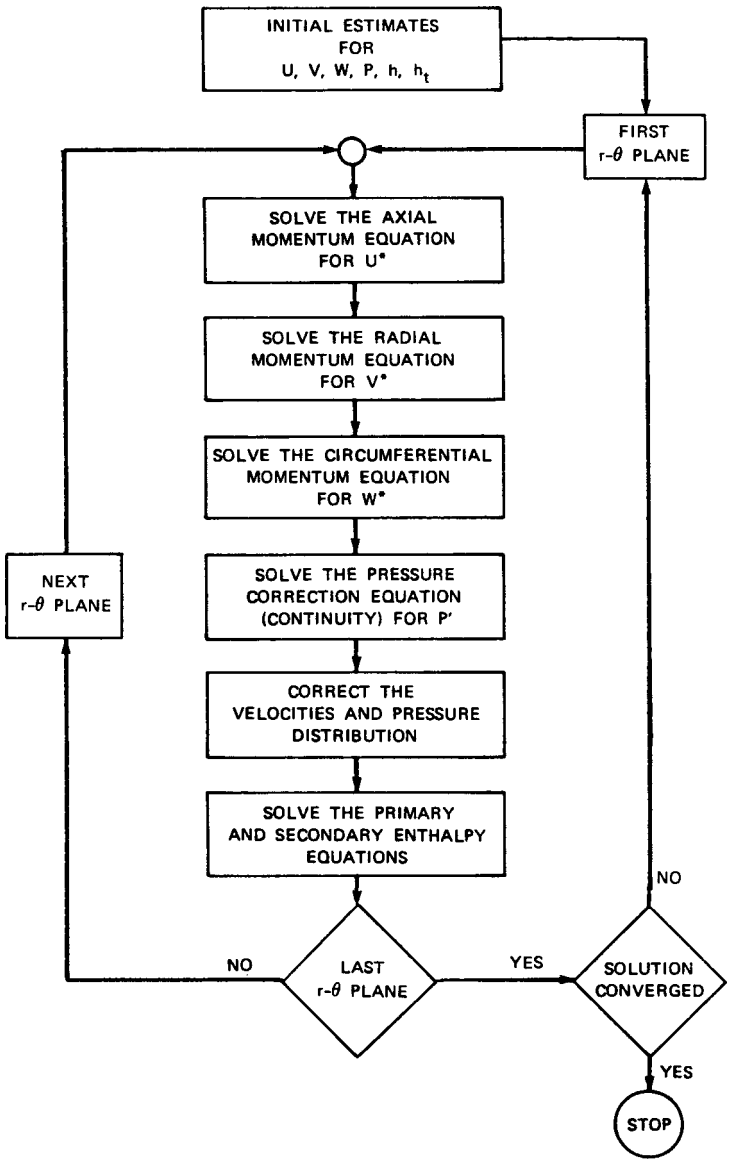

FIGURE 4.3 OUTLINE OF THE THEDA–1 SOLUTION PROCEDURE

4.4 CONVERGENCE PARAMETERS

The convergence of the solution procedure depends on many factors including the inherent non-linearity of the problem, the initial accuracy of the guesses, and the relaxation factors used during the iteration procedure. It is possible that the overall solution may converge to a reasonable solution while conditions in small local regions are inadequately converged. Each solution must be examined by the user to determine if it has converged to a reasonable degree.

Several convergence parameters are monitored as part of the calculation process to ensure that the solution procedure is converging to a stable solution. These parameters include residuals for the finite-difference equations, primary and secondary side heat balance, and typical values for velocity and enthalpy at arbitrary locations within the steam generator. The parameters are given after each iteration.

Normally, a THEDA run is made with many restarts of the calculation process. Each restart typically consists of 30 iterations. After each restart, the steam generator conditions are printed out for each grid point to provide a further check of convergence.

The finite-difference equation residuals are provided for the continuity equation and the x, r, and θ momentum equations. The continuity equation residual, R_p, as defined by Eq. 4.20, is given for each main control volume. The momentum equation residuals, R_ϕ , are obtained after the coefficients and source terms have been calculated but before these terms are used to calculate U*, V*, and W*. Thus, the momentum equation residuals are the differences of the right- and left-hand sides of Eq. 4.8 with the velocities from the previous iteration used for the ϕ's, the coefficients, and the source terms.

Since R_p has a unit of mass flow rate and the R_ϕ's have units of momentum, the residuals have been normalized to some physical quantity. For the continuity equation residual, the total steam flow rate is used, and for the momentum residuals, the total steam outlet momentum is applied. The maximum and average normalized residuals are included as part of the print-out information as shown in Table C.3 of Appendix C. The print-outs include then:

$$\overline{R}_{p,\,max} = \max \left| \overline{R}_{p,n} \right| \tag{4.21}$$

$$\overline{R}_{p,\,ave} = \frac{1}{N} \sum_{n=1}^{N} \left| \overline{R}_{p,n} \right| \tag{4.22}$$

where

$\overline{R}_{p,n} = R_{p,n} / \dot{m}_{SG}$

N = total number of main control volumes

$\dot{m}_{SG}$ = steam flow rate

and for the momentum equations

$$\overline{R}_{\phi,max} = \max \left| \overline{R}_{\phi,n} \right| \tag{4.23}$$

$$\overline{R}_{\phi,ave} = \frac{1}{N} \sum_{n=1}^{N_\phi} \left| \overline{R}_{\phi,n} \right| \tag{4.24}$$

where

$$\overline{R}_{\phi,n} = R_{\phi,n} \frac{\rho_{ex} A_{ex}}{\dot{m}_{SG}^2}$$

ρ_{ex} = outlet steam density

A_{ex} = steam outlet area between the upper shroud and upper tubesheet

N_ϕ = total number of momentum control volumes for variable ϕ

An energy balance is made to check the agreement between the primary and secondary side solutions. The energy balance calculates the total heat transfer to the secondary side fluid and the total heat transfer from the primary side fluid. These heat transfer quantities are not calculated from the local heat transfer at each cell, but are calculated from the inlet and exit conditions on the primary and secondary side. For the secondary side, the total heat transfer is calculated from the given feedwater flow rates and temperature and an overall average exit enthalpy, i.e.,

$$Q_{sec} = \dot{m}_{FW} (\tilde{h}^{s}_{ex} - h_{FW}) \tag{4.25}$$

where

Q_{sec} = secondary side heat transfer

$\dot{m}_{FW}$ = given feedwater flow rate

h_{FW} = given feedwater enthalpy

$\tilde{h}^{s}_{ex}$ = calculated average exit enthalpy

The average exit enthalpy is calculated from the local values at the exit plane by

$$\tilde{h}^{s}_{ex} = \frac{\sum \dot{m}_i \, h_i^{s}}{\dot{m}_{FW}} \tag{4.26}$$

where the summation is over all the exit plane nodes and $\dot{m}_i$ is the exit mass flow rate at each of these nodes.

The primary side heat transfer is calculated in a similar manner. The primary side heat transfer is given by

$$Q_t = \dot{m}_t (h_{in} - \tilde{h}^{t}_{ex}) \tag{4.27}$$

where

Q_t = primary side heat transfer

$\dot{m}_t$ = primary side flow rate

h_{in} = given primary inlet enthalpy

$\tilde{h}^{t}_{ex}$ = calculated average primary exit enthalpy

The primary side average exit enthalpy is calculated from

$$\tilde{h}^t_{ex} = \frac{\sum \dot{m}^t_i \, h^t_i}{\dot{m}_t} \tag{4.28}$$

The indicated summation is over all of the primary side exit plane control volumes. $\dot{m}^t_i$ is the primary side flow rate in each of these control volumes and h^t_i is the exit plane enthalpy for each of these control volumes.

The print-out information given after each iteration includes Q_t, Q_{sec}, and the percent difference between these values.

Section 5

OTSG MODEL DESCRIPTION

There are several areas in the THEDA analysis where detailed local geometric features of the steam generator are modeled. In the following sections, the method used to represent these features in the two OTSGs will be discussed.

5.1 BOUNDARY CONDITIONS

To include the necessary boundary conditions, special control volumes are used at the boundaries (i.e., walls, openings, or the centerline) as shown in Figures 5.1 and 5.2. For main control volumes adjacent to a boundary as shown in Figure 5.1, the mass flow rate at the z+ face is calculated with a specified velocity. This velocity is zero if the boundary is a wall or the centerline. It is a predefined value if the boundary is an opening. If the boundary is an inlet, the velocity is a prescribed inlet condition. If the boundary is an exit, the velocity is calculated using a continuative outflow condition. The diffusion term at z+ for the energy equation, as defined in Eq. 4.3, is set to zero at all boundaries. This is equivalent to a zero gradient or adiabatic boundary condition at all boundaries. The momentum equation control volume shown in Figure 5.2 extends from main node z- to the boundary rather than from main node z- to main node p which is done for the interior momentum equation control volumes. The mass flow rate for the z+ face is identical to $\dot{m}_{z+}$ for the main control volume in Figure 5.1. The diffusion term for the z+ face of the momentum control volume is also set to zero to provide the required zero gradient boundary condition. In addition, the pressure gradient between main nodes z- and p is set equal to the pressure gradient between main nodes z- and z+, so that the pressure at main node p is the last pressure solved for within the solution domain rather than P_{z+}.

The current version of the code assumes a uniform distribution of all variables at the inlet to the generator. The inlet ports in the shroud are not modeled and the inlet area is assumed to be completely open around the circumference. The inlet flow is assumed to be saturated liquid and all secondary inlet properties are evaluated at the saturated liquid conditions.

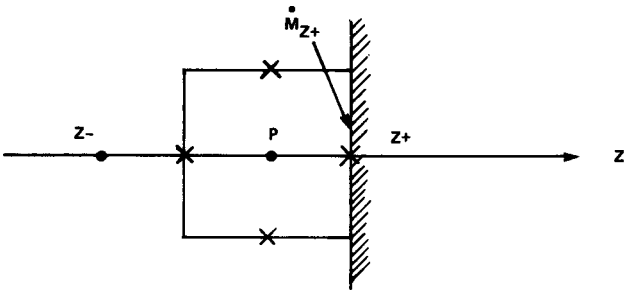

FIGURE 5.1 MAIN CONTROL VOLUME AT A BOUNDARY

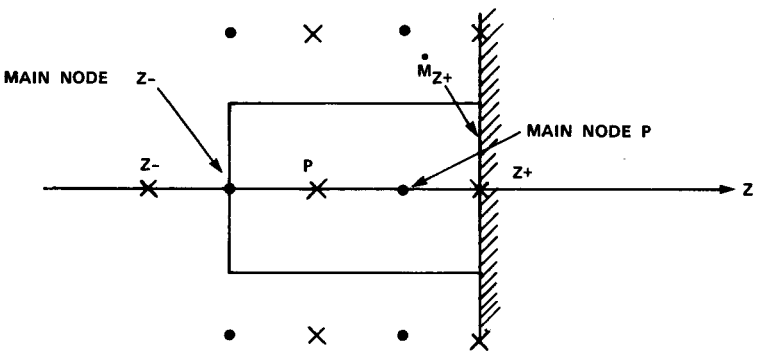

FIGURE 5.2 MOMENTUM CONTROL VOLUME AT A BOUNDARY

The exit plane boundary conditions are of the continuative outflow type. This means that two factors are considered in determining the exit boundary values for all variables. First, since the diffusion term is zero and the flow is out of the exit plane, the a_{Z+} coefficients for the control volumes adjacent to the exit plane are zero due to hybrid differencing. This eliminates the direct coupling of the exit plane variables from the field variables adjacent to the exit plane during the solution of the energy and momentum equations. Once the momentum equations are solved, the exit plane velocities can be explicitly calculated based on mass conservation for each of the main control volumes adjacent to the exit plane. These velocities, however, do not in general yield mass flow rates which satisfy global continuity when integrated over the exit plane. The second constraint at the exit plane is, therefore, that the mass flow rates satisfy overall continuity for the steam generator. To accomplish this, the exit plane velocity profile is adjusted such that continuity is satisfied. These adjusted exit plane velocities enter into the solution process through the pressure correction scheme via the R_p term defined by Eq. 4.20. In this case, the appropriate $U^*_{i,Z+}$ velocity in Eq. 4.20 is set equal to the adjusted exit plane velocity.

The bleed flow rate is calculated from the local secondary side flow conditions. The bleed flow rate is determined from energy balance considerations only and does not consider momentum conservation. From experimental measurements, it is known that the bleed flow rate is sufficient to preheat the flow to a saturated state at the inlet to the bundle. The bleed flow rate is calculated to provide saturated liquid at the bundle inlet from local flow conditions at the bleed port.

5.2 TUBE SUPPORT PLATES

The tube support plates in the two steam generators have several different regions which provide a varied amount of resistance to flow. Regions common to the tube support plates in both units include the main broached region, the outer periphery, and the center untubed region. For TMI-2, the outer periphery is partially blocked to flow, whereas the outer periphery for DB-2 is totally blocked. As shown in Section 2, the steam generators also have untubed lanes. In TMI-2, the inspection lane is open at the support plates and the resistance to flow is small compared to the resistance in the surrounding broached region. In DB-2, the manway cover lane is mostly blocked, but a small amount of flow area is available from part of the broached areas from the tubes on the boundaries of the manway lane.

In THEDA, two levels of detail are used to model the tube support plates. In the regular support plate model (RSP), the tube support plates are situated at the center of large axial momentum equation control volumes as shown in Figure 5.3. The porosity in the control volumes is equal to either the bundle porosity of 0.537, or 1.0 if the region is without tubes. With this model, the K factor in Eq. 3.66 is based on the average axial velocity calculated at the velocity grid point. This velocity is not equal to the much higher axial velocity that actually occurs within the support plate due to the area reduction.

The RSP model K factors are obtained from Idelchik as discussed in Section 3.3. The values are: 4.18 for main broached tube region, 0.5 for the open lane, 23.5 for preferentially broached region, 61.5 for the manway lane, 268 for the manway lane with adjacent tubes preferentially broached, and 417 for the center untubed region.

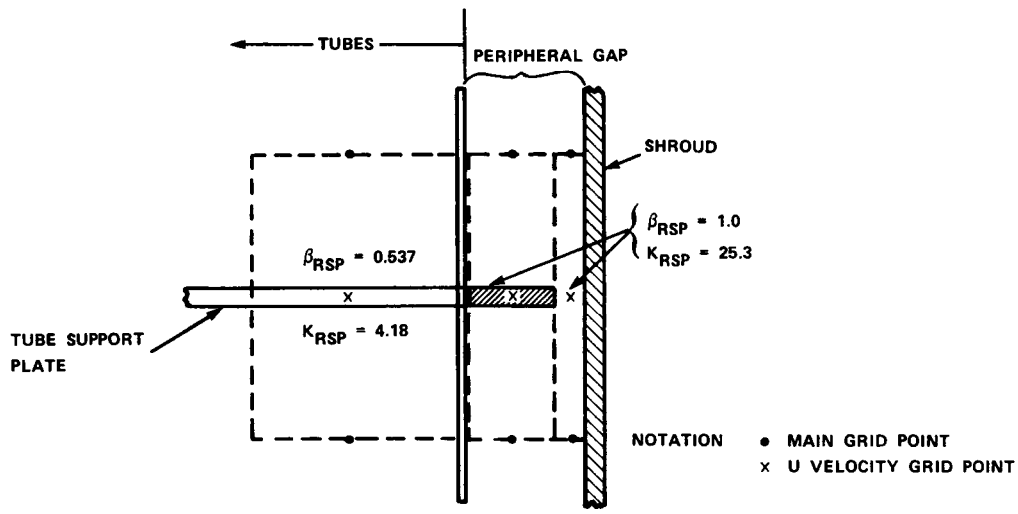

FIGURE 5.3 REGULAR SUPPORT PLATE MODEL (RSP)

In the RSP model, special consideration is given to the peripheral gap region. For the partially open peripheral gap for TMI-2, an equivalent hydraulic diameter and area ratio are used in Eq. 3.67 to obtain a K factor equal to 25.3. This averaged K factor is used in the axial momentum control volumes for both the peripheral gap opening and the blockage as shown in Figure 5.3. For DB-2, the peripheral gap is totally blocked and a large K factor of 1000 is used.

A higher level of detail is obtained with the fine grid support plate (FGSP) model. As shown in Figure 5.4, the FGSP model uses four axial nodes at the support plates. The axial momentum equation control volume that is centered about the support plate contains the actual tube support plate porosity. This porosity is 0.232 for the main broached tube region, 0.717 for the open lane, 0.128 for the preferentially broached region, 0.148 for the manway lane, 0.081 for the manway lane with adjacent tubes preferentially broached, and 0.059 for the center untubed region. Since the FGSP model calculates the actual velocity in the support plate, the K factor used in Eq. 3.66 is based on the tube support plate velocity. The FGSP K factors are related to RSP K factors by the following relation

$$K_{FGSP} = f\, K_{RSP} \left(\frac{\beta_{FGSP}}{\beta_{RSP}} \right)^2 \qquad (5.1)$$

where

K_{FGSP} = fine grid K factor

K_{RSP} = regular grid K factor

β_{FGSP} = porosity in the tube support plate

β_{RSP} = porosity downstream of the tube support plate

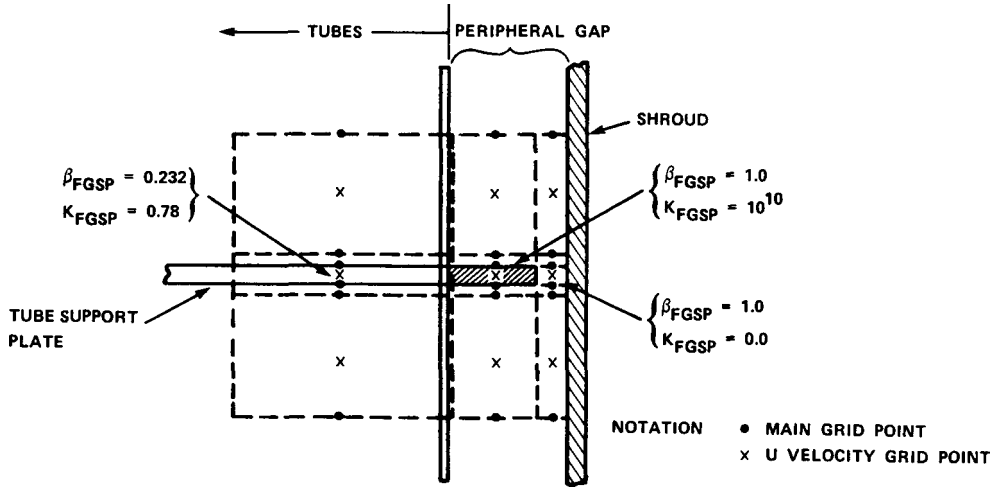

FIGURE 5.4 FINE GRID SUPPORT PLATE MODEL (FGSP)

The factor f is used to obtain equal tube support plate pressure drops for the RSP and FGSP models. For the sensitivity study and for other analyses performed within B&W, it has been found that the FGSP model with f = 1.0 overpredicts the tube support plate pressure drop. Runs have been made with the FGSP K factor, friction factor, and diffusion coefficients set to zero. In this case, one would expect a pressure reduction within the tube support plate and then a recovery of the original pressure downstream of the support plate. However, THEDA-1 predicts a net loss of pressure on the order of one velocity head. A preliminary examination of these results has shown that this false pressure drop is due to the upwind differencing of the axial velocity in the convective term of the momentum equation. The upwind differencing scheme used in THEDA-1 applies the velocities at the velocity grid points to the faces of the momentum control volumes. It has been shown, however, that this assumption leads to an inaccurate calculation of the momentum change across the control volume when the porosity at the velocity grid point differs from the porosity at the

control volume face. The necessary modifications to THEDA-1 to correct this problem are currently under development. For the computer runs presented in this report, these modifications were not available. Instead, the factor f (Eq. 5.1) was applied to give agreement between the FGSP and RSP tube support plate pressure drops. The actual value of f will be shown to be 0.487 in Section 6.2.3.

The primary advantage of FGSP model is that completely blocked regions can be modeled with greater detail than with the RSP model. This is accomplished by setting the K factors to 1×10^{10} for the axial, radial, and circumferential momentum equation control volume that lie within the support plate blockage. This effectively forces the velocities in the blockage to zero and thus, by continuity considerations, diverts the flow around the blockage. The blocked regions include the peripheral gap for all support plates in DB-2 and the top and bottom support plates in TMI-2, part of the peripheral gap for TMI-2 support plates 2 through 14, and the unbroached outer rim on the top TMI-2 support plate.

5.3 OTSG GRID

OTSG grids are set up to model the geometric details described in Section 2 for both TMI-2 and DB-2. These grids are used in both the sensitivity study and best estimate analysis. Main node points given in Appendix A are specified so that the boundaries of the main control volumes coincide with local geometric details. Exceptions to this are the open lane for TMI-2 and the DB-2 manway lane. In these cases, approximations are made since the shapes of the tube free areas do not fit into the cylindrical coordinate system.

The r-θ grid for TMI-2 is shown in Figure 5.5. One hundred and eighty (180) degree symmetry is used with 11 circumferential nodes and 12 radial nodes. The first and last nodes lie on the boundaries so that there are 9 control volumes in the circumferential direction and 10 in the radial direction.

The open lane is modeled with a pie-shaped segment adjacent to the symmetry boundary at $\theta = 0°$. The arc length of the segment is equal to one-half the width of the open lane at the outer radius. For all x and r values within this segment, the porosities are set to unity and the primary flow rates to zero and thus, the tube heat fluxes are set to zero. Two other segments with small $\Delta\theta$ are positioned next to the main segment. At several radial positions,

these segments intersect both the open lane and tubed area. For the control volumes within these segments, the porosities and primary flow rates are adjusted by interpolation to account for the presence of the open lane.

The r-θ grid for DB-2 is shown in Figure 5.6. There are 11 circumferential nodes and 15 radial nodes. The circular shaped manway lane has been approximated by the main control volumes shown in Figure 5.4. As is the case with the TMI-2 open lane, the porosities within the manway lane control volumes are set to unity and primary flow rates are set to zero. The total cross-sectional area of the manway lane control volumes is equal to the area of the actual manway lane. Therefore, the shape is only approximate, but the total number of missing tubes is accurately represented.

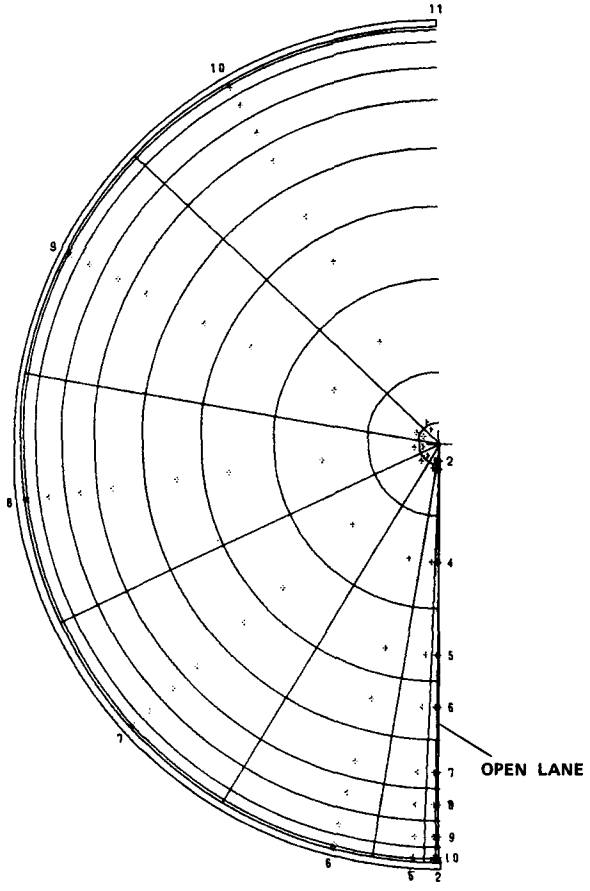

FIGURE 5.5 TMI-2 R-θ GRID SHOWING THE MAIN CONTROL VOLUMES

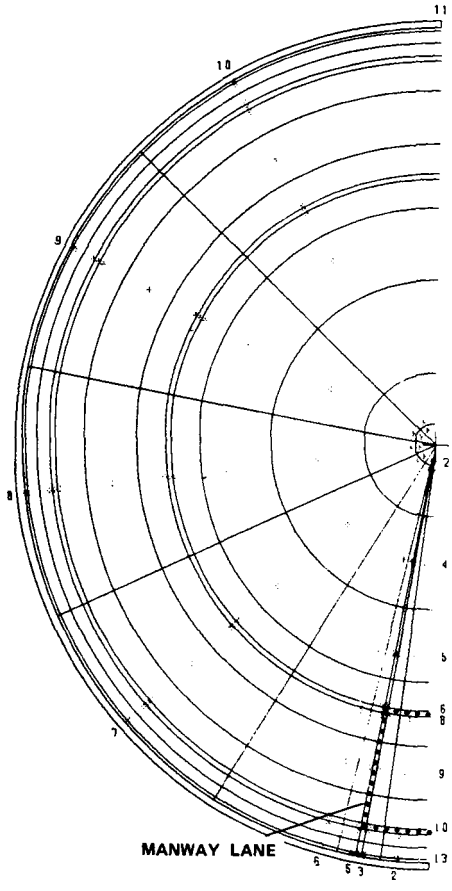

FIGURE 5.6 DB-2 R-θ GRID SHOWING THE MAIN CONTROL VOLUMES

The r-x grids for TMI-2 and DB-2 are shown in Figures 5.7 and 5.8. Two axial nodes are used to model the inlet port, one node is used at the bleed port, and one at the exit port. There are 55 axial nodes with regular support plate models for most of the support plates. Four fine grid support plate models are used for the 1st, 9th, 10th, and uppermost tube support plates. These models provide additional modeling detail near the inlet, exit, and bleed ports.

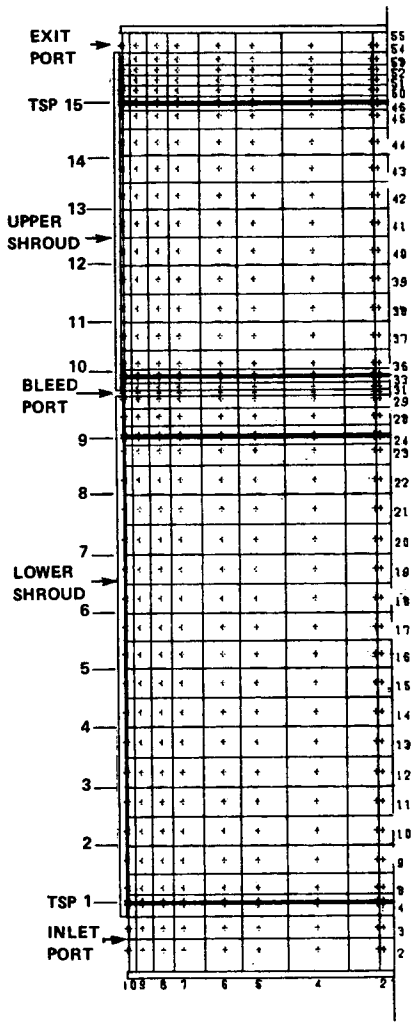

FIGURE 5.7 TMI-2 R-X GRID SHOWING THE MAIN CONTROL VOLUMES

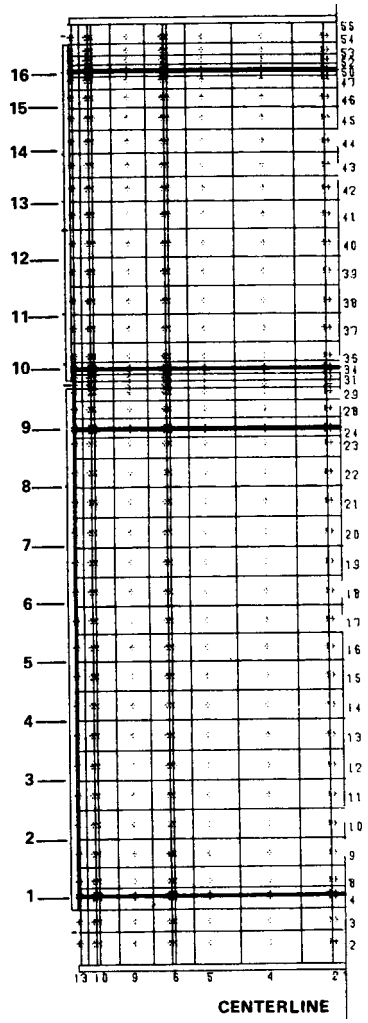

FIGURE 5.8 DB-2 R-X GRID SHOWING THE MAIN CONTROL VOLUMES

The peripheral gap and center untubed regions have shapes that fit well into the cylindrical coordinate system. The peripheral gap is modeled with radial nodes 10 and 11 for TMI-2 and nodes 13 and 14 for DB-2. The center untubed region is modeled with radial node 2 in each steam generator. The porosities are set to unity and the primary flow rates are set to zero for all x-θ values at these radial positions excluding the tube support plates that have FGSP models.

The input and output for THEDA-1 are described in detail in Appendix C.

Section 6

RESULTS

The results consist of two parts--the best estimate analysis and the sensitivity study. In the best estimate analysis, results are presented and compared for the two steam generators. For the sensitivity study, results are presented that show the changes in steam generator conditions due to changes in empirical correlations and grid system. It should be noted that although the predicted exit steam temperatures are consistent with the expected performance, there has been no comparison of local steam conditions to experimental data. Therefore, the results presented in this report must be used with caution.

6.1 BEST ESTIMATE ANALYSIS

The best estimate computer runs were made with the OTSG model and grid system described in Section 5. The runs were made with the three-dimensional model at the operating conditions given in Table 2.1 for the 15%, 67%, and 100% power levels. The empirical correlations used in the analysis are given in Section 3.3. In particular, the Smith void fraction correlation was used with $K_s = 0$, and the B&W proprietary correlation was used for the nucleate boiling heat transfer coefficient.

Each run was initialized with an approximate one-dimensional solution. In this solution, a film dryout height is estimated with a simple model that uses a known constant overall heat transfer coefficient in the nucleate boiling region. Linear interpolation of enthalpy on the primary and secondary sides is then used between the lower tubesheet and film dryout position, and the film dryout position and upper tubesheet. With this enthalpy, an approximate one-dimensional pressure profile is obtained by solving the axial momentum equation with a constant axial mass velocity at each elevation.

As the runs were made, intermediate results were examined at intervals of 30 iterations (one restart). Variables such as axial velocity, pressure, and steam quality were compared with values from the previous restart to check for convergence. In particular, overall parameters such as steam temperature, bleed flow rate, film dryout height in the bundle, and dryout height in the untubed lanes were checked

after each restart to determine if these parameters were still changing. In addition, the convergence parameters described in Section 4.4 were monitored at each iteration. The average continuity and axial momentum equation residuals are given in Table 6.1 for the last iteration. The residuals tended to level out, so that the rate of decrease of the residuals and heat balances diminished as the number of iterations increased. When this occurred, the overall parameters tended to change very slowly from one restart to the next. It was at this point that the runs were terminated. The total number of iterations to reach this point varied for each power level. The 67% runs required the fewest iterations with 150 and 120 for the TMI-2 and DB-2 runs, respectively. The largest discrepancy in heat balance was 2.2% for the 100% DB-2 run after 330 iterations. All other runs had heat balances that were less, as shown in Table 6.1.

TABLE 6.1

BEST ESTIMATE ANALYSIS CONVERGENCE PARAMETERS

	THREE MILE ISLAND UNIT 2			DAVIS-BESSE UNIT 2		
	15%	67%	100%	15%	67%	100%
Total number of iterations	220	150	300	250	120	330
Average continuity residual, 10^{-4}	0.53	0.12	0.02	0.28	0.17	0.03
Average axial momentum residual, 10^{-4}	1.4	0.25	0.04	1.2	0.43	3.3
Heat Balance, %	0.37	0.22	0.70	-0.51	-0.13	2.2

The best estimate analysis results which include conditions on the primary and secondary side are given in Table 6.2. The following points are noted.

- The computed heat transfer rates are in good agreement with the nominal heat transfer rates at 67% and 100%. At 15%, the computed heat transfer rates are greater than the nominal values. This discrepancy does not represent an error in the computed results but is caused by inaccurate nominal steam flow rates as read from graphs in the functional specification reports.

- The steam temperature increases from the 67% to 100% power level for DB-2 whereas for TMI-2, the steam temperature decreases at 100%, probably because of the larger bypass flows in the untubed periphery.

- At 67% and 100%, the bleed flow rates for DB-2 are less than those for TMI-2, and about equal at 15%.

- The film dryout height in the DB-2 tube bundle is greater than in the TMI-2 tube bundle at 67% and 100% heat transfer rate. They are nearly equal at 15%. The increased dryout height partly results from DB-2's lower primary flow and higher steam flow rate.

TABLE 6.2

BEST ESTIMATE ANALYSIS RESULTS
(Operating Conditions are listed in Table 2.1)

THREE MILE ISLAND UNIT 2 Design heat transfer rate at 100% power = 1393.5 MWt/OTSG			
Nominal heat transfer rates, % Computed heat transfer rates*, %	15% 16.7	67% 67.6	100% 99.7
Secondary Side			
Outlet steam temperature,°F	585.5	595.0	593.2
Secondary pressure drop, psi	1.08	6.44	12.2
Bleed flow rate, 10^6 lbm/hr	0.309	0.756	0.946
Film dryout height (θ = 180°, r = 2.49 ft), ft	3.78	14.8	25.1
Primary Side			
Outlet temperature, °F	577.4	564.4	556.9
Average temperature, °F	581.7	581.7	582.2
Average ΔT, °F	8.6	34.6	50.6
DAVIS-BESSE UNIT 2 Design heat transfer rate at 100% power = 1394 MWt/OTSG			
Nominal heat transfer rates, % Computed heat transfer rates*, %	15% 18.2	67% 67.6	100% 100.2
Secondary Side			
Outlet steam temperature, °F	585.6	596.9	598.4
Secondary pressure drop, psi	1.24	7.93	15.3
Bleed flow rate, 10^6 lbm/hr	0.325	0.667	0.803
Film dryout height (θ = 180°, r = 2.49 ft), ft	3.75	15.9	27.0
Primary Side			
Outlet temperature, °F	576.1	563.6	555.6
Average temperature, °F	581.0	581.8	582.1
Average ΔT, °F	9.9	36.4	53.0

*Average of primary and secondary side heat transfer rates which differ by the heat balances given in Table 6.1.

Quality contours for TMI-2 and DB-2 are given in Figures 6.1 through 6.8. In Figures 6.1 through 6.6, the lines of constant quality are given in increments of 4% quality. At the inlet port, the quality is 0% (saturated liquid). At each power level, the contours are given at the θ = 0° plane, which slices through the open lane for TMI-2

and the manway lane for DB-2, and at $\theta = 180°$, which is representative of conditions in the tube bundle. It is also noted that the radial dimension is expanded three times the axial dimension in each figure.

In Figures 6.7 and 6.8, r - θ quality contours are presented at the 49-foot elevation for each steam generator. For TMI-2, this elevation is 0.6 foot above the 15th tube support plate and in DB-2, this is 0.5 foot below the 16th tube support plate.

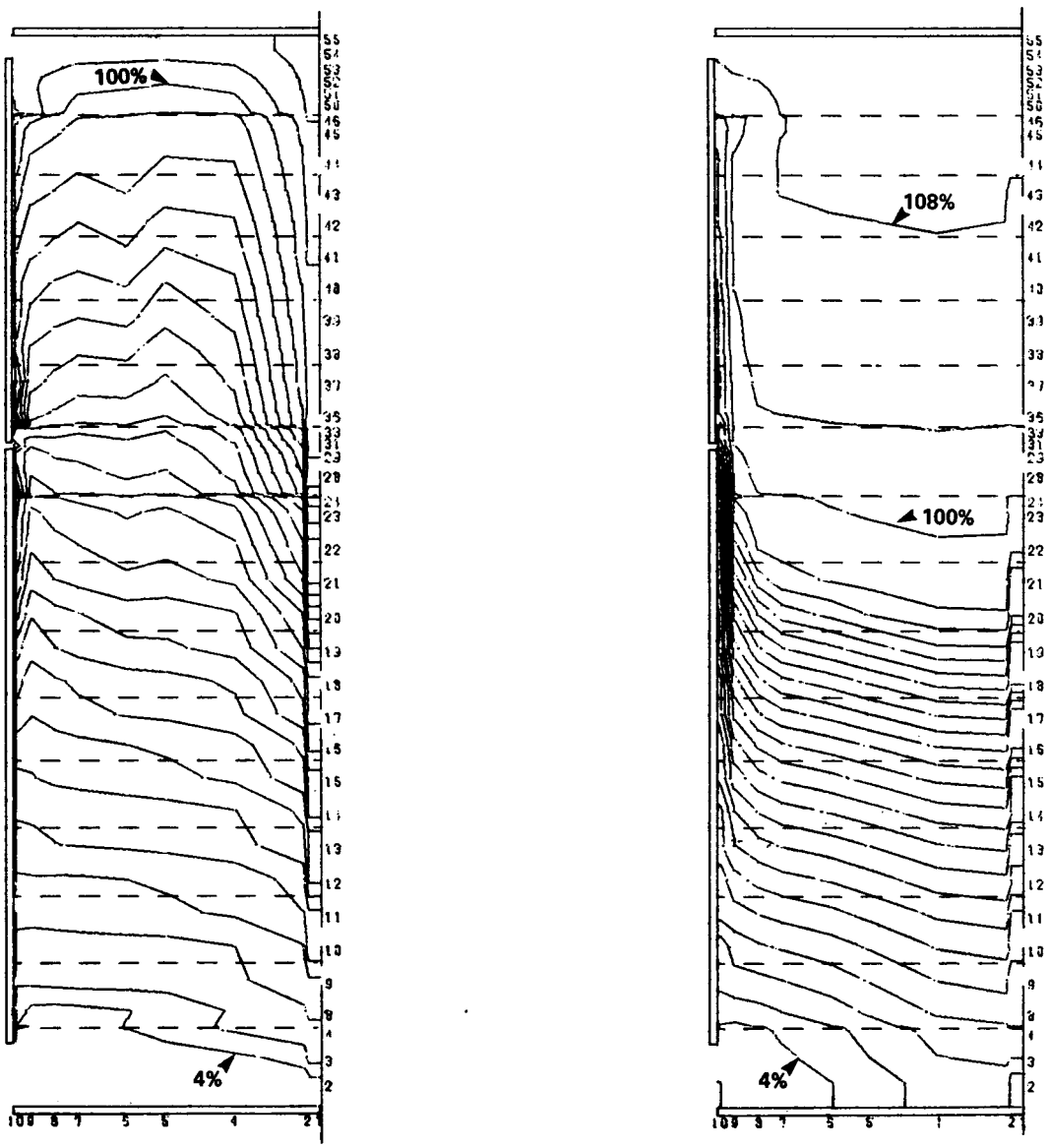

OPEN LANE, $\theta = 0^{o}$ TUBE BUNDLE, $\theta = 180^{o}$

FIGURE 6.1 TMI-2 100% POWER QUALITY CONTOURS (4% QUALITY INCREMENTS)

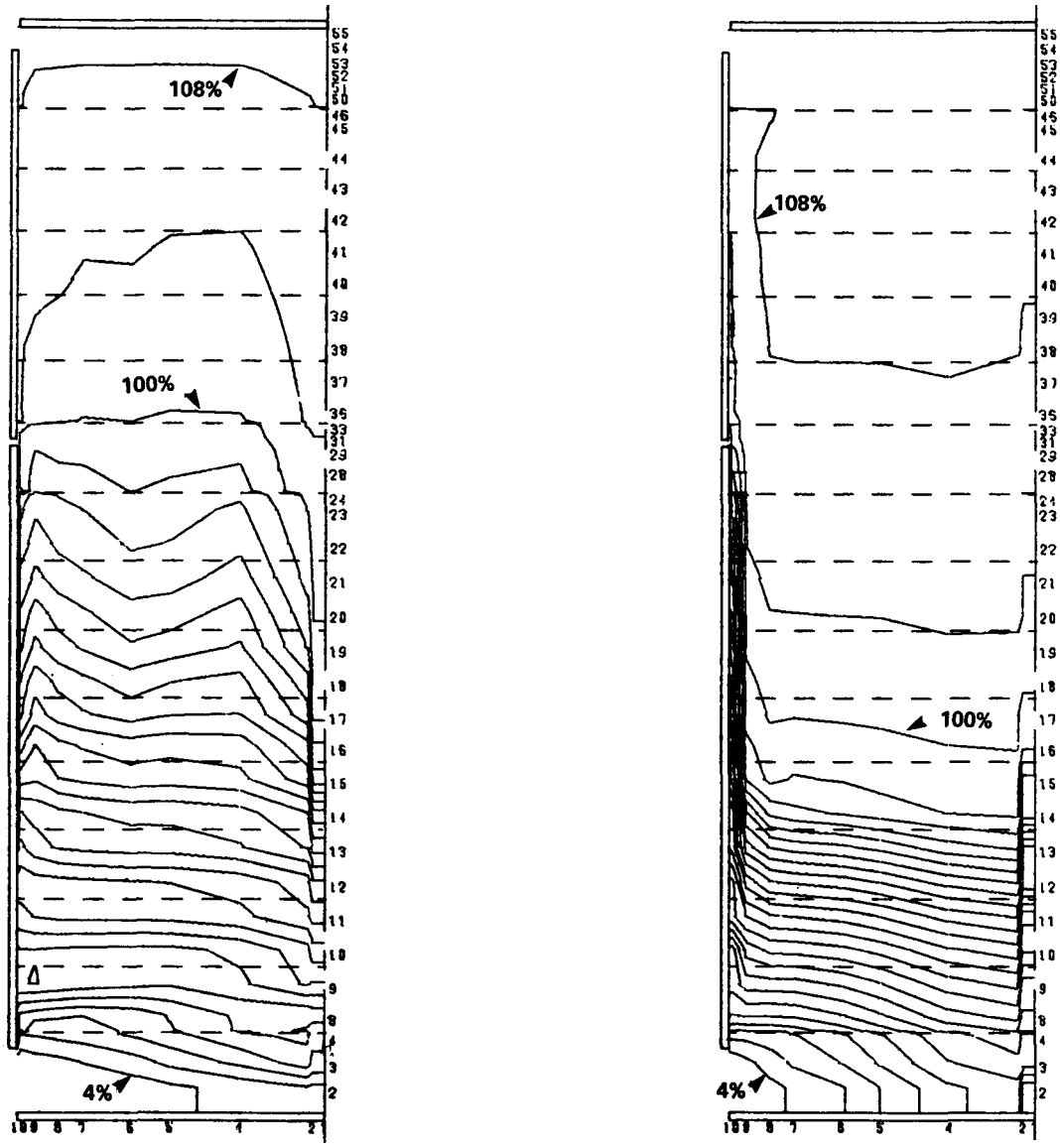

OPEN LANE , θ = 0°

TUBE BUNDLE θ = 180°

FIGURE 6.2 TMI-2 67% POWER QUALITY CONTOURS
(4% QUALITY INCREMENTS)

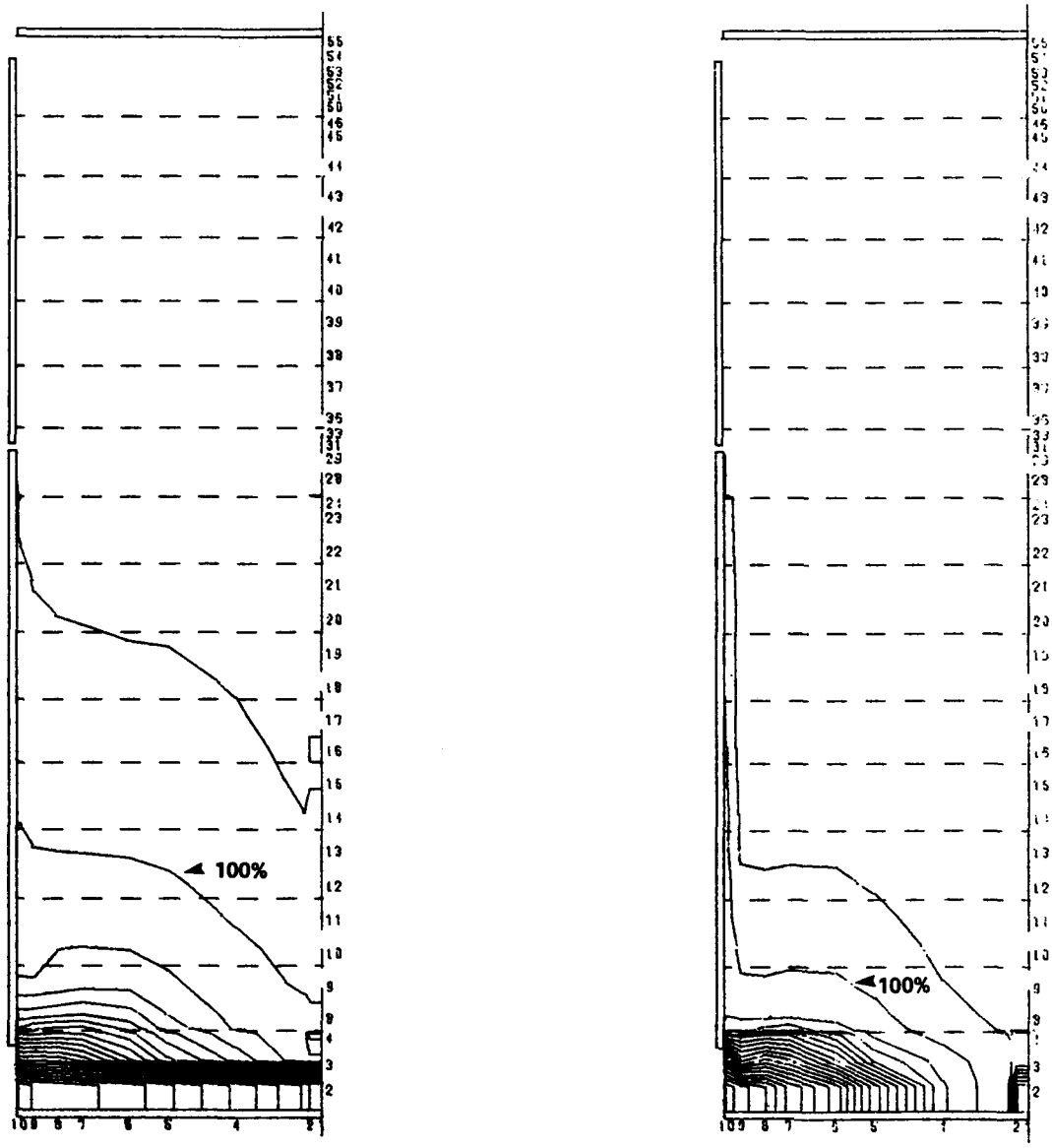

OPEN LANE, θ = 0°

TUBE BUNDLE, θ = 180°

FIGURE 6.3 TMI-2 15% POWER QUALITY CONTOURS
(4% QUALITY INCREMENTS)

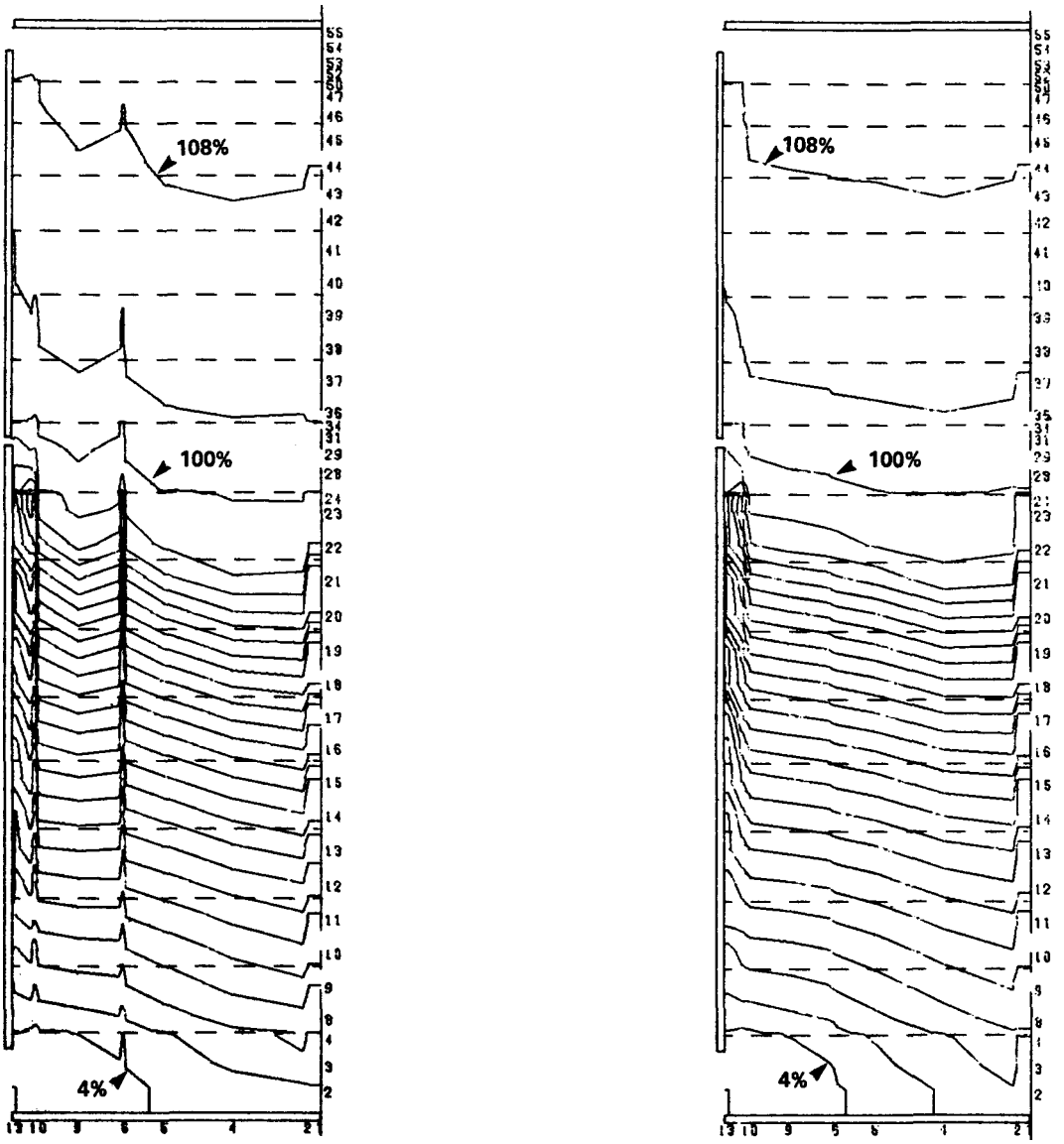

MANWAY LANE, θ = 0°

TUBE BUNDLE, θ = 180°

FIGURE 6.4 DB-2 100% POWER QUALITY CONTOURS
(4% QUALITY INCREMENTS)

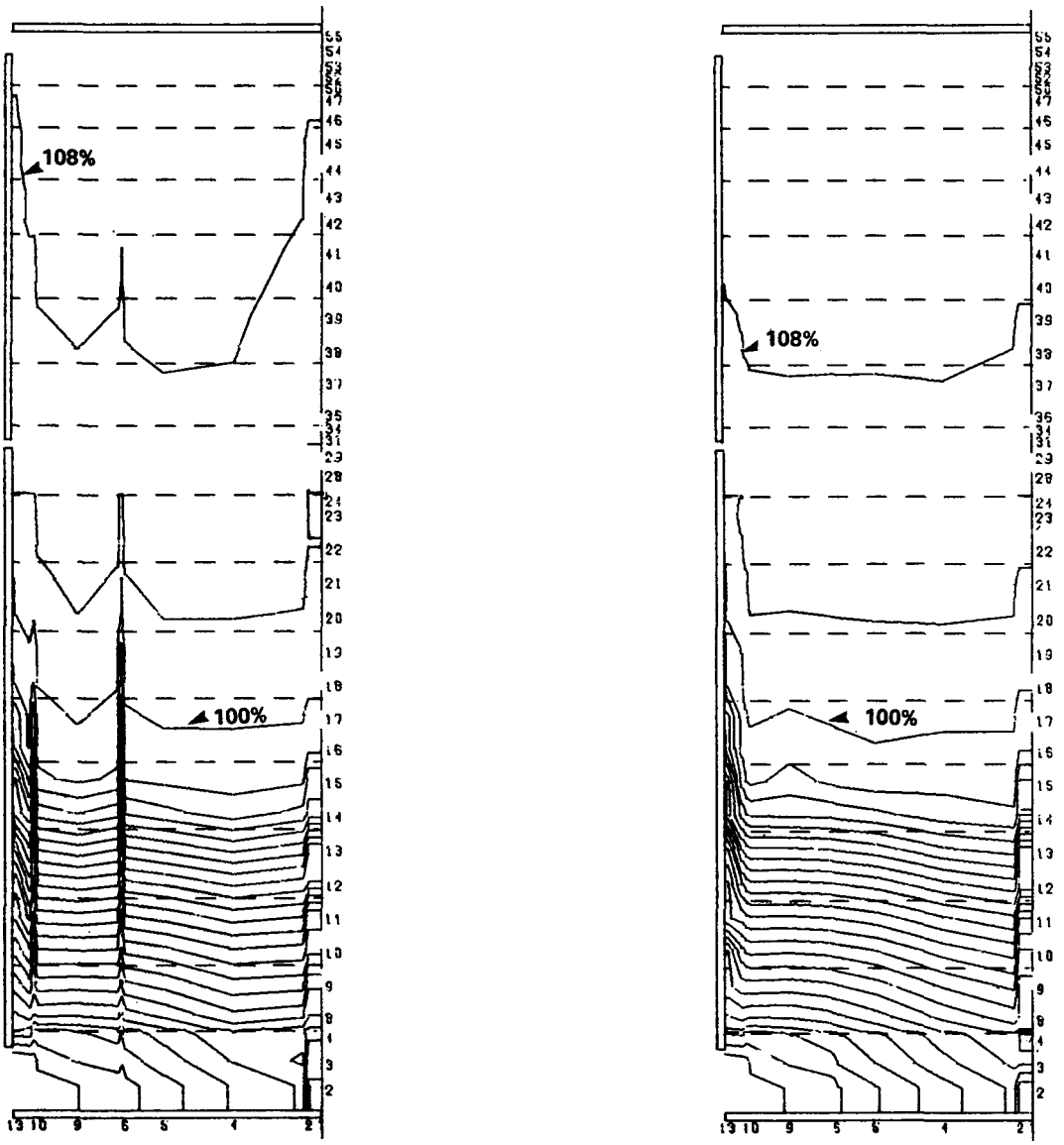

MANWAY LANE, θ = 0°

TUBE BUNDLE, θ = 180°

FIGURE 6.5 DB-2 67% POWER QUALITY CONTOURS
(4% QUALITY INCREMENTS)

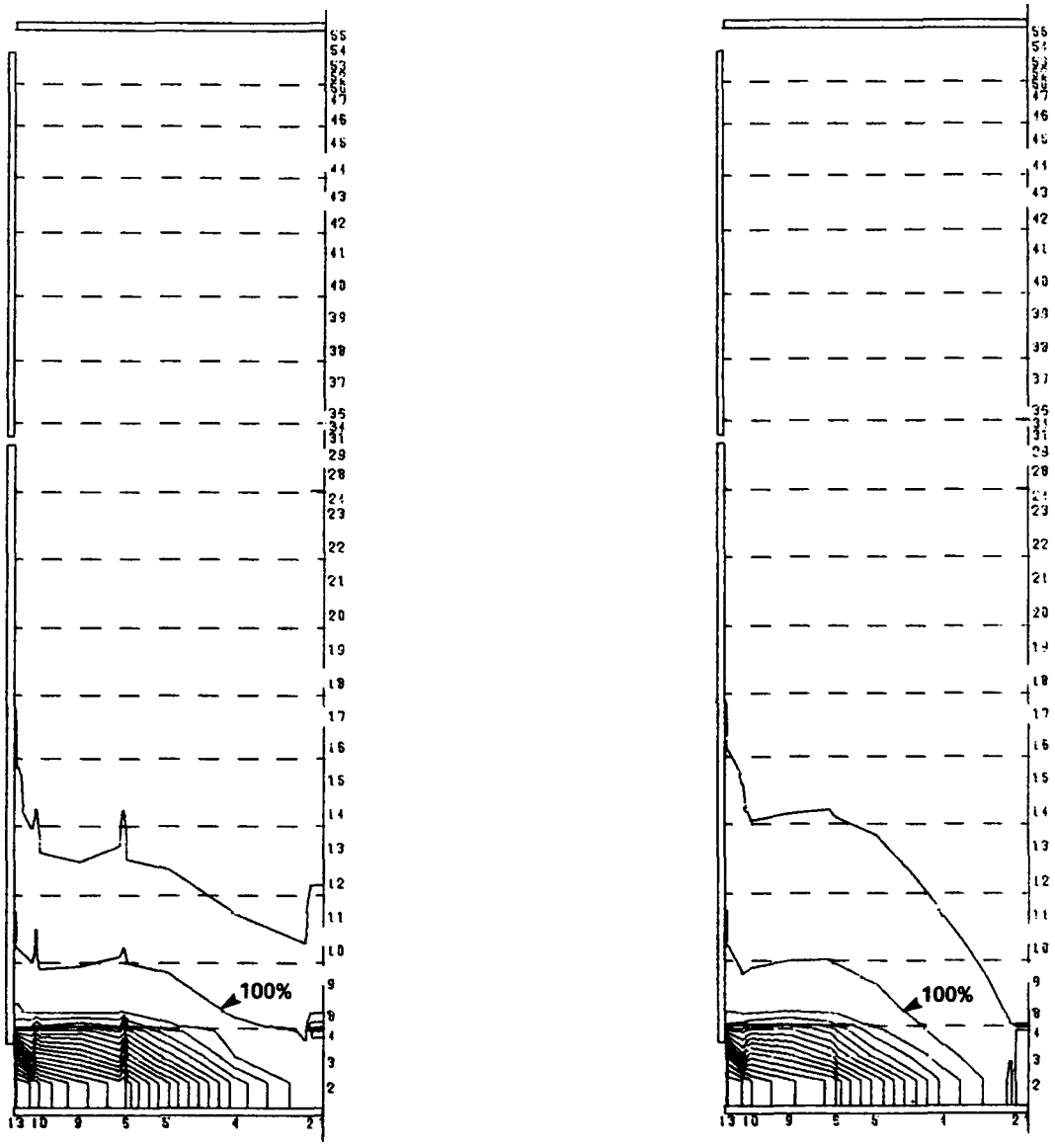

MANWAY LANE, θ = 0°

TUBE BUNDLE, θ = 180°

FIGURE 6.6 DB-2 15% POWER QUALITY CONTOURS
(4% QUALITY INCREMENTS)

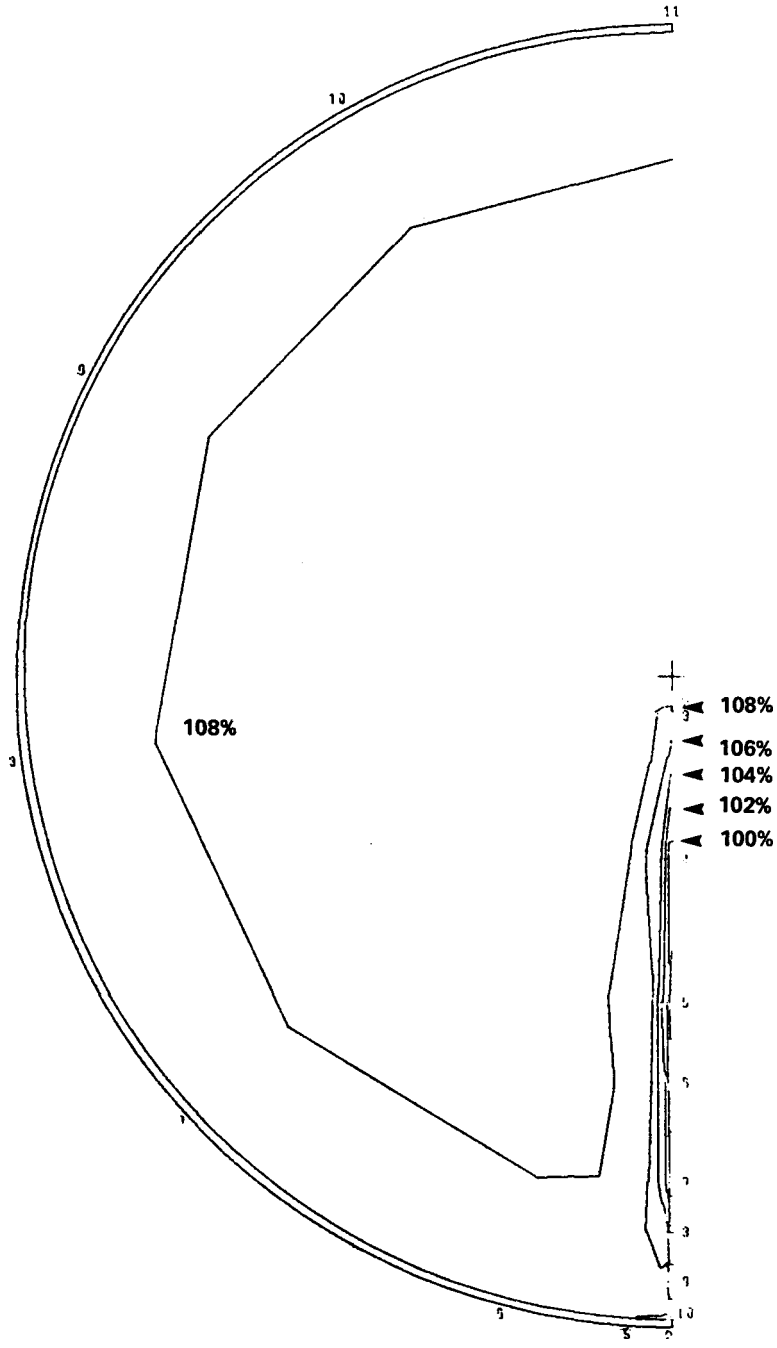

FIGURE 6.7 TMI-2 100% POWER QUALITY CONTOUR,
X = 49 FT
(2% QUALITY INCREMENTS)

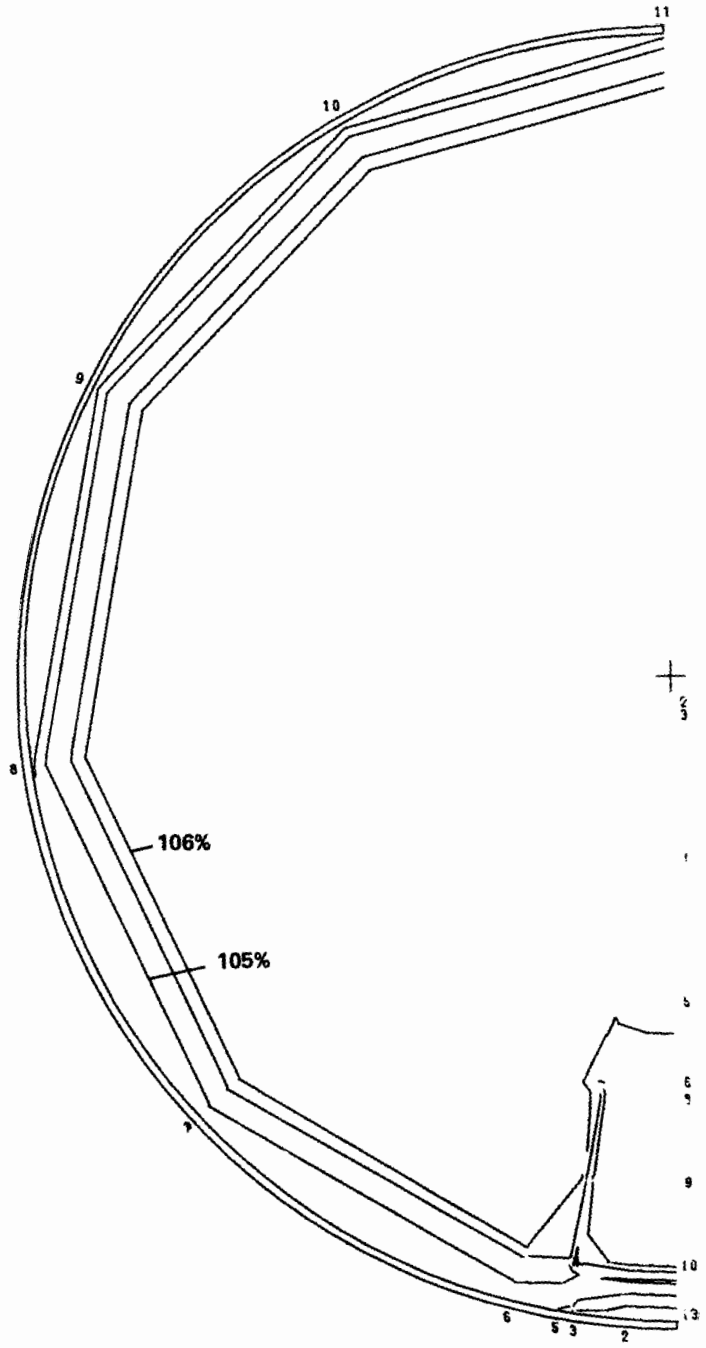

FIGURE 6.8 DB-2 100% POWER QUALITY CONTOUR, X = 49 FT (0.5% QUALITY INCREMENTS)

The following are noted from the quality contours:

- At all power levels for TMI-2 and at a given elevation, the steam quality in the open lane is much less than the quality in the tube bundle away from the open lane. The maximum difference occurs at the tube bundle film dryout height. The maximum difference also increases with load. At 15% power and at mid-radius, it is approximately 10%; at 67% power, it is 35%; and at 100% power, it is 50%. Above the film dryout height, the differences in lane and bundle qualities decrease with increasing elevation.
- At the 100% power levels for TMI-2, the steam in the open lane does not reach superheat until after the 15th tube support plate.
- Steam qualities in the DB-2 manway lane are, in most cases, less than 8% below the steam qualities in the tube bundle at any given elevation. In the superheat region, this difference does not exceed 2%.
- The steam quality in the TMI-2 unblocked peripheral gap is significantly lower than the quality in the blocked DB-2 peripheral gap. The line of 100% quality reaches the 15th tube support plate in the TMI-2 peripheral gap but in DB-2, the gap quality is 100% at the 10th tube support plate.
- Steam quality contours in the center untubed regions are very similar for both steam generators. At 100% power, the difference in quality between the center untubed region and the adjacent tube bundle reaches a maximum of 12% in the nucleate boiling region. In the superheat region, this difference is less than 1% quality.

Further details of the best estimate analysis results are presented in Figures 6.9 through 6.13. In these figures, local conditions are presented at $\theta = 180°$. As shown in Figures 6.7 and 6.8, the conditions at $\theta = 180°$ are representative of conditions for a large majority of x - r planes in the two steam generators away from the untubed lanes.

In Figure 6.9, quality versus axial height is shown in the tube bundle and peripheral gap. The quality profile in the tube bundle shows a steady increase in quality until film dryout is reached (95% quality). After film dryout, the increase is more gradual due to less heat transfer in the film boiling and superheated steam regions compared to the nucleate boiling region. In the peripheral gap below the bleed port, steam quality increases at a lower rate than in the tube bundle. At the bleed port,

the lower quality peripheral gap steam is drawn off to heat the feedwater and higher quality steam from the tube bundle flows outward and mixes with the peripheral gap steam. This results in a sharp increase in peripheral gap quality. This increase is greater in TMI-2 since the peripheral gap qualities differ from the tube bundle qualities to a greater extent than in DB-2 which has the blocked peripheral gap at the tube support plates.

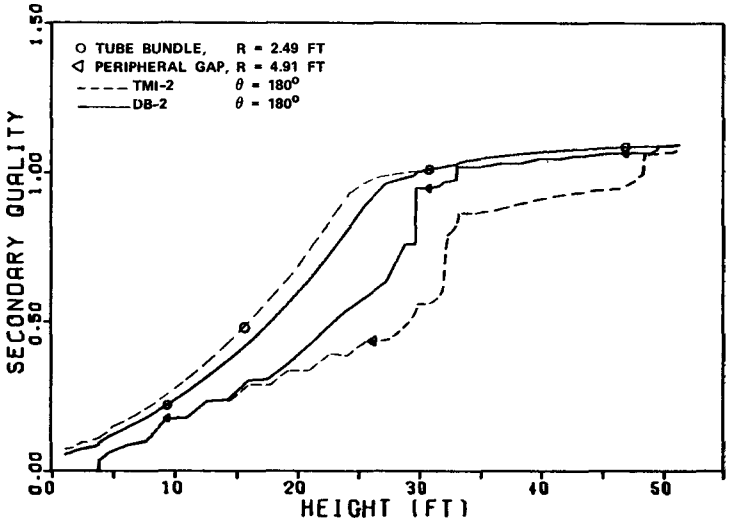

FIGURE 6.9 COMPARISON OF QUALITY PROFILES FOR TMI-2 AND DB-2 AT 100% POWER

Temperature profiles for each power level are given in Figures 6.10, 6.11, and 6.12. Primary and secondary side temperature profiles in the tube bundle are similar for the two steam generators. In the DB-2 peripheral gap, the steam temperatures in the superheat regions are considerably higher than the gap temperatures in TMI-2.

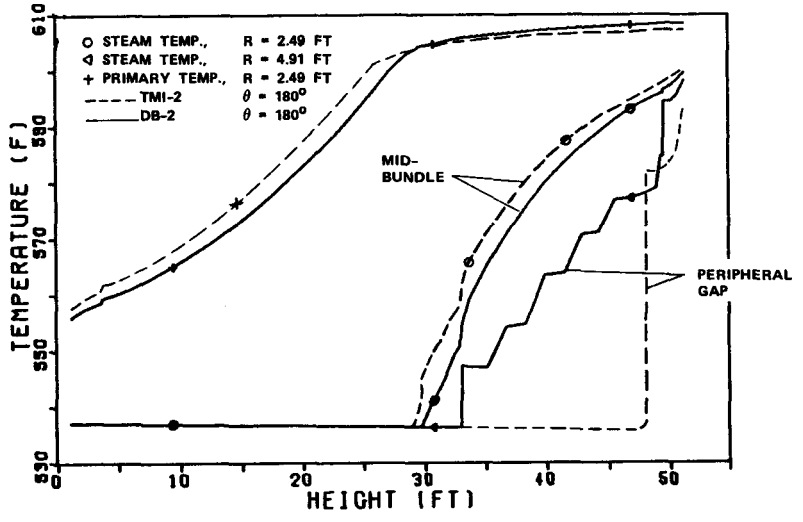

FIGURE 6.10 COMPARISON OF AXIAL TEMPERATURE DISTRIBUTIONS FOR TMI-2 AND DB-2 AT 100% POWER

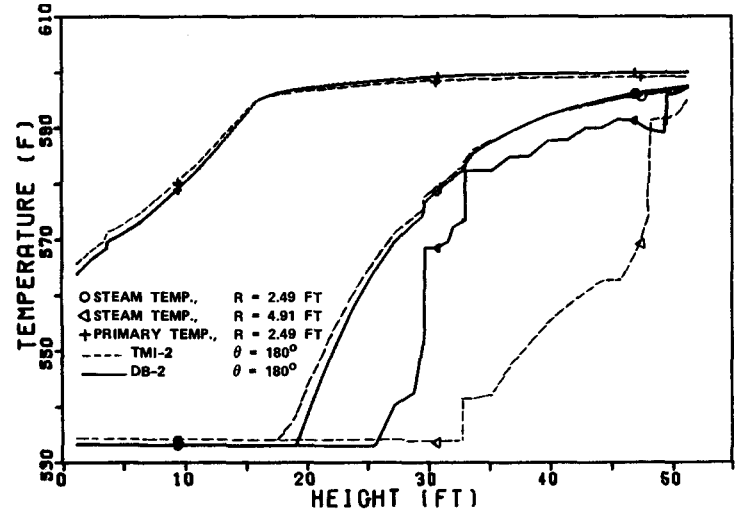

FIGURE 6.11 COMPARISON OF AXIAL TEMPERATURE DISTRIBUTIONS FOR TMI-2 AND DB-2 AT 67% POWER

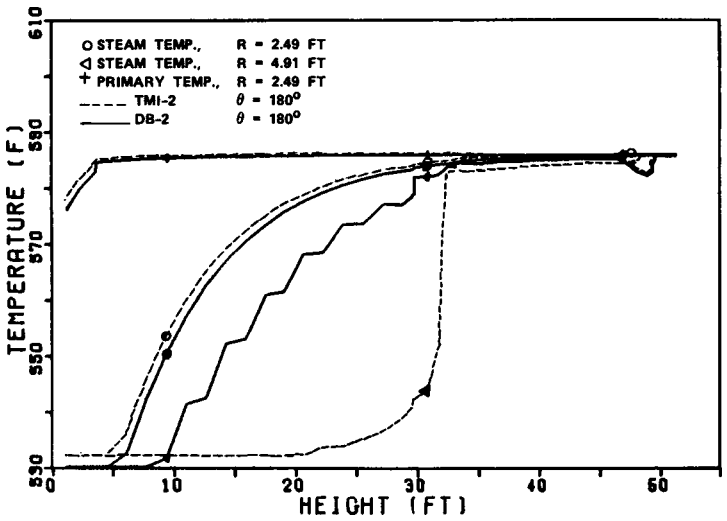

FIGURE 6.12 COMPARISON OF AXIAL TEMPERATURE DISTRIBUTIONS FOR TMI-2 AND DB-2 AT 15% POWER

In Figure 6.13, the differences in axial velocity due to the differences in top tube support plate geometries are shown. At the 49-foot elevation (6 inches below the DB-2 16th tube support plate), the velocities are lower at those radii that correspond to the preferentially broached region in the 16th tube support plate. At the 49-foot elevation (9 inches above the TMI-2 15th tube support plate), the velocity profile reaches a peak at a radius of 4.3 feet. This peak is caused by the flow bypassing the blocked gap. At all other elevations, the velocities in the tube bundle are nearly equal for the two steam generators.

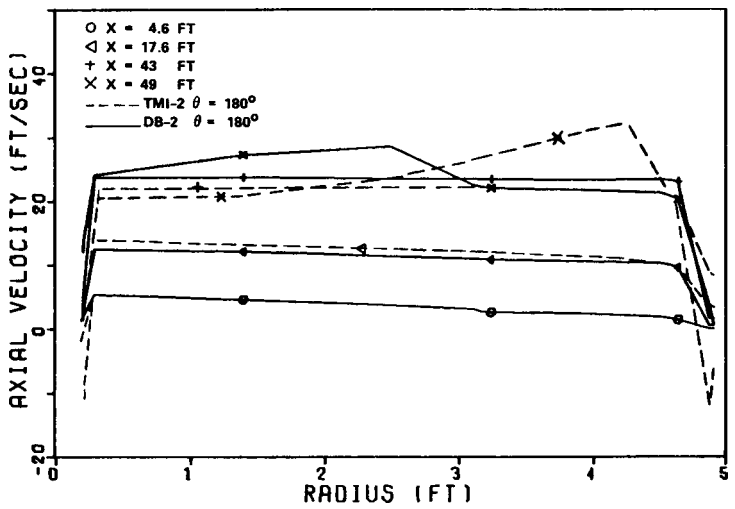

FIGURE 6.13 COMPARISON OF AXIAL VELOCITY DISTRIBUTIONS FOR TMI-2 AND DB-2 AT 100% POWER

6.2 SENSITIVITY STUDY

In the sensitivity study, changes in empirical correlations, grid spacing, and the level of tube support plate detail were made to determine the effect on predicted steam generator performance as well as the local conditions within the steam generator. The sensitivity study results are presented in two parts. The first part contains results from a two-dimensional (2-D) sensitivity study that neglects the open lane. For this sensitivity study, a two-dimensional model is used that represents most features in the TMI-2 steam generator excluding the open lane. The second part contains results from a 2-D circumferential open lane (COL) sensitivity study which approximates the TMI-2 radial open lane with a circumferential open lane of the same width. The 2-D COL model was used rather than a 3-D model because of the much greater cost of running a 3-D model and because a 3-D model severely limits the number of axial and radial nodes available for modeling the steam generator. As shown later, the 2-D and 3-D model results agree well when lane conditions are compared at mid-radius.

6.2.1 Procedure

The following approach was used to perform the sensitivity study. First, nominal runs using TMI-2 100% power operating conditions were made for both the 2-D sensitivity study and the COL sensitivity study. These runs contained the correlations described in Section 3.3 that were used for the best estimate analysis. In particular, the Smith void fraction correlation and the B&W proprietary nucleate boiling correlation were used. Changes were then made to the nominal runs.

Changes in empirical correlations were accomplished by applying multipliers to the nominal correlations in most cases. For each correlation, two changes were made. Usually, the first change employed a multiplier less than one and the second used a multiplier greater than one. For the void fraction correlation changes, and one change for the nucleate boiling coefficient, the nominal correlations were replaced by other correlations rather than using multipliers. The magnitudes of the multipliers were different for each correlation. These values were chosen so as to represent a conservative range of uncertainty for each correlation.

Other runs were made to estimate the uncertainty in the results due to the coarseness of the grid system. In these cases, runs were made with nodes added or removed from the nominal case so that results could be compared with the nominal run. In another case, fine grid tube support plate (FGSP) models were added to all the

support plates for comparison with the nominal run which contained only four FGSP models. Unlike the cases where the grid system was changed, this case changes the actual physical model with more modeling detail at all the tube support plates.

For both the 2-D sensitivity study and COL sensitivity study, two-dimensional models were used. With the two-dimensional models, conditions were determined in the x-r plane with no variation in the circumferential direction. This allowed many more parameters to be studied than could have been obtained with a three-dimensional model due to computer cost and storage considerations. For the 2-D sensitivity study, the two-dimensional model used the axial grid shown in Table A.3 and the radial grid shown in Table A.6. For the COL study, the same axial grid was used. The radial grid, however, was set up to model a circumferential open lane. The COL was positioned at mid-radius (r = 2.466 ft) with two radial nodes placed within the lane along with one node placed on either side of the lane. The main node points are given in Table A.8. The width of the COL was set equal to the width of the TMI-2 open lane. Thus, the total cross-sectional area of the COL in a plane perpendicular to the x direction is π times the cross-sectional area of the TMI-2 lane. Therefore, the COL model is conservative in that it predicts a somewhat lower exit steam temperature because the COL lane has π times more unheated area than the 3-D radial lane it approximates.

6.2.2 Two-Dimensional Sensitivity Study Results

As mentioned previously, the 2-D sensitivity study was done to obtain the sensitivity of overall and local conditions to changes in empirical correlations and grid system for those regions of the steam generator that are away from the open lane. To change the correlations, multipliers were applied to the nominal correlation or entire correlations were changed. For changes in grid system, nodes were both added and deleted from the nominal case as shown in Tables A.3 through A.8.

After several runs were made, it was discovered that the porosities for the main nodes at the bottom faces of the four fine grid tube support plates were set to the bundle porosities rather than the tube support plate porosities. These porositities were corrected and a new nominal run was made. Except for the pressure drop, the results were not significantly changed. The 11 regular support plates were not affected by this error.

The parameters that were studied along with the changes that were made are given below:

1) Void Fraction *

Nominal : Smith correlation (K_s = 0)

Changes : homogeneous model, Thom correlation

2) Turbulent Mixing (Diffusion) Coefficient *

Nominal : Γ_t and μ_t defined by Eq. 3.58 and Eq. 3.60

Changes : Γ_t and μ_t times 0.2, 5.0, 15.0, and 50.0

3) Tube Support Plate Resistance *

Nominal : R_{tsp} defined by Eq. 3.66

Changes : all K factors (both K_{RSP} and K_{FGSP}) times 0.75 and 1.25 (±25%)

4) Cross-Flow Resistance *

Nominal : R_r and R_θ defined by Eq. 3.68 with f' by Jakob

Changes : f' times 0.5 and 3.0

5) Nucleate Boiling Coefficient *

Nominal : B&W proprietary correlation

Changes : B&W proprietary times 0.5 and the Chen correlation

6) Superheated Steam Coefficient *

Nominal : Kay's correlation

Changes : Kay's correlation times 0.9 and 1.10 (±10%)

---

*f (as defined in Eq. 5.1) is 1.0 as discussed in Section 5.2 and the Fine Grid Support Plate porosity is in error as discussed in Section 6.2.2.

7) Film Dryout Quality *

Nominal : $x_{DO} = 0.95$

Changes : $x_{DO} = 0.92$ and 0.98 ($\pm 3\%$)

8) Number of Axial Nodes *

Nominal : 54 axial nodes

Changes : 41 and 115 axial nodes

9) Number of Radial Nodes **

Nominal : 15 radial nodes

Changes : 11 and 21 radial nodes

10) Peripheral Gap Tube Support Plate Resistance **

Nominal : $K_{RSP} = 25.3$ in the gap

Changes : $K_{RSP} = 12.7$ and 38.0 ($\pm 50\%$)

11) Fine Grid Support Plate Model **

Nominal : contained FGSP models at TSPs 1, 9, 10, and 15

Changes : 99 axial nodes with all TSPs with FGSP models

A total of 21 cases were examined and are compared to the nominal run.

The changes were chosen so as to represent a conservative range of uncertainty. The basis for selecting the values was previous experience in modeling operating and laboratory OTSGs with one-dimensional computer codes. In the case of cross-flow resistance, there is no OTSG data and it was assumed that Jakob's single-phase f' factor and Thom's two-phase friction multiplier ϕ_{fo}^2 could be used in

*f (as defined in Eq. 5.1) is 1.0 as discussed in Section 5.2 and the Fine Grid Support Plate porosity is in error as discussed in Section 6.2.2.

**f = 1.0, FGSP porosities corrected.

Eq. 3.68. Therefore, a large range of uncertainty (0.5 and 3.0 times f') was applied. Similarly, in the case of the mixing coefficient, a wide range of Γ_ϕ's was run, since the correlation was based on LWR rod bundle data at single-phase conditions rather than two-phase conditions.

For the case of the number of axial nodes, 41 axial nodes correspond to 1 axial node between tube support plates, and 115 axial nodes correspond to 6 axial nodes between support plates. For the nominal run (54 axial nodes), two axial nodes were used between the support plates. For the case where 11 radial nodes were used, 4 nodes were removed from the tube bundle. For the 21 radial node case, extra nodes were added in the peripheral gap and center untubed region as well as in the tube bundle. The main node locations are given in Appendix A.

Results were obtained for the nominal run and change cases described above. The nominal run was brought to convergence in 360 iterations. The final values of the average residuals are given in Table 6.3.

TABLE 6.3

NOMINAL RUN RESIDUALS

Average Continuity Residual	3.3×10^{-6}
Average Axial Momentum Residual	3.2×10^{-6}
Heat Balance, %	0.095

The changes involving empirical correlations were initialized with the nominal run and, in general, required fewer total iterations to reach convergence than the nominal run which was started from initial values based on a one-dimensional calculation as described in Section 6.1. The residuals for the change cases were of the same order of magnitude as those given in Table 6.3. By comparing the nominal run residuals with those given in Table 6.1, it can be seen that the sensitivity study runs were brought to a higher level of convergence than in the best estimate analysis. This was necessary since many of the change cases involved only small perturbations in local conditions.

The results for the overall conditions are presented in Table 6.4. Here, the nominal conditions are given along with the perturbations for each case that was studied. The perturbations are defined as the change case value minus the nominal value. Included are perturbations in steam temperature (T_S), total pressure drop (ΔP), bleed flow ($\dot{m}_B$), and dryout height at r = 2.49 ft.

TABLE 6.4

NOMINAL RESULTS AND PERTURBATIONS*

	T_S (F)	ΔP (psi)	$\dot{m}_B$ (10^6 lbm/hr)	Dryout Height (ft)
Nominal (-30 iterations)**	593.3	10.4	0.9316	25.403
Nominal (last iteration)	593.4	10.4	0.9314	25.376
Difference	-0.1	0.0	0.0002	0.027
Thom Void Fraction	-1.0	-1.0	0.126	-0.115
Homogeneous Void Fraction	-1.9	-1.4	0.187	-0.332
Turbulent Mixing x 0.2	-0.3	0.0	0.007	-0.023
Turbulent Mixing x 5.0	0.4	0.0	-0.037	-0.023
Turbulent Mixing x 15.0	1.3	0.1	-0.090	-0.159
Turbulent Mixing x 50.0	2.3	0.4	-0.156	0.027
Tube Support Plate K x 0.75	0.2	-1.0	-0.022	0.085
Tube Support Plate K x 1.25	-0.2	1.0	0.019	-0.127
Cross-Flow Resistance Coeff. x 0.5	0.3	-0.6	-0.034	-0.023
Cross-Flow Resistance Coeff. x 3.0	-0.5	1.9	0.081	-0.166
Chen Nucleate Boiling Coeff.	-15.6	0.2	0.313	8.573
B&W Proprietary Coeff. x 0.5	-1.8	0.1	0.039	1.846
Steam Convection Coeff. x 0.9	-2.0	0.0	-0.0011	-0.103
Steam Convection Coeff. x 1.1	2.7	0.1	-0.0007	0.054
x_{DO} = 0.92	-1.5	0.0	0.002	-0.506
x_{DO} = 0.98	1.4	0.1	-0.004	0.301
41 Axial Nodes	-1.2	0.0	0.014	0.682
115 Axial Nodes	0.6	0.3	-0.033	-0.319
Corrected Nominal (-30 iterations)***	592.7	12.1	0.9595	25.466
Corrected Nominal (last iteration)	592.6	12.1	0.9590	25.455
Difference	0.1	0.0	0.0005	0.011
Gap K x 0.5	-0.8	-0.1	0.056	-0.252
Gap K x 1.5	0.9	0.1	-0.026	0.117
11 Radial Nodes	0.3	0.0	-0.011	0.011
21 Radial Nodes	0.5	0.1	0.023	0.181
All FGSP Models	2.6	2.0	-0.012	-0.139

*The perturbation is defined as the change case minus the nominal case.

**Tube support plate porosity error.

***Corrected tube support plate porosity.

For the two nominal runs, the results before the last restart are given along with the final results. The differences in these values can be used as an estimate of the uncertainty in the nominal values due to convergence. Those perturbations that are of the same magnitude as these differences can be considered negligible perturbations.

The following are noted from Table 6.4:

- In general, the magnitudes of the perturbations in overall steam generator conditions are not particularly large compared to the nominal values. Only the use of the Chen correlation resulted in large changes in overall conditions. In particular, 15.6°F less superheat was predicted than the nominal run.
- The parameters that had a moderate influence on steam temperature (thermal performance) included : void fraction, turbulent mixing (x 15 and x 50 cases), nucleate boiling coefficient, steam convection coefficient, film dryout quality, 41 axial nodes, and the FGSP model.
- The parameters that had a moderate influence on pressure drop (hydraulic performance) included : void fraction correlation, tube support plate resistance coefficient, cross-flow pressure drop coefficient, and the FGSP model.
- Since changes in bleed flow rate are due to changes in the peripheral gap bleed port quality, it can be inferred that those parameters that have a moderate influence on bleed flow rate also have an influence on local conditions within the steam generator. They include: void fraction correlation, turbulent mixing coefficient (x 15 and x 50 cases), and cross-flow resistance coefficient and peripheral gap K factor to a lesser extent.
- The film dryout height gives an indication of conditions in the tube bundle. Those parameters that have a moderate influence on film dryout include : void fraction correlation, nucleate boiling correlation, film dryout quality, and the number of axial nodes.

- In all cases where the perturbations were significant, the plus or minus sign of the perturbations was physically consistent for the changes that were made in the correlations. For example, an increase in the superheat heat transfer coefficient resulted in an increased steam temperature.
- By comparing the original nominal and corrected nominal runs, it can be seen that the FGSP porosity correction primarily affected the pressure drop as expected. The steam temperature was slightly decreased, but the bleed flow rate and DNB height were relatively unaffected.

To obtain an overall picture of how conditions changed within the steam generator, the reader is referred to Appendix B. The quality contours given for each case show the changes in local thermal conditions.

The following are noted from the quality contours:

- In most cases, the local steam quality in the tube bundle is not significantly changed. The exceptions are cross-flow resistance coefficient, nucleate boiling coefficient, and the FGSP model. For cross-flow resistance coefficient, (Figures B.11 and B.12) the radial distribution of quality was changed. For nucleate boiling, the Chen correlation predicted a much larger boiling region (Figure B.13). With the FGSP model, the tube support plates had an influence on the quality distribution (Figure B.22).
- Several parameters have an influence on the peripheral gap conditions while not significantly affecting the bundle conditions. They include : void fraction (Figures B.3 and B.4), large increases in mixing coefficients (Figures B.7 and B.8), 41 axial nodes (Figure B.19), and the peripheral gap resistance (Figures B.23 and B.24).
- For 115 axial nodes, closed quality contours occur in the center untubed region near the 11th, 13th, and 14th tube support plates (Figure B.20). The solution does not appear fully converged in these regions. In the rest of the steam generator, however, steam quality compares favorably with the nominal run.
- Increasing the number of radial nodes to 21 changes the radial quality profiles near the center untubed region (Figure B.26). Steam quality in the tube bundle is relatively unchanged.

Additional details for the regular sensitivity study results are provided in Figures 6.14 through 6.46. In these figures, axial and radial profiles are shown only if they differ from the nominal profile. On each figure, the nominal profiles are shown with a solid line.

Void Fraction

With the exception of the Chen boiling correlation, the void fraction correlation has the largest effect on bleed steam flow (Table 6.4). As expected, the void fraction correlation also has a significant effect on local steam quality.

In Figure 6.14, the nominal quality profiles versus axial height are shown for radial positions in the tube bundle and peripheral gap. Quality profiles at the same radial positions are shown for both the Thom and homogeneous void fraction models. The use of the Thom and homogeneous models results in very little change in quality in the tube bundle. Only a slight increase in quality is predicted for the homogeneous model, which decreases the film dryout position by the amount shown in Table 6.4. In the peripheral gap, however, there is a significant decrease in quality for both correlations. The differences in gap quality between the nominal and each of the change cases reach a maximum of 12% just below the bleed port. The decreased gap quality was the reason the bleed flow rate increased by the amount shown in Table 6.4.

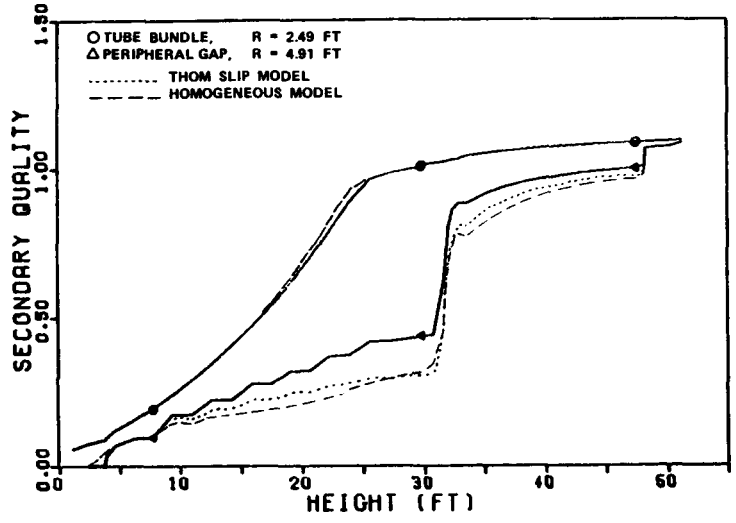

FIGURE 6.14 EFFECT OF CHANGES IN VOID FRACTION CORRELATION ON QUALITY PROFILES

In Figure 6.15, pressure versus axial position is shown for the nominal, Thom, and homogeneous models, respectively. From an examination of the results, it was found that axial profiles between the inlet and outlet ports were essentially the same at all radial positions. The figure shows that lower pressure drops are predicted for the Thom and homogeneous models in the low quality region of the steam generator where two-phase density is most sensitive to changes in void fraction. Both the Thom and homogeneous models have lower slip ratios and thus, higher void fraction at a given quality than the nominal Smith correlation. Therefore, the volume average two-phase density given by Eq. 3.22 and thus, the gravitational pressure drop term for the axial momentum equation control volumes is less for the Thom and homogeneous models as compared to the Smith Correlation.

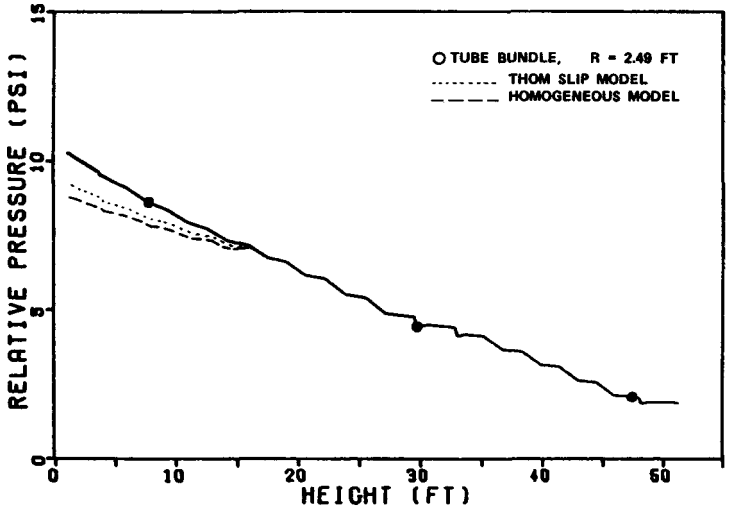

FIGURE 6.15 EFFECT OF CHANGES IN VOID FRACTION CORRELATION ON THE PRESSURE PROFILE

A simple axial momentum balance can be used to qualitatively explain the effect of the void fraction correlation on quality and flow in the peripheral gap. The convection, diffusion, pressure, and gravity terms for a peripheral gap momentum control volume between tube support plates were estimated using THEDA predicted pressures, velocities, and enthalpies. Diffusion due to turbulent mixing and wall shear was found to be negligible and the net convection of axial momentum was found to be small (approximately 10%) compared to the pressure and gravity terms. Radial pressure gradients are small and so the net axial pressure force on a control volume in the peripheral gap is determined by the axial pressure gradient in the tube bundle. This pressure force is balanced mostly by the gravity head which depends on the volume averaged fluid density and hence the void fraction correlation.

Simply, the void fraction in the peripheral gap must be such that the gravity head nearly balances the bundle axial pressure gradient.

The void fraction in the peripheral gap can now be estimated merely by knowing the bundle axial pressure gradient. The quality in the gap is related to the void fraction by Eq. 3.20 which can be rewritten in terms of the velocity ratio, S, as

$$\chi = \frac{\alpha \rho_g}{\alpha \rho_g + (1-\alpha) \rho_f / S} \tag{6.1}$$

For a given void fraction, gap quality increases directly with an increase in S. Thus for the same bundle pressure gradient, an algebraic slip model for void fraction, as used for the nominal run, would be expected to result in higher gap qualities than a homogeneous model. The THEDA-1 predictions shown in Figure 6.14 support this argument. Since the void fraction in the gap is fixed by the axial pressure gradient, the quality in the gap depends on the velocity difference between the liquid and vapor phases as indicated by Eq. 3.20.

Since the peripheral gap is untubed, heating of the gap fluid must take place by convection and diffusion (turbulent mixing) from the tube bundle. The mixing coefficient sensitivity runs indicate that turbulent mixing (for the nominal run) is insignificant in the two-phase region. Therefore, the gap fluid is heated solely by convection from the bundle. To preserve an axial momentum balance, the net energy transferred by radial flow in and out of the peripheral gap must be sufficient to increase the void fraction in the gap so that the gravity head balances the tube bundle axial pressure gradient.

Radial flow in and out of the gap region causes an increase and a decrease in axial velocity to satisfy a mass balance as shown by Figure 6.16. The in and out flow repeats at every tube support plate. Since the homogeneous model results in smaller quality increases than the algebraic slip models, the convective flow in and out of the gap should be less for the homogeneous model than the slip models. This is also substantiated by Figure 6.16 which shows smaller changes in the axial velocity for the homogeneous model.

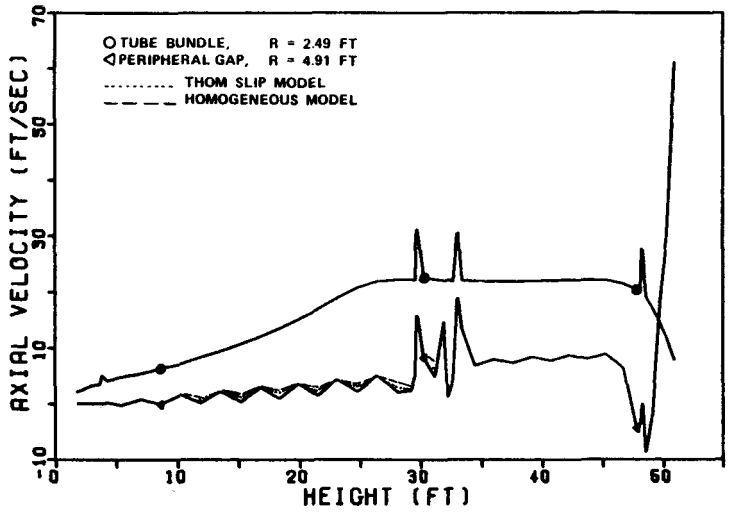

FIGURE 6.16 EFFECT OF CHANGES IN VOID FRACTION CORRELATION ON AXIAL VELOCITY PROFILES

The flow in the peripheral gap at a tube support plate is determined by the pressure drop across the tubed region of the support plate. Above a height of 15 feet, the tube support plate pressure drop is not significantly affected by the void fraction correlation (Figure 6.15) and, therefore, the velocity in the gap at the support plate is unaffected. (This velocity is the peak velocity shown on Figure 6.16.) The difference between the maximum and minimum flow is determined by the amount of radial convection required to heat the gap fluid as previously discussed.

In reality, additional factors have a second-order effect on the axial momentum balance for control volumes in the gap. For example, cross-flow resistance and the tube support plate gap resistance affect terms in the axial momentum equation. However, as discussed in subsequent sections dealing with the sensitivity studies for these resistances, the effect on quality in the gap is small indicating that a balance of the axial pressure gradient and the fluid density in the gap is the dominant factor in determining gap quality over a wide range of other variables.

The effect of changes in void fraction on radial temperature distributions is shown in Figure 6.17. When the void fraction is determined from the homogenous rather than an algebraic slip model, the steam temperatures decrease in the peripheral gap and increase near the center of the steam generator. The net effect, however, is a decrease in the average steam outlet temperature as shown in Table 6.4.

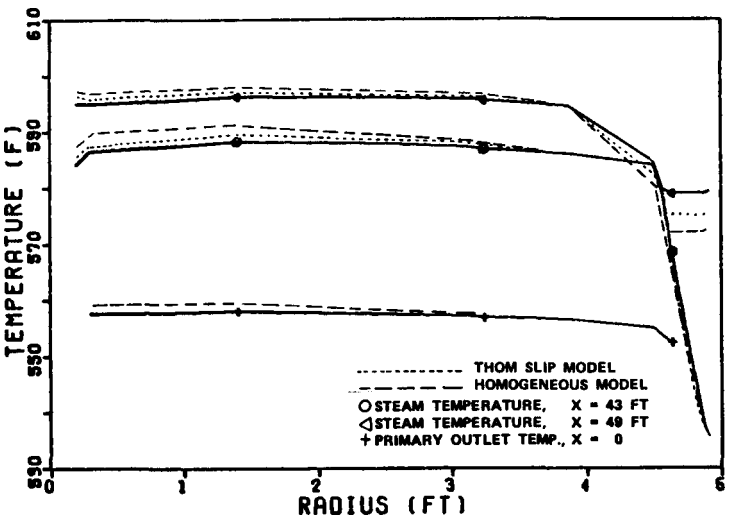

FIGURE 6.17 EFFECT OF CHANGES IN VOID FRACTION CORRELATION ON RADIAL TEMPERATURE PROFILES

Turbulent Mixing Coefficient

As shown in Figures 6.18 and 6.19, changes in the turbulent mixing coefficients have no influence on the quality profiles in the tube bundle. In the peripheral gap, however, large increases in the mixing coefficients increase the quality. Thus, with higher coefficients the diffusion of enthalpy from the tube bundle to the peripheral gap is greater. The effects that these changes in gap qualities have on steam temperatures are shown in Figures 6.20 and 6.21. Only the large increases (x 15.0 and x 50.0) in mixing coefficients show significant increases in peripheral gap steam temperature. In the other cases with mixing coefficients varied over a reasonable range of uncertainty (mixing coefficient multiplied by 0.2 and 5.0), the steam temperatures are only slightly changed near the 15th tube support plate.

The radial temperature profiles in Figures 6.22 and 6.23 show the changes in temperature gradients in the radial direction near the peripheral gap for the changes in mixing coefficients.

The results suggest that transport of enthalpy by radial diffusion contributes to the heating of the peripheral gap only when the mixing coefficient exceeds 0.05. Convective transport dominates for smaller mixing coefficients.

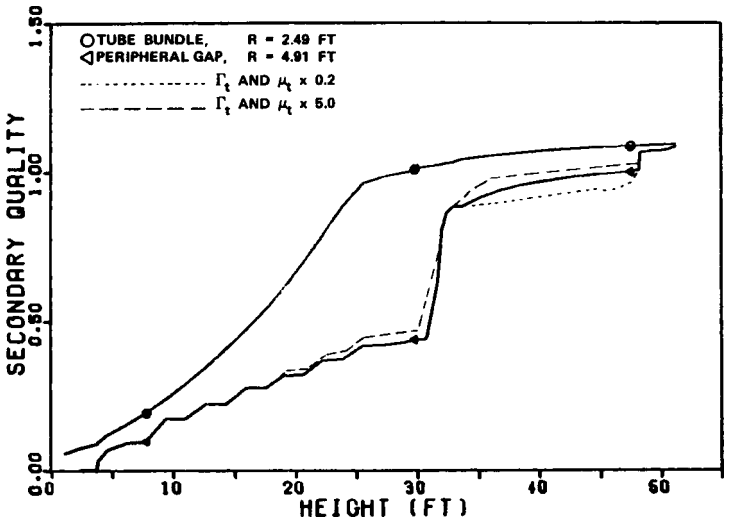

FIGURE 6.18 EFFECT OF CHANGES IN MIXING COEFFICIENTS ON QUALITY PROFILES

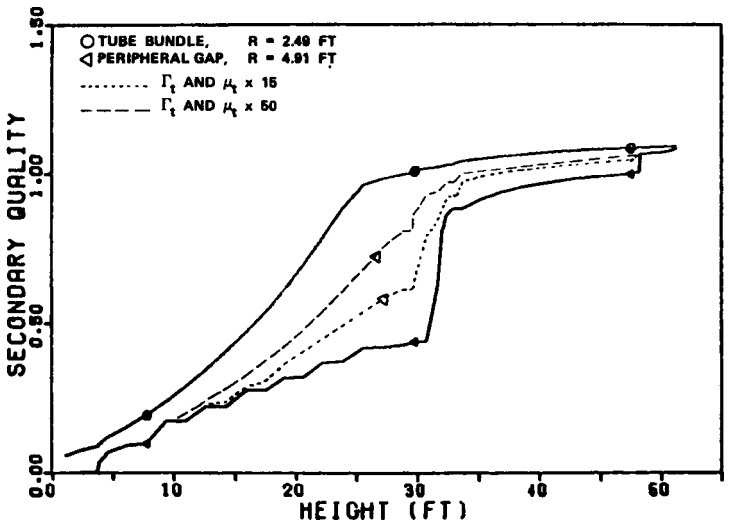

FIGURE 6.19 EFFECT OF LARGE CHANGES IN MIXING COEFFICIENTS ON QUALITY PROFILES

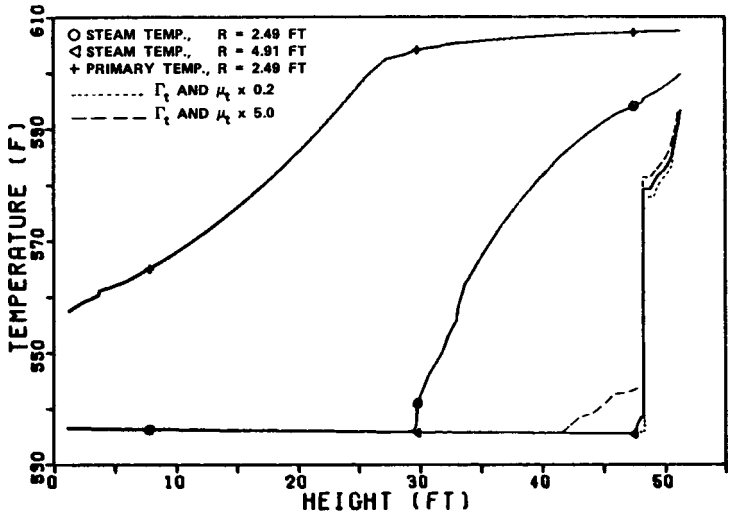

FIGURE 6.20 EFFECT OF CHANGES IN MIXING COEFFICIENTS ON AXIAL TEMPERATURE PROFILES

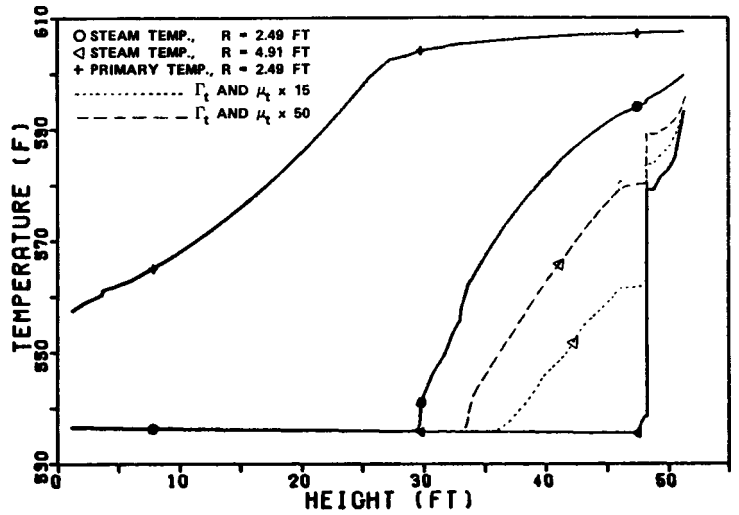

FIGURE 6.21 EFFECT OF LARGE CHANGES IN MIXING COEFFICIENTS ON AXIAL TEMPERATURE PROFILES

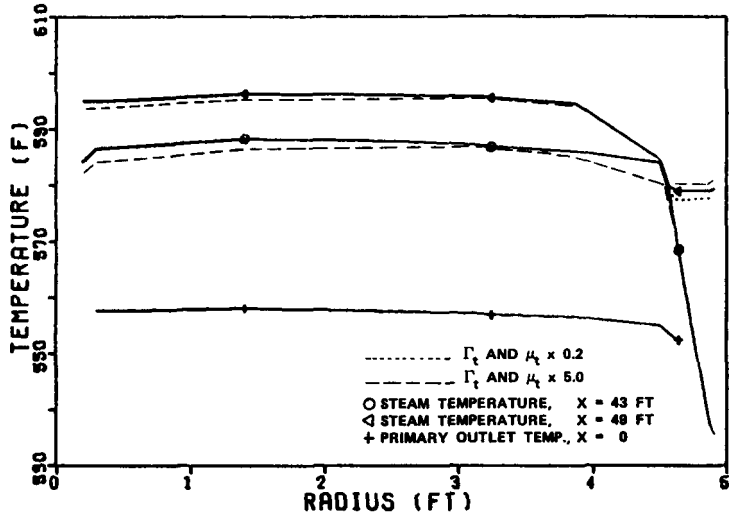

FIGURE 6.22 EFFECT OF CHANGES IN MIXING COEFFICIENTS ON RADIAL TEMPERATURE PROFILES

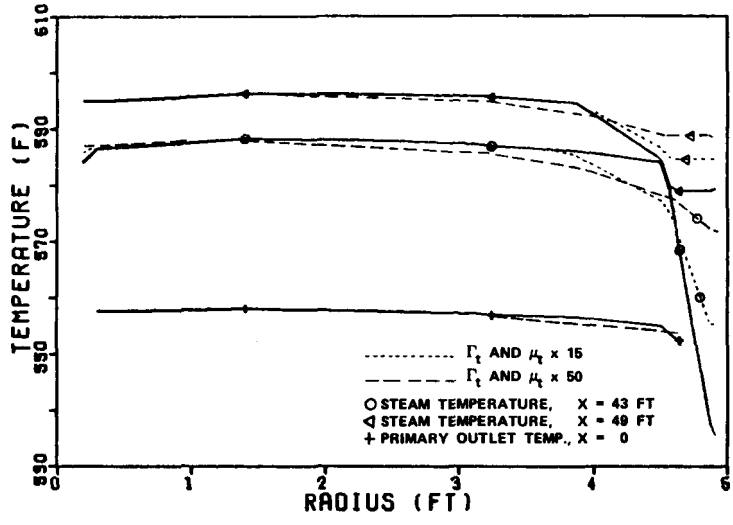

FIGURE 6.23 EFFECT OF LARGE CHANGES IN MIXING COEFFICIENTS ON RADIAL TEMPERATURE PROFILES

Tube Support Plate Resistance

The only significant effect of uniformly changing the tube support plate resistance by the same ratio in the bundle and the peripheral gap was to change the pressure profiles by the amounts shown in Figure 6.24. Other parameters such as quality, temperature, and axial velocity were nearly identical to the nominal values.

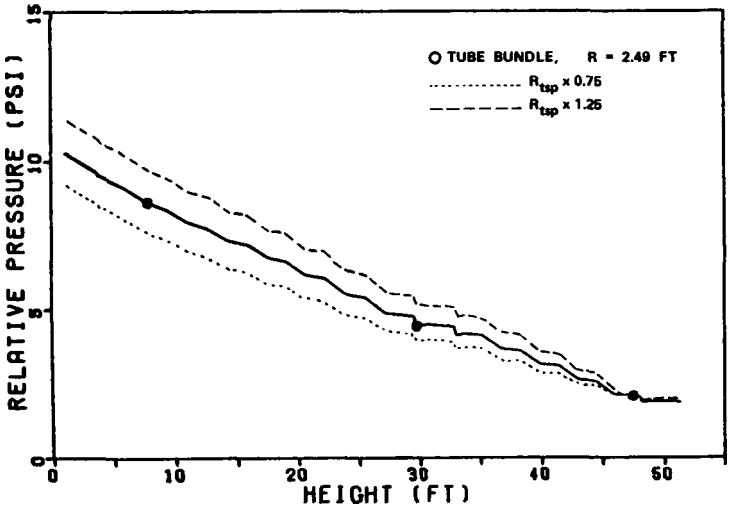

FIGURE 6.24 EFFECT OF CHANGES IN TUBE SUPPORT PLATE RESISTANCES ON THE PRESSURE PROFILE

The slope of the pressure drop versus height curves show that the changes in K factors primarily affect the pressure drop for those tube support plates in the top two-thirds of the steam generator. In the lower region, the axial velocities are much less than those in the high quality and superheat regions due to the changes in two-phase density. This is shown in Figure 6.16. Thus, in the low quality regions, tube support plate losses are small compared to the other loss terms in the axial momentum equation. This reinforces the applicability of K factors that were derived from Idelchik's single-phase data, since the support plates which are of importance are either in the single-phase superheat region or the high quality region that is nearly single-phase vapor.

Cross-Flow Resistance

The quality contours (Figures B.11 and B.12) show the effects of varying the cross-flow resistance. An increase in this parameter slightly reduces quality at the outer

radii and increases quality near the center-line. The changes in quality in the peripheral gap are shown in Figure 6.25. Only slight decreases in peripheral gap qualities were predicted for a 300% increase in the cross-flow resistance. The changes were not confined to the peripheral gap, but rather there was a general tilt in the radial quality and temperature distributions as shown in Figure 6.26.

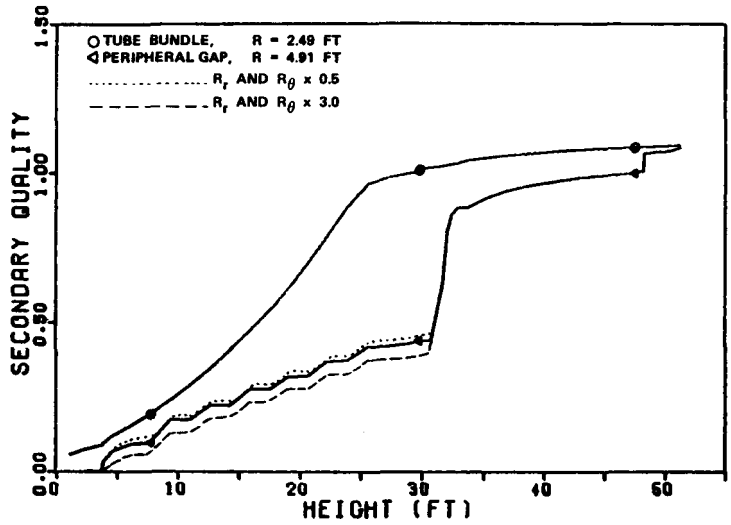

FIGURE 6.25 EFFECT OF CHANGES IN CROSS-FLOW RESISTANCE ON QUALITY PROFILES

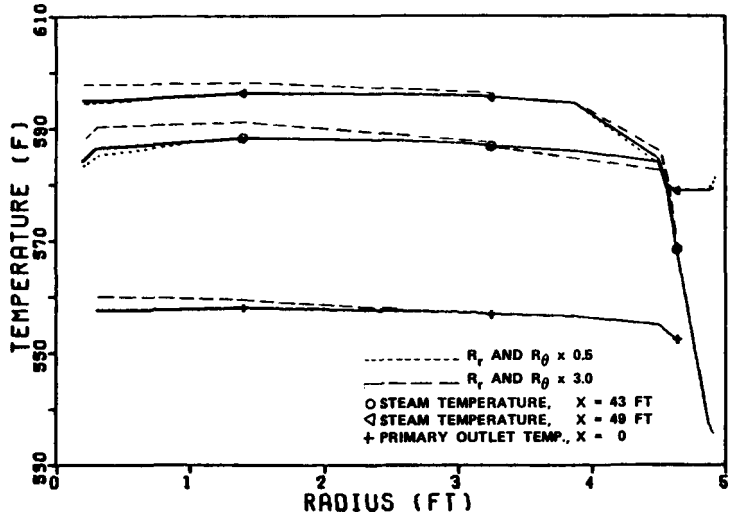

FIGURE 6.26 EFFECT OF CHANGES IN CROSS-FLOW RESISTANCE ON RADIAL TEMPERATURE PROFILES

The changes in cross-flow resistance had an effect on the pressure and velocity distributions near the steam outlet region. As shown in Figure 6.27, the cross-flow resistance affected the velocity distribution near the 15th tube support plate which is blocked at the peripheral gap and contains an outer rim of unbroached tube support plate holes. The figure shows that the axial velocity at the 49-foot elevation reaches a peak at the 4.3-foot radius as flow is diverted around the tube support plate blockage. An increase in cross-flow resistance increases the maximum velocity and narrows the width of the peak. Physically, this implies that a larger cross-flow resistance allows less of the diverted flow to be spread out over the tube bundle. Also since the total integrated mass flow rate is constant at a given elevation, an increase in the peak velocity decreases the axial velocities further into the tube bundle slightly as shown.

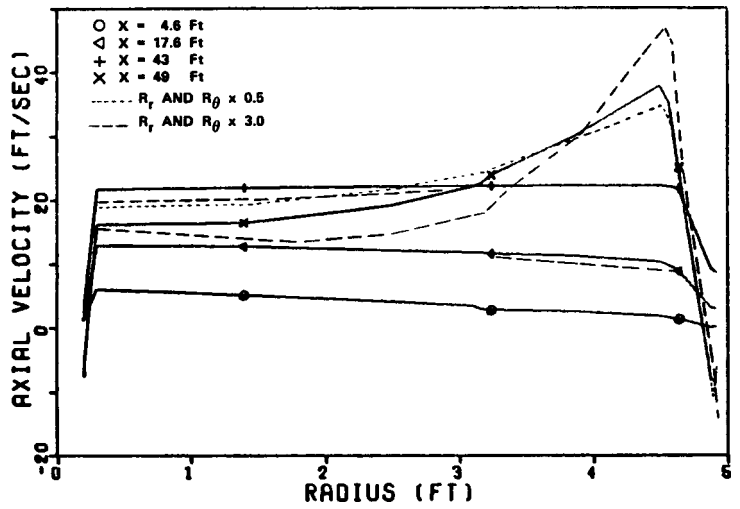

FIGURE 6.27 EFFECT OF CHANGES IN CROSS-FLOW RESISTANCE ON AXIAL VELOCITY VERSUS RADIAL POSITION

Figure 6.28 shows the effects of changes in cross-flow resistance on the axial pressure profile. Increases in the cross-flow resistance increased the pressure drop primarily between the steam outlet opening and the tube bundle. This resulted in an upward shift of the axial pressure profile with no observable change in the pressure distribution axially.

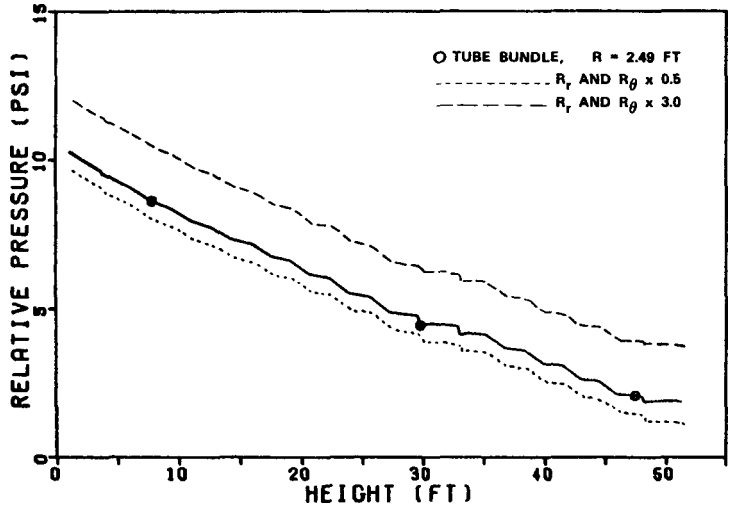

FIGURE 6.28 EFFECT OF CHANGES IN CROSS-FLOW RESISTANCE ON THE PRESSURE PROFILE

Nucleate Boiling Coefficient

Except for one set of data at pressures up to 550 psi, the steam water data on which the Chen correlation is based is limited to a pressure of 40 psia. The bulk of the higher pressure data is at higher heat fluxes, higher mass velocities, and lower steam quality than the OTSG operating conditions. Therefore, it is not too surprising to find that the Chen correlation predicts coefficients which are much lower than laboratory data obtained by B&W for an OTSG at operating conditions. The average value of the boiling coefficient from the Chen correlation was 4000 Btu/ft^2/hr/F. It varied between 3500 and 5000 Btu/ft^2/hr/F with the maximum occurring at higher qualities. The average value of the B&W proprietary correlation which represents the B&W test data was 7 to 7.5 times the value predicted by Chen. Such large differences in the nucleate boiling coefficient result in significant changes in the predicted primary and secondary temperatures shown in Figure 6.29. A 50 percent reduction in the B&W nucleate boiling coefficient has a much smaller effect (Figure 6.29).

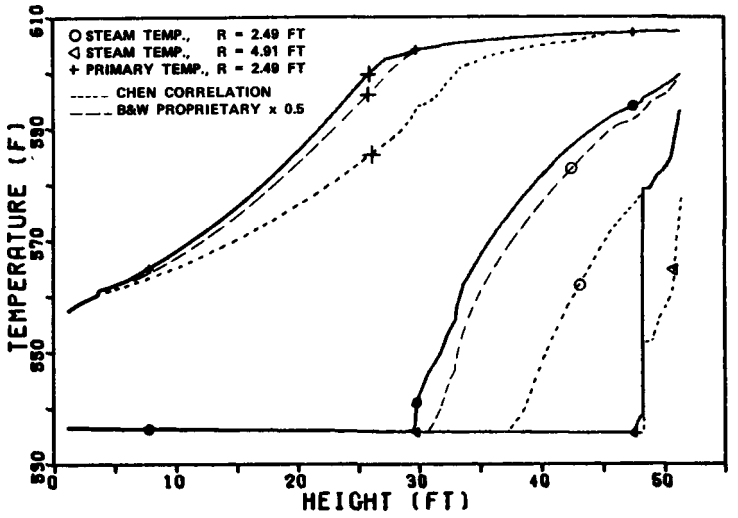

FIGURE 6.29 EFFECT OF CHANGES IN NUCLEATE BOILING COEFFICIENT ON AXIAL TEMPERATURE PROFILES

Superheated Steam Coefficient

The effect of changing the superheated steam heat transfer coefficient ±10% is shown in Figure 6.30. In the tube bundle, temperatures increase approximately 2°F for a 10% increase in the coefficient. The changes are essentially one-dimensional in the axial direction as shown in Figure 6.31. The changes in the heat transfer coefficient only shift the temperatures by an equal amount at each radial position. Other parameters, such as pressure and velocity, were not significantly affected.

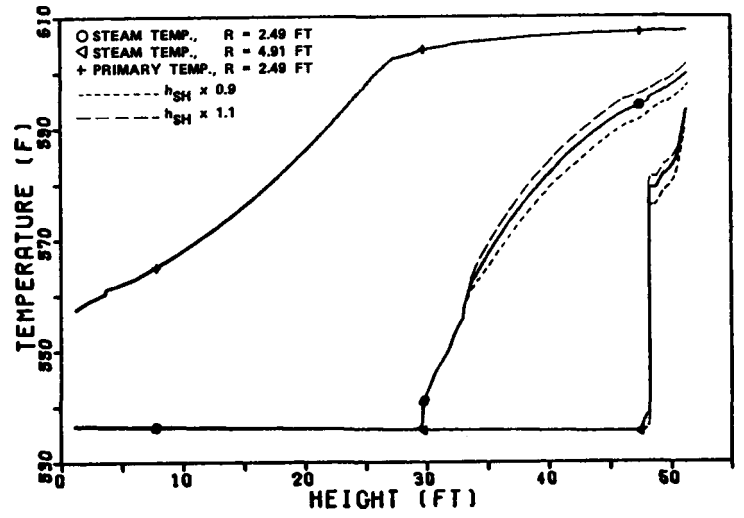

FIGURE 6.30 EFFECT OF CHANGES IN SUPERHEATED STEAM COEFFICIENT ON AXIAL TEMPERATURE PROFILES

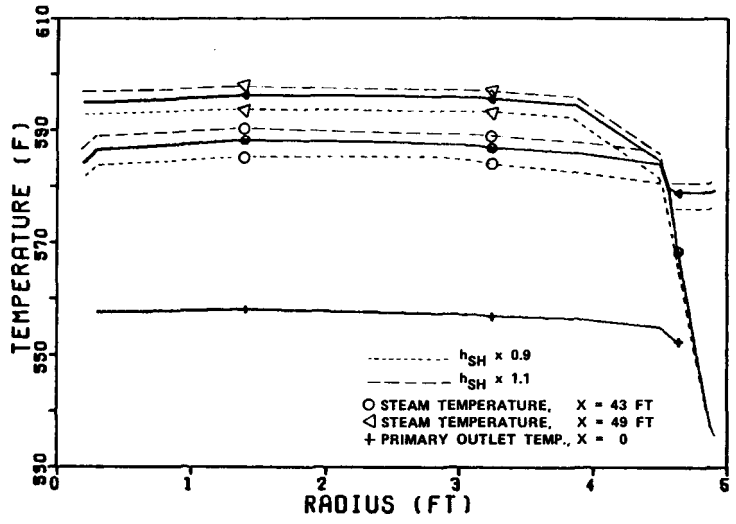

FIGURE 6.31 EFFECT OF CHANGES IN SUPERHEATED STEAM COEFFICIENT ON RADIAL TEMPERATURE PROFILES

Film Dryout Quality

As in the case of superheated steam heat transfer coefficient, the changes in film dryout quality primarily affected the steam temperatures as shown in Figure 6.32. The changes were also one-dimensional as shown in Figure 6.33, since the radial temperatures were changed by a constant increment at each radial position. An increase in the film dryout quality by 3% resulted in an increase in steam temperature of about 1.5°F, and vice-versa. Increasing the film dryout quality decreased the film boiling region which increased the superheated steam heat transfer area raising the outlet steam temperature.

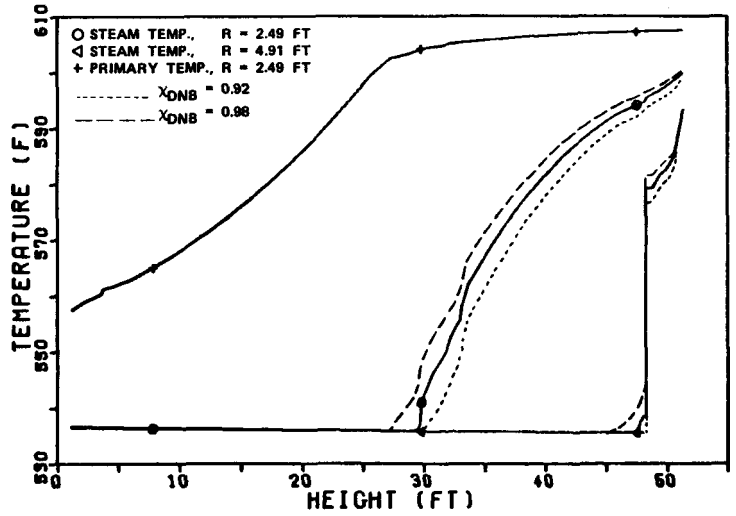

FIGURE 6.32 EFFECT OF CHANGES IN FILM DRYOUT QUALITY ON AXIAL TEMPERATURE PROFILES

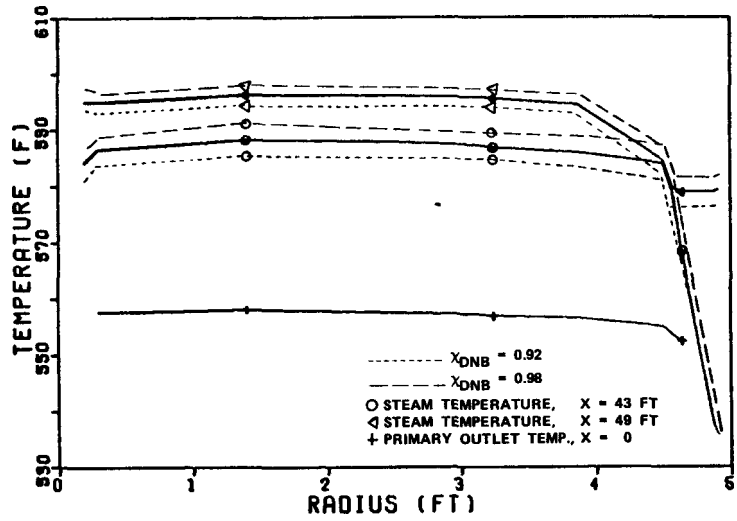

FIGURE 6.33 EFFECT OF CHANGES IN FILM DRYOUT QUALITY ON RADIAL TEMPERATURE PROFILES

Number of Axial Nodes

Performance predictions were made with three axial grid spacings corresponding to 41, 54 (nominal), and 115 axial nodes. The axial node spacing for the nominal run is identical to that shown by Figure 5.5. All of these runs were made with the regular support plate model for all support plates other than 1, 9, 10, and 15. The tube support plate axial resistance for the regular support plate model is averaged over the control volume, radial and circumferential resistances are neglected, and the flow resistance provided by the support plate in the peripheral gap is modeled as described in Section 5.2. For the tube support plates represented by the regular support plate model, the number of control volumes per support plate span varied as follows: 41 nodes, one control volume; 54 nodes, two control volumes (Figure 5.7); and 115 nodes, six control volumes. For two and six nodes per span, the support plate axial resistance was concentrated in the control volume containing the support plate rather than spread over the entire span.

For these three runs, grid spacing has little effect on bundle average performance as shown by Table 6.4. However, Figures 6.34 and 6.35 show that the axial grid spacing affects the local quality and velocity in the peripheral gap. The results for 54 and 115 nodes agree and differ from the results for 41 nodes. The differences can be explained as follows:

For 41 axial nodes, the axial resistance of the tube support plate is evenly distributed over the entire height of the steam generator. Therefore, there is no discontinuity in axial resistance at the support plate to promote flow diversion from the gap to the bundle. As a result, the axial velocity in the peripheral gap changes gradually as indicated in Figure 6.35. However, for 54 and 115 nodes the support plate axial resistance is concentrated in one control volume per support plate span. The resulting discontinuity in axial resistances at the support plate causes cross-flow between the peripheral gap and the tube bundle. This flow in and out of the gap produces an oscillating axial flow in the peripheral gap as shown by Figure 6.35. The predicted characteristics of the oscillatary flow are very similar for both the two and six axial nodes per tube support plate span (54 and 115 axial nodes).

As noted in the discussion of the effect of the void fraction correlation on peripheral gap quality, the gap quality is primarily determined by the tube bundle axial pressure gradient between, but not including, support plates. Both the 54 node and 115 node case predict the same bundle pressure gradient between support plates and therefore, the peripheral gap quality for both runs is almost identical (Figure 6.34). However, the bundle axial pressure gradient for the 41 node run includes the tube support plate resistance and is therefore greater than the gradient for the 54 and 115 node runs.

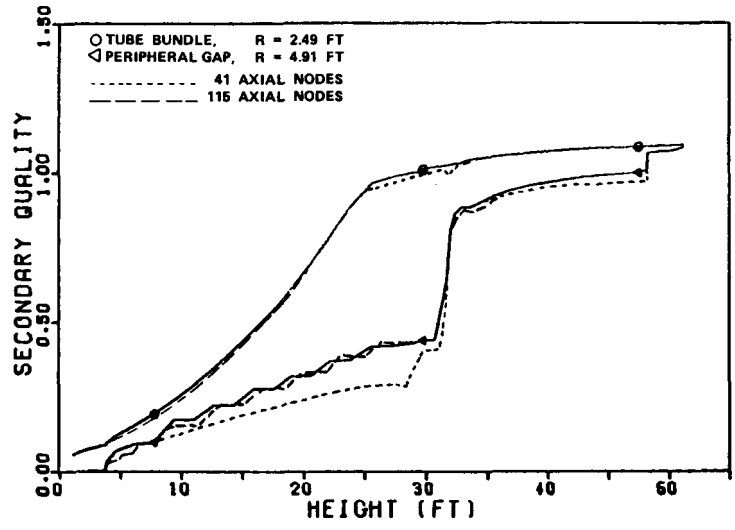

FIGURE 6.34 EFFECT OF CHANGES IN THE NUMBER OF AXIAL NODES ON QUALITY PROFILES

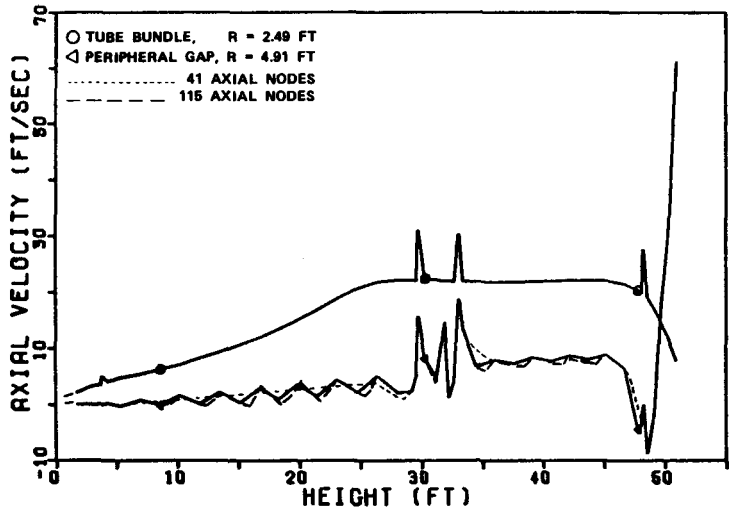

FIGURE 6.35 EFFECT OF CHANGES IN THE NUMBER OF AXIAL NODES ON AXIAL VELOCITY PROFILES

The large bundle pressure gradient requires a higher density, lower quality two-phase mixture in the peripheral gap to achieve a momentum balance. This is verified by the quality profiles shown in Figure 6.34.

In summary, to correctly predict quality in the peripheral gap it is necessary to model the tube support plate axial resistance as a discontinuity rather than averaging it over the entire span between support plates. However, once this is done, two axial nodes per span appear to be adequate for predicting the general level of gap quality and velocity. If detailed predictions in the immediate vicinity of a support plate are required, more axial nodes would be necessary.

Slight changes in the film dryout height can be inferred from Figure 6.36 by the primary side axial temperature distributions. The elevation at which the axial gradient in primary temperature suddenly decreases corresponds to film dryout. As the number of axial nodes is increased, film dryout elevation decreases as shown. This change in film dryout position also slightly changes the axial steam temperature profiles as shown.

For the 115 axial node quality contour shown in Figure B.20, it was noted that quality in the center untubed region below the 11th, 13th, and 14th tube support plates appear to be unrealistic since there are closed quality contours in these regions. The qualities at these locations did not converge as rapidly as those in the remainder of the steam generator. The effect on steam temperature is shown in Figure 6.37. The figure shows that the decrease in temperature is con-

fined within a 1.5-foot distance from the center. The temperature changes in the rest of the steam generator appear reasonable for a change in axial grid.

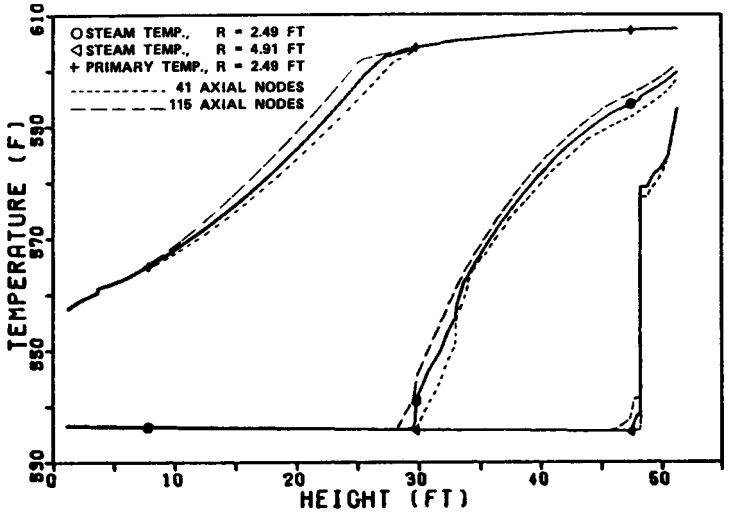

FIGURE 6.36 EFFECT OF CHANGES IN THE NUMBER OF AXIAL NODES ON AXIAL TEMPERATURE PROFILES

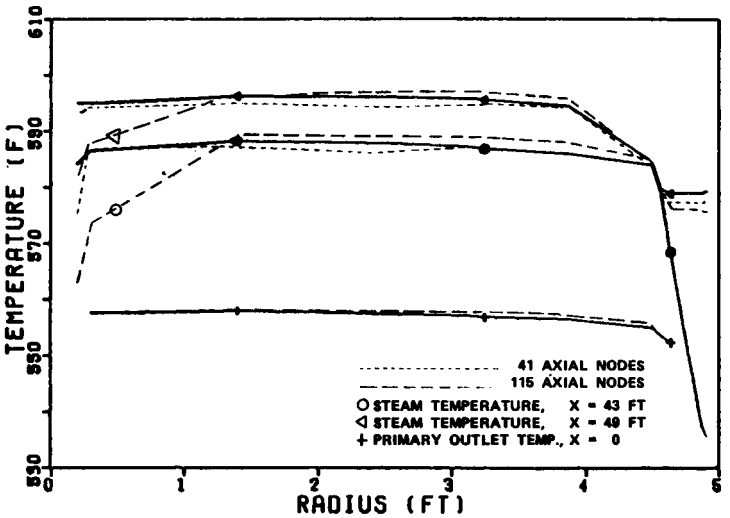

FIGURE 6.37 EFFECT OF CHANGES IN THE NUMBER OF AXIAL NODES ON RADIAL TEMPERATURE PROFILES

Corrected Nominal Run

As was discussed previously, after the runs presented above were completed, it was discovered that the porosities for the main nodes at the bottom faces of the four fine grid tube support plates were inadvertently set to the bundle porosities rather than tube support plate porosities. These porosities were corrected and a new nominal run was made. Comparisons between the corrected nominal and original nominal quality profiles are shown in Figure 6.38. The agreement is good in the tube bundle and in the peripheral gap below the 9th tube support plate. Above the 9th tube support plate, which is the first FGSP model in the high velocity single-phase region, the peripheral gap quality differs slightly. The principal effect of the change was in the pressure drop across the 9th 10th, and 15th fine grid tube support plates as shown in Figure 6.39. Since the porosity revision decreased the porosity for the axial momentum control volumes within the support plates to 0.232, the tube support plate velocity increased and the pressure drop increased as shown.

It can also be seen from Figure 6.39 that the corrected FGSP model predicts larger tube support plate pressure drops than the RSP model. This is discussed further in connection with the run that was made with all FGSP models.

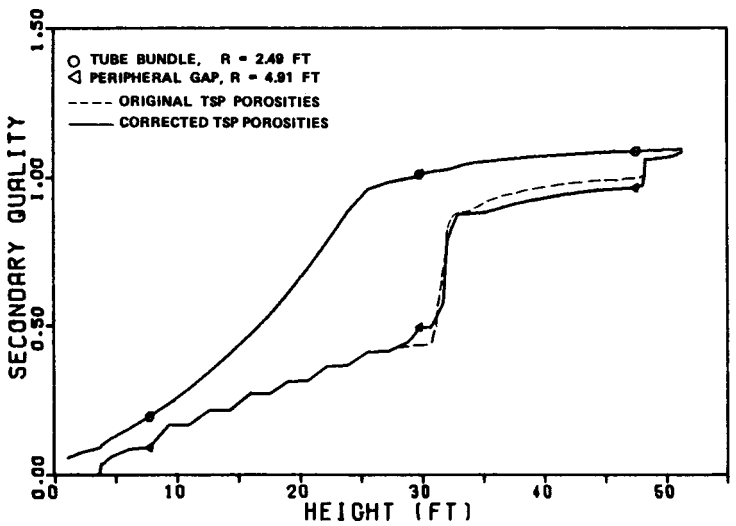

FIGURE 6.38 COMPARISON OF THE ORIGINAL AND CORRECTED NOMINAL QUALITY PROFILES

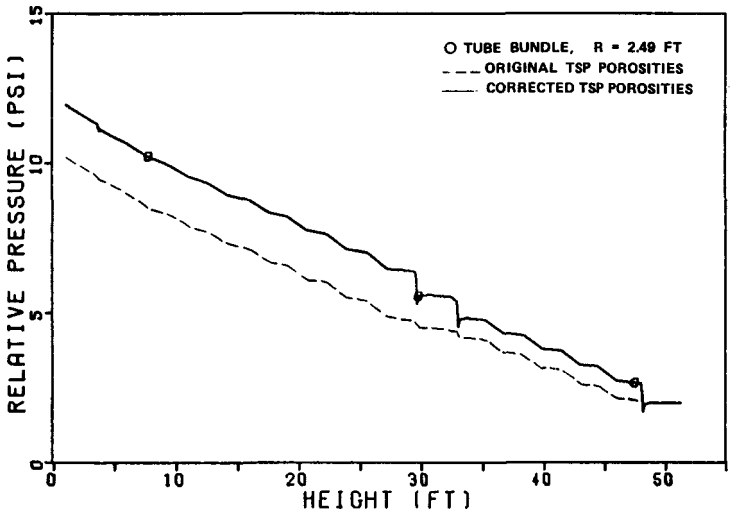

FIGURE 6.39 COMPARISON OF THE ORIGINAL AND CORRECTED NOMINAL PRESSURE PROFILES

Based on the agreement between the original and corrected nominal run as shown in Figure 6.38, the conclusions reached using the incorrect tube support plate porosities, as presented in the previous paragraphs, are believed to be unaffected. However, after the error was discovered, the remaining runs were made with the corrected tube support plate porosities and are compared with the corrected nominal run.

Peripheral Gap K Factor

As discussed previously, varying the tube support plate K factors by a constant factor at all positions within the support plate had no effect on steam conditions in either the peripheral gap or tube bundle. Only the pressure changed with no observable change in enthalpy. By changing the K factor only in the peripheral gap, the effect of changing the ratio of K factors between the tube bundle and peripheral gap can be evaluated.

In Figure 6.40, the changes in peripheral gap qualities are shown for ±50% changes in peripheral gap K factors for the RSP tube support plates. Somewhat surprisingly, the 50% increase in the flow resistance causes the peripheral gap quality to increase only slightly. However, since changes in the gap K factor do not change the bundle pressure gradient between support plates, the simple model presented in the section on void fraction correlations would indicate that changes in K should have little effect on gap quality as substantiated by Figure 6.40. The small

quality changes that do occur are consistent with the peripheral gap axial velocity shown in Figure 6.41; an increase in K reduces the average velocity in the gap and increases quality.

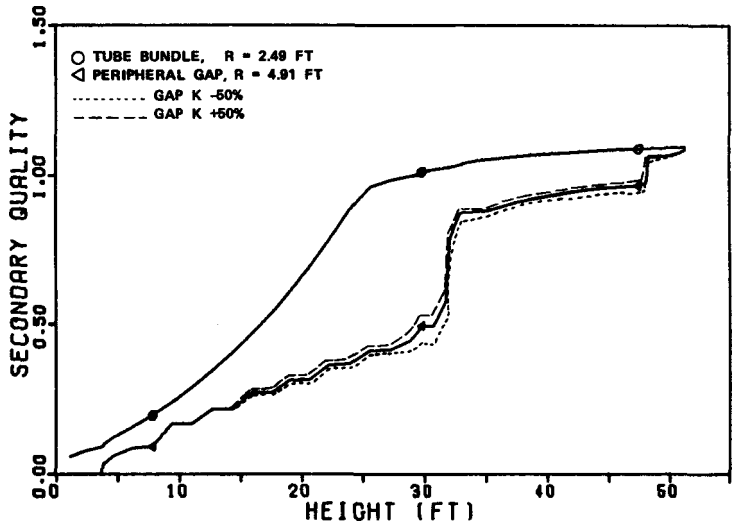

FIGURE 6.40 EFFECT OF PERIPHERAL GAP TUBE SUPPORT PLATE K FACTOR ON QUALITY PROFILES

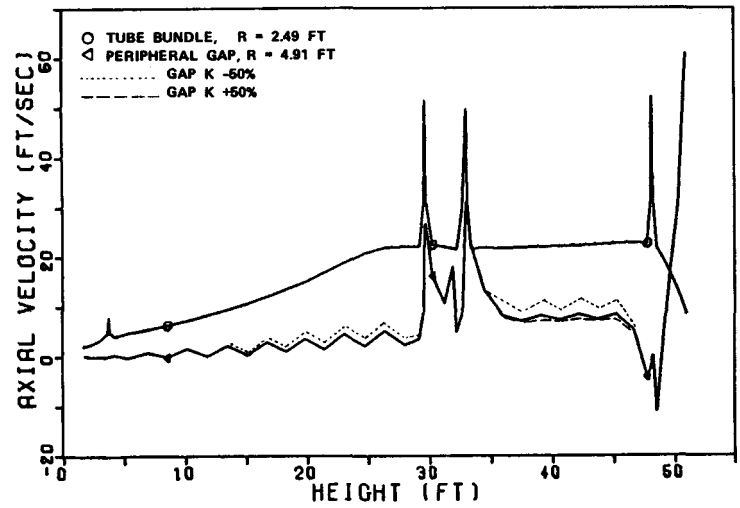

FIGURE 6.41 EFFECT OF PERIPHERAL GAP TUBE SUPPORT PLATE K FACTOR ON AXIAL VELOCITY PROFILES

Number of Radial Nodes

Increasing the number of radial nodes to 21 had only a small effect on the quality profiles in the peripheral gap and no effect in the tube bundle as shown in Figure 6.42. Decreasing the number of radial nodes to 11 had even less effect in the peripheral gap and also no effect in the tube bundle. This again would be expected since changing the number of radial nodes does not affect the axial pressure gradient.

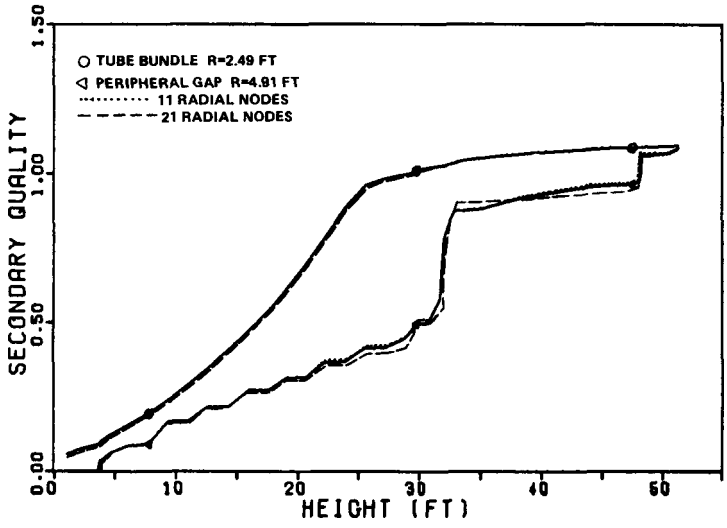

FIGURE 6.42 EFFECT OF CHANGES IN THE NUMBER OF RADIAL NODES ON QUALITY PROFILES

However, as shown in Figure B.26, the addition of radial nodes changes the quality contours in and around the center untubed region. The contours show that steam qualities are lower in the center untubed region with 21 radial nodes compared with 15 radial nodes for the corrected nominal run. The effect that this has on steam temperature is shown in Figure 6.43. In the center, steam temperatures are reduced by as much as 10°F. The results of the radial grid spacing runs indicate that the spacing in the center region of the steam generator must be finer than that employed in this study.

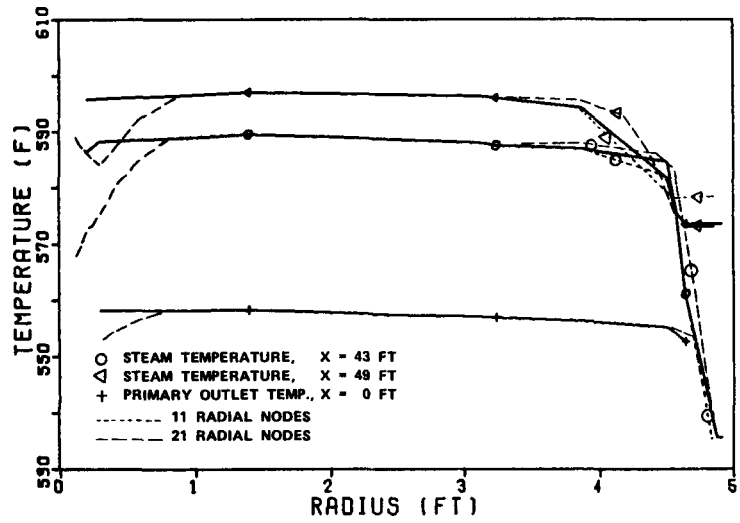

FIGURE 6.43 EFFECT OF CHANGES IN THE NUMBER OF RADIAL NODES ON RADIAL TEMPERATURE PROFILES

Fine Grid Support Plate Model

Steam generator performance was calculated using the Fine Grid Support Plate (FGSP) model at all support plate locations. The finite difference equations are based on the assumption that porosity changes and area changes across a control volume are small. This is clearly not true for the control volumes in the FGSP model. Because this assumption is violated, the FGSP model over-predicts the pressure drop across a support plate as compared to B&W experimental data (Figure 6.44), even though the loss factor is based on this data. On the other hand, the RSP model, which does not include a porosity change predicts pressure gradients which agree with experimental data. Note that this FGSP run was made with f in Eq. 5.1 set equal to 1.0.

Figure 6.45 compares the quality predicted with the RSP model (nominal run) and the FGSP model. Figure 6.46 compares predicted temperatures. Although there is close agreement, it is possible that the results could change if the assumptions made in deriving the finite difference equations were revised to correctly allow for area and porosity changes.

As shown in Table 6.4, the predicted outlet bundle average steam temperature is 2.6°F higher for the FGSP model. The increased temperature occurs mostly in the superheat region. It is possible that the increased heat transfer results from the assumptions made in the analysis and could change if the assumptions were modified.

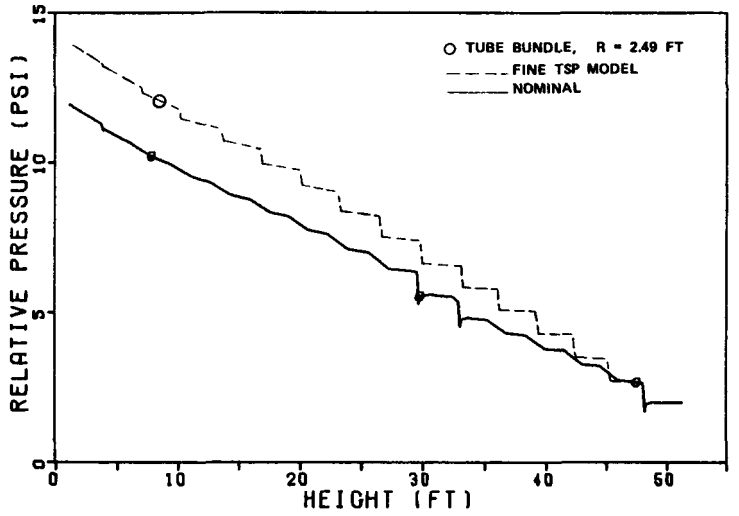

FIGURE 6.44 COMPARISON OF FINE GRID TUBE SUPPORT PLATE AND REGULAR GRID SUPPORT PLATE PRESSURE DROPS

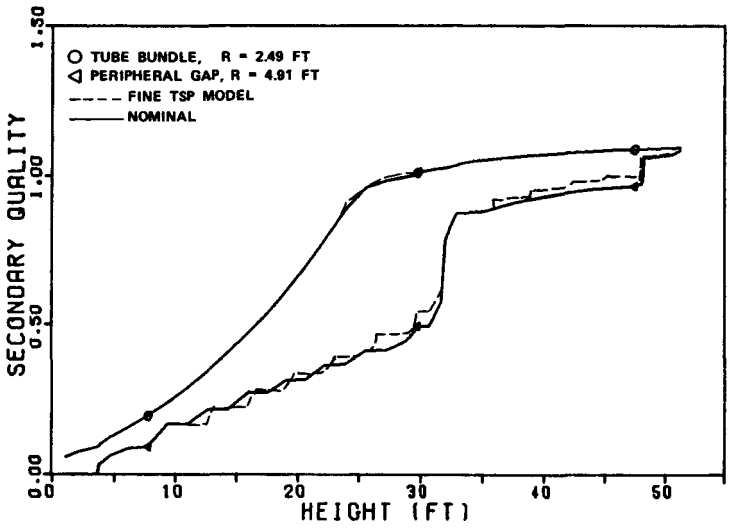

FIGURE 6.45 COMPARISON OF QUALITY PROFILES FOR FINE GRID AND REGULAR GRID TUBE SUPPORT PLATE MODELS

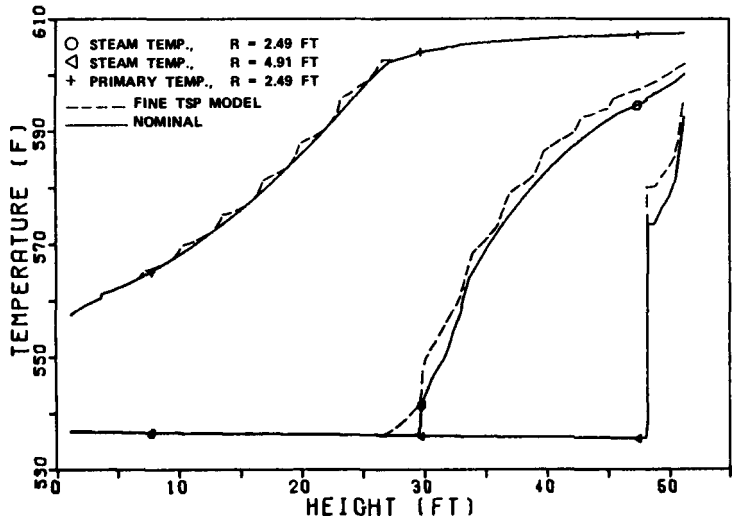

FIGURE 6.46 COMPARISON OF AXIAL TEMPERATURE PROFILES FOR FINE GRID AND REGULAR GRID TUBE SUPPORT PLATE MODELS

6.2.3 Circumferential Open Lane Study Results

As discussed in Section 6.2.1, the circumferential open lane (COL) is an approximate two-dimensional model for the TMI-2 radial open lane. The width of the COL and the tube support plate resistance are identical to those used for the radial lane, but the total cross-sectional area is π times the radial lane area. With the COL, the sensitivity of local lane conditions can be determined more economically than with a three-dimensional radial lane model.

For the COL study, the effects of changes in tube support plate modeling detail and void fraction were examined. The nominal run employed the correlations and axial grid system used for the 2-D sensitivity study.

The following cases were run:

1) FGSP Model, f = 0.487

   Nominal : FGSP models at TSPs 1, 9, 10, and 15

   Changes : All TSPs with FGSP models

2) Void Fraction, f = 0.487

Nominal : Smith correlation (K_s = 0)

Changes : homogeneous model, Zuber correlation with bundle average mass velocity, and Zuber correlation with local lane mass velocity

For the FGSP study, the steam generator was modeled with the same axial grid that was used for the FGSP run in the 2-D sensitivity study. As in that case, FGSP models were used at all tube support plates for comparison with the RSP models used in the nominal run. The tube support plate axial flow resistance for the circumferential open lane (fine) grid support plate (COL FGSP) run was modified to obtain agreement with the RSP results. By trial and error, a value of f = 0.487 (Eq. 5.1) was found to produce equal steam generator total pressure drop for both the FGSP and RSP calculations. Using f = 0.487 compensates for the error in axial pressure gradient that results from the assumptions used in deriving the finite difference equations. However, this adjustment probably does not fully account for the effect of the assumptions on the predicted values of other parameters.

The Smith correlation was used in the nominal COL run. The homogeneous model given by Eq. 3.39 was used as one of the changes. Two cases of the Zuber void fraction correlation given by Eq. 3.50 were also run. The first contained the average steam generator mass velocity defined by Eq. 3.55 and 3.56 at all positions within the steam generator. The second case used the local mass velocity, ρU, in the COL and the average steam generator mass velocity at all other positions.

The local value of mass velocity can not be used at all locations within the steam generator because, in regions of very low mass velocity or reverse flow, the Zuber correlation is not valid. Since the bundle average mass velocity is always within the range of validity of the Zuber correlation, it was selected as a way to avoid the problem of low mass velocities. Since it had been found previously that steam conditions are affected by void fraction only in untubed regions, another case was run with the COL void fraction based on the local COL mass velocity and the bundle and peripheral gap void fraction based on the bundle average mass velocity. The COL mass velocities were also always within the range of validity of the Zuber correlation.

The nominal COL run used the axial grid that was used for the 2-D sensitivity study (Figure 5.7). The f factor for the four FGSP models used in the nominal run was also set to 0.487. The total pressure drop for the nominal run and the FGSP run are identical as shown in Figure 6.47.

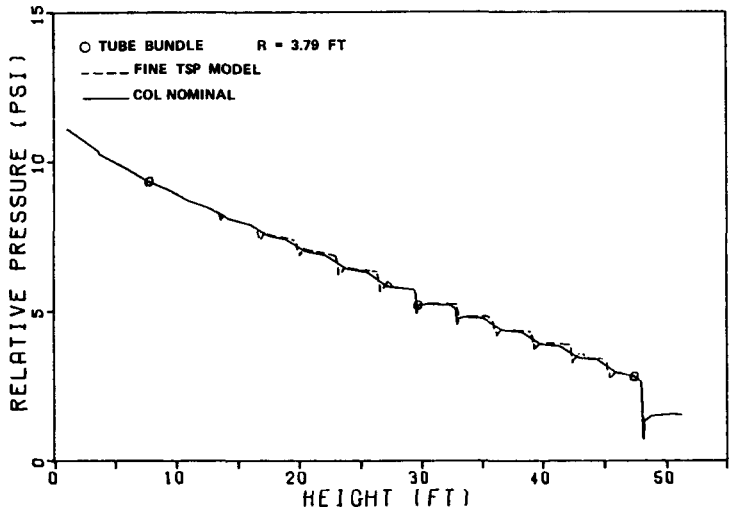

FIGURE 6.47 COMPARISON OF COL NOMINAL AND COL FINE GRID TSP MODEL WITH f = 0.487

The overall results from each of the runs made in the COL study are presented in Table 6.5. The COL nominal run values are given along with the perturbations for the other cases. The film dryout height is given at a radius of 3.79 feet, which is midway between the COL and peripheral gap. Steam outlet temperature (T_S), total pressure drop (ΔP), and the bleed flow rate ($\dot{m}_B$) are also given.

TABLE 6.5

CIRCUMFERENTIAL OPEN LANE STUDY RESULTS

	T_S (F)	ΔP (psi)	$\dot{M}_B$ (10^6 lbm/hr)	Film Dryout Height
Nominal (-30 iterations)	589.0	11.145	0.8793	25.160
Nominal (last iteration)	589.0	11.144	0.8790	25.160
Difference	0.0	0.001	0.0003	0.0
FGSP Model	2.9	- 0.005	-0.0578	- 0.286
Homogeneous Void Fraction	- 5.1	- 1.679	0.0834	- 1.396
Zuber Average G	- 1.1	- 0.663	0.0252	- 0.262
Zuber Local Lane G	- 1.4	- 0.695	0.0185	- 0.626

The following are noted from Table 6.5:

- The 2.9°F steam temperature increase for the COL FGSP run was close to the 2.6°F increase for the 2-D sensitivity study FGSP run given in Table 6.4.
- Because of the large untubed areas associated with the COL, the change to the homogeneous model decreased the steam temperature (-5.1°F) by a greater amount than that obtained without the COL (-1.9°F, Table 6.4).
- The Zuber void fraction cases with average and local mass velocities gave similar results. The Zuber correlation with the local lane mass velocity resulted in a slightly larger decrease in steam temperature (-1.4°F) than with the average mass velocity (-1.1°F).
- The Zuber correlation predicts a lower velocity ratio than the Smith correlation used for the nominal COL run. Therefore, the perturbations from the nominal shown in Table 6.5 are in the same direction as the perturbations resulting from the homogeneous void fraction correlation, but of a lesser magnitude. The Zuber correlation results are closer to the Smith correlation results (nominal) than to the homogeneous void fraction results.

The quality contours for the COL study are given in Appendix B (Figures B.27 - B.30). Several features from the quality contours are noted below:

- The nominal and FGSP model have similar quality contours in and around the COL.
- The homogeneous model shows a larger decrease in steam quality in and around the COL than the nominal case. Tube bundle qualities in the center of the steam generator increased as was the case for the 2-D sensitivity study homogeneous model run.
- The Zuber void fraction case with average steam generator mass velocity predicts COL conditions that are between the nominal Smith correlation and the homogeneous model. The Zuber quality contours with average mass velocity are very similar to the Zuber quality contours with local COL mass velocity (not shown).

Additional details for the COL sensitivity study are provided in Figures 6.47 through 6.53. Axial profiles are given for various steam generator conditions. They are described in the following paragraphs.

COL Study - FGSP Model

As is shown in Figure 6.47, the pressure drops for the COL FGSP model were set equal to the RSP pressure drops in the nominal run. This was accomplished by setting f = 0.487 in Eq. 5.1.

For the 2-D sensitivity runs without an open lane, the quality profiles in the peripheral gap for the FGSP case were in good agreement with the nominal run (Figure 6.45). In that case, however, tube support plate pressure drops were not in agreement (Figure 6.44) because an f of 1.0 was used in Eq. 5.1. The quality profiles in the peripheral gap for the COL FGSP run are shown in Figure 6.48. Here, the FGSP model predicts a higher gap quality than the nominal case. For the COL FGSP run, the f was set equal to 0.487 to achieve agreement with the RSP (nominal) pressure drop as shown in Figure 6.47. It is not clear why the peripheral gap qualities are different for the FGSP runs (Figures 6.45 and 6.48) with and without the circumferential open lane. The difference could be partly due to the use of different values of f, to the presence of the open lane, or to some other factor.

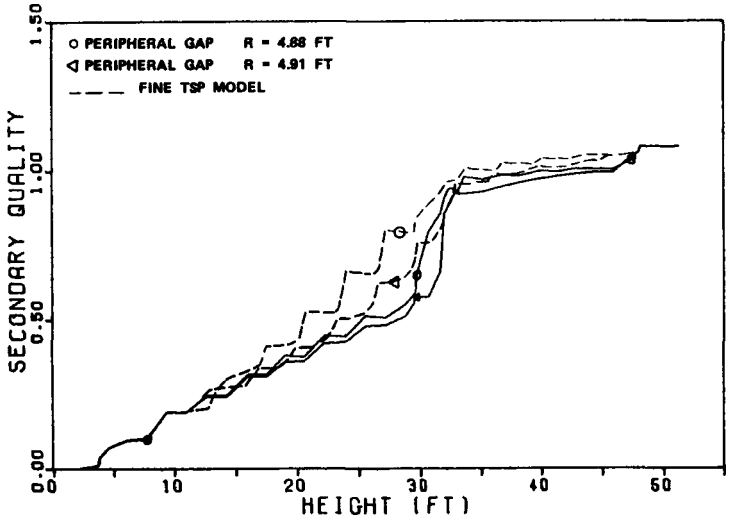

FIGURE 6.48 COMPARISON OF COL NOMINAL AND COL FINE GRID PERIPHERAL GAP QUALITIES

Although the FGSP peripheral gap qualities are higher than the nominal values, conditions in other regions of the steam generator are in good agreement. As shown in Figure 6.49, the qualities in both the COL and the tube bundle compare favorably.

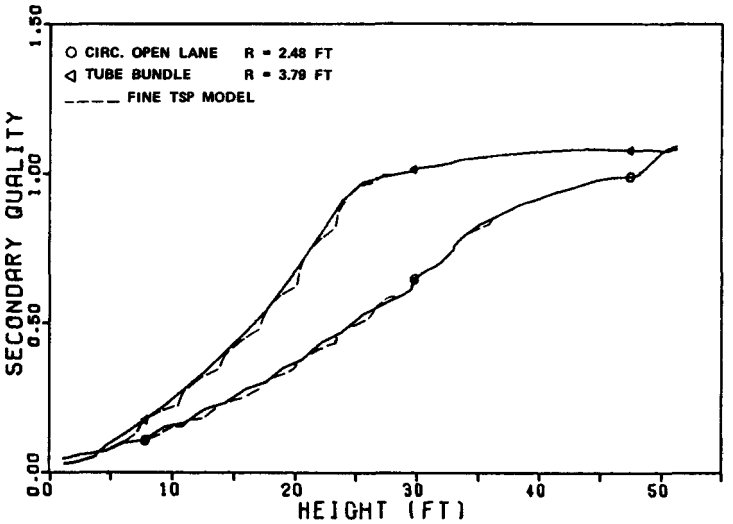

FIGURE 6.49 COMPARISON OF COL NOMINAL AND COL FINE GRID QUALITY PROFILES

Comparisons of axial velocity and steam temperature are given in Figures 6.50 and 6.51. The FGSP axial velocity profiles show the increase in velocity at each tube support plate restricion. The velocity between the support plates is in good agreement between the FGSP and nominal cases in both the COL and tube bundle. The steam temperatures in Figure 6.51 are higher in the tube bundle with the FGSP model due to a slight decrease in the boiling length.

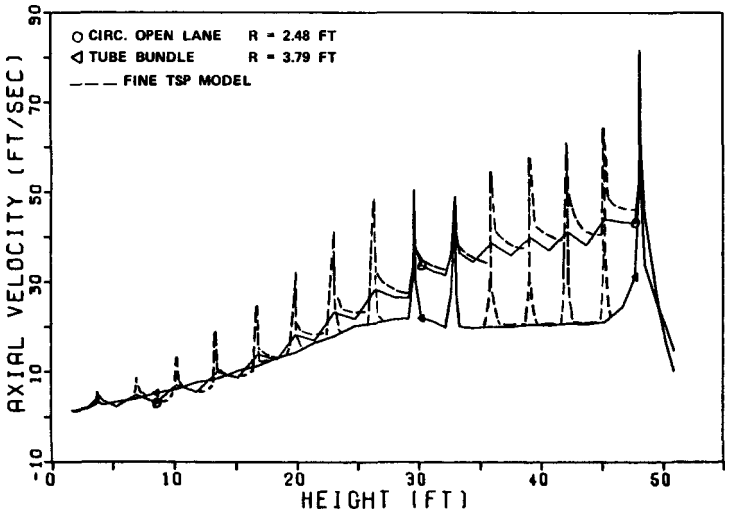

FIGURE 6.50 COMPARISON OF COL NOMINAL AND COL FINE GRID AXIAL VELOCITY PROFILES

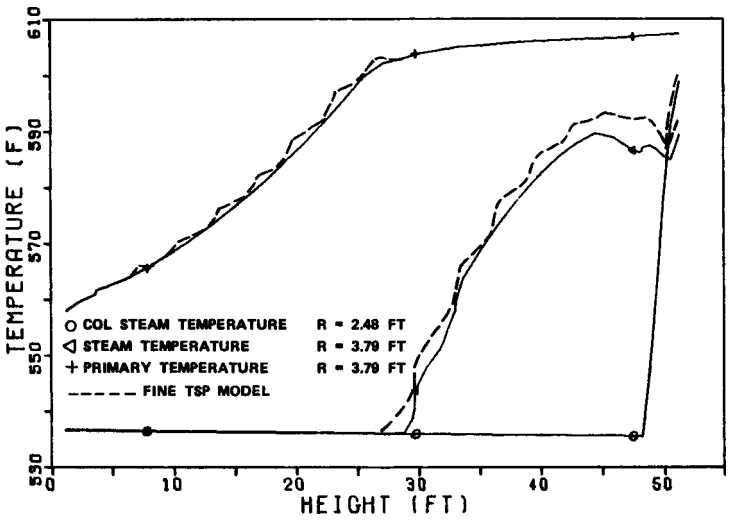

FIGURE 6.51 COMPARISON OF COL NOMINAL AND COL FINE GRID AXIAL TEMPERATURE PROFILES

COL Study - Void Fraction

The changes in COL and tube bundle qualities are shown in Figure 6.52 for changes in the void fraction correlation. Significant decreases in COL qualities are predicted with the homogeneous model and Zuber void fraction cases as compared to the nominal Smith correlation. This result is similar to that obtained for the peripheral gap for the void fraction cases examined in Section 6.2.2. That is, an increased velocity ratio produces an increase in the quality in an untubed region. Only a slight difference in qualities is shown between the Zuber correlation with local lane mass velocity and the Zuber correlation with average mass velocities, indicating that the simplifying assumption about the mass velocity term in the correlation has only a slight effect on the predictions.

The axial velocity profiles are shown in Figure 6.53. The tube bundle axial velocities are unaffected by changes in void fraction models. In the COL, the axial velocity increases in the low quality region and decreases in the superheat region by changing to the homogeneous and Zuber correlations.

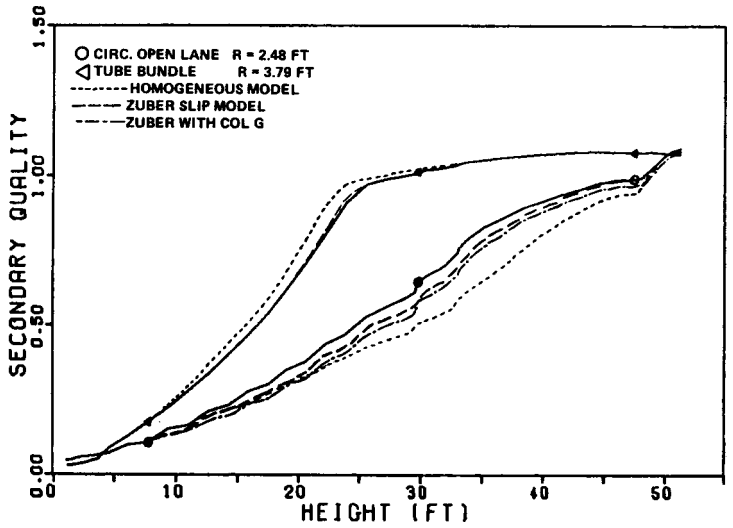

FIGURE 6.52 EFFECT OF CHANGES IN VOID FRACTION ON QUALITY PROFILES

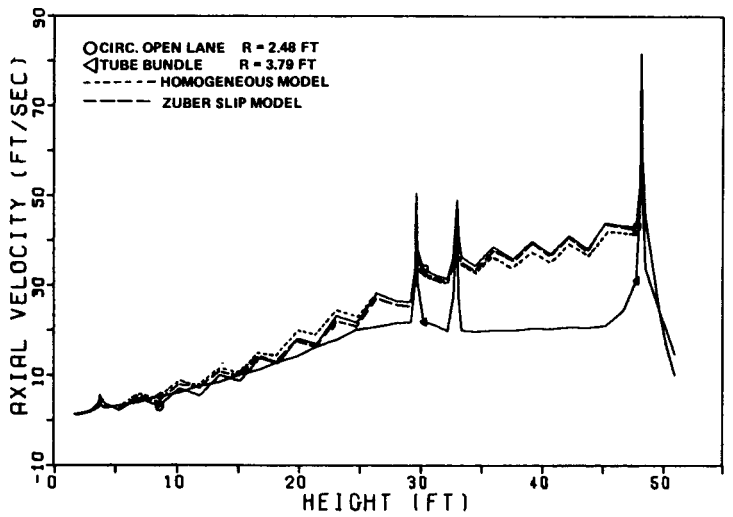

FIGURE 6.53 EFFECT OF CHANGES IN VOID FRACTION ON AXIAL VELOCITY PROFILES

Section 7

DISCUSSION

The results for the best estimate analysis and sensitivity study are discussed below.

7.1 BEST ESTIMATE ANALYSIS

The most significant result from the best estimate analysis is the variation in local thermal/hydraulic conditions caused by differences in geometrical features. Predicted steam quality in the TMI-2 open lane is significantly lower than quality in the bundle at the same elevation. As is shown in Figure 6.7, the low quality steam from the open lane is confined to a small fraction of the total cross-sectional area of the steam generator. Since the TMI-2 steam temperature is not much less than the DB-2 steam temperature, the effect of the open lane on overall performance appears small. The circumferential open lane was also found to have only a small effect on steam temperature.

The peripheral gap also has a significant effect on predicted local thermal/hydraulic conditions. With the peripheral gap open at the tube support plates in TMI-2, low quality steam reaches the upper portion of the steam generator. With all the peripheral gap openings blocked as in DB-2, the peripheral gap steam temperatures are greatly increased. The split ring appears effective for improving the thermal conditions in the peripheral gap.

Since the DB-2 manway lane is blocked at the tube support plates, the quality reductions in the manway lane are not nearly as large as the unblocked TMI-2 open lane quality reductions. Although the number of tubes that are missing from the DB-2 manway lane is nearly equal to the number missing from the TMI-2 open lane, the difference in quality between the manway lane and tube bundle is much smaller.

Since the center untubed region is mostly blocked, the difference in quality between the center untubed region and tube bundle is not large. The effect of center untubed region conditions on overall performance appears negligible since the cross-sectional area of the center untubed region is relatively small.

The differences in the predicted overall conditions presented in Table 6.2 can be explained in terms of the operating conditions and internal geometrical features used for each steam generator. First, the pressure drop for DB-2 is greater than for TMI-2 since there is an extra tube support plate in DB-2. The ratio of bleed flow rate to steam flow rate is higher for TMI-2 at all loads since the peripheral gap enthalpy at the bleed port elevation is less for TMI-2.

At low loads, the steam outlet temperature approaches the primary inlet temperature as shown in Figure 6.12. Since feedwater temperature and primary inlet temperature are specified as a functions of load, steam flow at each load can be computed by a secondary side heat balance. At 15% load, this steam flow is about 0.72×10^6 lbm/hr per steam generator for both TMI-2 and DB-2. However, the steam flows for the THEDA best estimate calculations (Table 2.1) were read from graphs in the functional specifications rather than computed from a heat balance. The values read from the graphs are 0.80×10^6 and 0.865×10^6 lbm/hr and appear to be in error. This is the source of the discrepancy between the nominal and computed heat transfer rates at 15% power as shown in Table 6.2. The agreement at 67% and 100% is quite good.

The DB-2 runs also showed a different trend in steam temperature versus load than the TMI-2 runs. As load increases, the TMI-2 outlet steam temperature reaches a peak at an intermediate power level (70% to 80%). Above that power level, the temperature decreases due to a decreasing superheated steam heat transfer region. The DB-2 steam temperature, however, continues to increase up to the 100% power level. This is due primarily to the tube support plate blockages in the DB-2 peripheral gap which increase the steam temperature.

7.2 SENSITIVITY STUDY

The use of a two-dimensional model to simulate the steam generator away from the open lane is verified by Figure 7.1. The quality profiles in the peripheral gap and tube bundle are in agreement for the 2-D nominal and 3-D TMI-2 run at $\theta = 180°$. The use of a two-dimensional circumferential open lane to determine the sensitivity of the TMI-2 radial open lane can be justified by the quality profiles in Figure 7.2. The axial quality profile at mid-radius in the radial lane is similar to the quality profile for the COL. Thus, incremental changes in COL conditions due to changes in empirical correlation and grid system should be similar to the average changes in the radial lane.

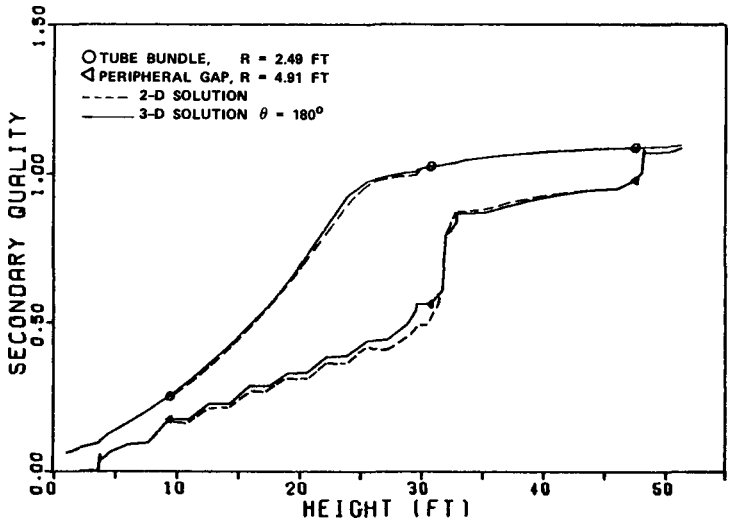

FIGURE 7.1 COMPARISON OF TMI-2 2-D SOLUTION AND 3-D SOLUTION QUALITY PROFILES

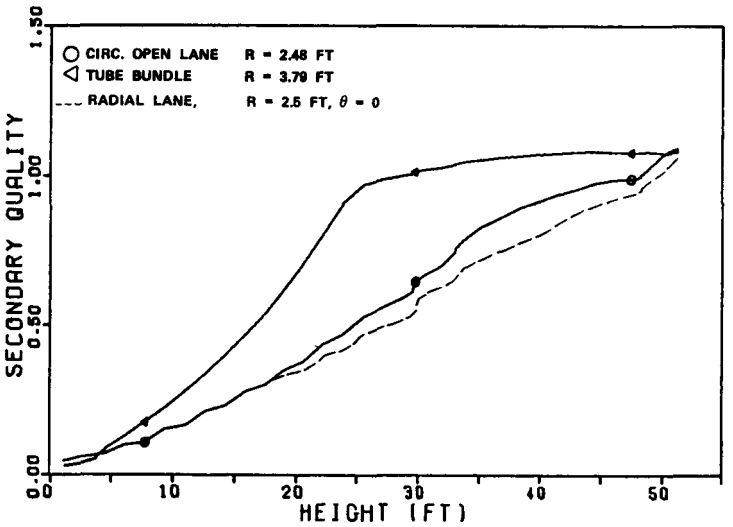

FIGURE 7.2 COMPARISON OF COL AND TMI-2 RADIAL OPEN LANE QUALITY PROFILES

The effect of changes in empirical correlations and grid system on steam generator performance can be broken up into two categories. Correlations in the first category influence the local conditions in untubed regions while not affecting the bundle conditions. The void fraction, mixing coefficient, and peripheral gap resistance belong in this group. The changes in void fraction correlation had the largest effect on local conditions within the peripheral gap and circumferential open lane.

Correlations in the second category affect tube bundle conditions as well as local conditions. They include the heat transfer coefficients for nucleate boiling and superheated steam, film dryout quality, cross-flow resistance, and tube support plate resistance. The heat transfer coefficients, film dryout quality, and tube support plate resistance produce one-dimensional perturbations. Conditions are changed in the axial direction with little change in the radial distribution. Cross-flow resistance, however, changes the radial distributions with small changes in the axial distributions.

Changes in the level of tube support plate modeling detail affect both the local conditions and bundle conditions (Figure B.22). As shown in Figure 6.48, changing to the FGSP model increases the quality in the peripheral gap compared to the RSP model. The FGSP model should model the support plate obstruction in the peripheral gap better than the RSP model. Therefore, it may be necessary to use the FGSP model in future analyses. However, the assumptions about area and porosity changes should be reviewed before the FGSP model is used extensively.

The primary side temperature distributions for the FGSP runs in Figures 6.46 and 6.51 require additional comment. These figures show a decrease in the primary temperature gradients on the upstream side of the FGSP nodes and an increase on the downstream side. These changes are not a result of local changes in heat flux. The heat flux would have to change by factors of one-half and two to account for the changes in temperature gradients. This was not found in the heat flux data. The gradients are actually a result of upwind differencing, the nonuniformity of the axial grid, and the method that was used to plot the temperature profiles. The non-uniformity of the grid is shown in Figure 7.3. For the main control volume that encloses point p, the finite-difference equation is obtained from Eq. 3.6 with upwind differencing as:

$$- G_t \left(\frac{h_{t,\,x+} - h_{t,\,p}}{\Delta x_p} \right) = \frac{4\, q_{t,\,p}}{d_t} \qquad (7.1)$$

where:

$h_{t,\,x+}$ = enthaly at main node x+

$h_{t,\,p}$ = enthalpy at main node p

$q_{t,\,p}$ = heat flux at main node p

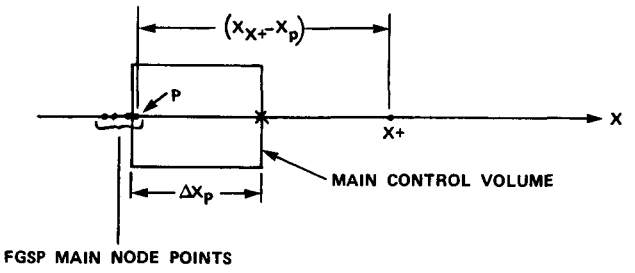

FIGURE 7.3 NONUNIFORMITY OF THE FGSP GRID SYSTEM

With the non-uniform grid, the distance Δx_p is less than the distance between points x+ and p shown in Figure 7.3. Since q_t does not change significantly from point x+ to point p, the apparent gradient in enthalpy between point x+ and point p will be less than the actual gradient by a factor of $\Delta x_p/(x_{x+} - x_p)$. The apparent gradient on the downstream side of the FGSP nodes is larger than the actual gradient by the inverse of this factor. With the enthalpies (or temperatures) plotted at the main node points as in Figures 6.46 and 6.51, the apparent gradients become evident. If, however, the enthalpies are plotted at the faces of the main control volumes, a smooth curve can be obtained. This is consistent with the upwind differencing assumptions which implies that the upwind value of enthalpy is transported to the face of the main control volume.

One of the objectives of the sensitivity study was to determine which correlations have a large effect on overall and local conditions. From the results, it is apparent that changing the void fraction correlation has a large and significant effect on the local conditions in both the peripheral gap and COL. Of those correlations that had an effect on local condition without affecting bundle conditions, void fraction gave the largest changes in local conditions. For the correlations that had a simultaneous effect on both bundle and local conditions, none of the correlations had a dominant effect. The Chen correlation has been excluded from this observation since the heat transfer appears unreasonably low compared to B&W proprietary test data. Thus, the total uncertainty in the overall conditions appear to be a combination of uncertainties from the nucleate boiling coefficient, the film dryout quality, and superheated steam heat transfer coefficient. In particular, the changes in these correlations gave steam outlet temperature changes that were of similar magnitude (1°F to 3°F).

The void fraction results indicate that several parameters not studied during this project could affect the local quality in untubed regions. Since it was found that the gap quality is determined by a balance of the tube bundle axial pressure gradient and the gravity load in the gap, anything that affects either of these parameters will also affect gap quality. Uncertainty in the two-phase flow pressure drop in the tube bundle is a likely source of uncertainty in gap quality. The analyses of this project used the same void fraction correlation for the tube bundle and the untubed regions. It is possible that the relationship between void fraction and quality in the open regions is different than in the tube bundle which would also affect gap quality.

Section 8

CONCLUSIONS

8.1 GENERAL

- THEDA-1 predicts physically realistic and internally consistent trends of both overall and local steam conditions.
- The cross-section averaged secondary side enthalpy is relatively unaffected by either the uncertainty in empirical correlations or the number of grid points.
- In untubed regions such as the gap between the bundle and the shroud and the inspection lane, the secondary flow and enthalpy are significantly affected by correlation uncertainties and by the detail used to model the tube support plates.

8.2 BEST ESTIMATE ANALYSIS

Although there is some uncertainty in the best estimate predictions, the following conclusions can be reached about the performance of the TMI-2 and DB-2 OTSGs:

- At the mean bundle radius, the predicted axial gradients of primary and secondary side pressure, enthalpy, and flow are consistent with the results from one-dimensional analyses. Except near untubed regions and at the inlet and outlet, gradients in the radial and circumferential directions are much smaller than axial gradients.
- The outlet steam temperature predicted by THEDA-1 equals or exceeds the maximum expected value as obtained from the TMI-2 and DB-2 functional specifications.
- At a given elevation, the secondary side enthalpy in untubed regions of the steam generator is less than the bundle enthalpy. The enthalpy difference is less for DB-2 than for TMI-2 because the DB-2 tube support plates totally block the flow in the untubed regions while the TMI-2 support plates do not.

- The average enthalpy of the steam bleed flow is significantly lower than the bundle average enthalpy at the bleed point elevation because the majority of the bleed flow comes from the untubed peripheral gap. Thus, more bleed flow is required to heat the feedwater to saturation than would be indicated by one-dimensional analysis. The bleed flow for DB-2 is less than for TMI-2 because the DB-2 tube support plates block the flow in the peripheral gap.
- The enthalpy in the open lane around the DB-2 manway cover is relatively close to the bundle enthalpy because of the flow blockages at each tube support plate.
- At 15 percent load, the secondary side fluid reaches superheat as it flows across the face of the lower tubesheet.

8.3 EFFECT OF CORRELATION UNCERTAINTIES ON TMI-2 PERFORMANCE PREDICTIONS

The reader should note that the conclusions presented in this section (8.3) and Sections 8.4 and 8.5 result from sensitivity studies based on the TMI-2 steam generator that has unblocked gaps between the tube support plate and the shroud. No sensitivity studies were carried out for the DB-2 steam generator geometry where these gaps are blocked to flow. The conclusions reached regarding uncertainties in steam conditions in untubed regions of the steam generator should not be applied to an OTSG with flow blockages at each support plate.

- THEDA-1 predicts realistic effects of correlation perturbations. Both the direction and magnitude of the predicted perturbations in steam conditions are consistent with the direction and magnitude of the input perturbations.
- Uncertainties in empirical correlations have effects which can generally be grouped in two categories: those which primarily affect the axial variation of steam conditions, and those which primarily affect the radial and circumferential variation. The axial variations can be estimated with a one-dimensional analysis; however, a multi-dimensional analysis such as THEDA-1 must be used to estimate the uncertainty in steam conditions resulting from correlations affecting radial and circumferential variations.

- In general, uncertainties affecting the heat transfer rate between the primary and secondary side have a one-dimensional effect on local and overall performance. The uncertainty in either local or outlet steam conditions caused by uncertainties in heat transfer relationships is relatively small.

- Uncertainty in the tube bundle cross-flow resistance affects the radial variation of enthalpy at the steam generator inlet and this effect persists along the length of the steam generator.

- Uncertainty in the void fraction correlation has a significant effect on both the axial and cross-stream variation of secondary side conditions. The void fraction correlation directly affects the buoyancy term in the axial momentum equation. Algebraic slip models result in larger densities than the homogeneous model. Compared to the homogeneous model, algebraic slip models produce larger cross-flows in and out of the untubed regions and also reduce the average axial flow. Both of these effects increase the enthalpy in untubed regions.

8.4 EFFECT OF GRID SPACING ON TMI-2 STEAM CONDITIONS

- Within the range studied, grid spacing has little effect on predicted bundle average steam generator performance.

- When only the axial resistance of the tube support plate is modeled and the axial resistance of a total flow blockage is averaged over a larger area (regular tube support plate model), two axial nodes per support plate are adequate. About five radial nodes per foot are sufficient to model the gradients in the peripheral gap of the steam generator. Fewer radial nodes are acceptable in the middle of the bundle. The radial spacing of nodes near the center of the steam generator, however, must be smaller than at the periphery. Grid spacing requirements for the fine grid support plate model were not established during this study.

8.5 FLOW BLOCKAGE MODEL

- Local flow conditions in untubed regions predicted with the fine grid support plate model sometimes agreed with and differed from those predicted with the regular support plate model. The cause of this inconsistency could not be determined.

8.6 CIRCUMFERENTIAL OPEN LANE MODEL FOR TMI-2

- A comparison of the results from the 2-D circumferential open lane run and the 3-D best estimate run indicates that the circumferential open lane model provides realistic estimates of conditions at the mid-radius of a radial open lane. The 2-D model provides a practical means for a detailed study of the effect of flow blockages on open lane conditions.
- The void fraction model affects open lane conditions in a manner similar to its effect on peripheral gap conditions; the higher density given by the algebraic slip model produces a greater enthalpy in the lane than does the homogeneous model.

Section 9

RECOMMENDATIONS

9.1 GENERAL

- Although THEDA-1 has been shown to provide reasonable predictions of the trends in local and overall thermal/hydraulic conditions, variations in modeling detail and correlation uncertainties can affect accuracy. THEDA-1 predictions should be verified by comparison with experimental data.
- Until a comparison with data is available, the results of this study can be used as an aid in determining the modeling detail required for a particular application. This study can also be used to estimate the inaccuracies that are expected to result from uncertainties in empirical correlations.
- This study indicates that additional work in several areas would improve the accuracy and efficiency of OTSG thermal/hydraulic analyses:

  Code Development
  Refined Two-Phase Flow Model
  Tube Support Plate Modeling
  Sensitivity Studies

9.2 CODE DEVELOPMENT

- Significant detail is required to model flow blockages at the tube support plate. The number of nodes necessary for a 3-D analysis of an OTSG, considering flow blockages at all tube support plates, exceeds the in-core storage capability of the CDC 7600 computer. Therefore, secondary storage capability should be added to the THEDA-1 code.
- Two-dimensional models of the OTSG are adequate in many cases, particularly when the 2-D circumferential open lane

model is used. THEDA-1 requires a minimum of four circumferential nodes even for an axi-symmetric application.

In order to reduce computer cost and storage requirements, the capability for a true two-dimensional analysis should be added to THEDA-1.

- THEDA-1 does not accurately model large changes of flow area or porosity such as occur at a tube support plate or between tubed and untubed regions of the steam generator. A more accurate model should be added to THEDA-1.

- In many cases, the cost and storage requirements for providing detailed local condition predictions in an untubed region or at a tube support plate could be reduced by providing THEDA-1 with a spotlighting capability. A small region of the steam generator could be modeled in detail with the boundary conditions for the local region provided from a coarser grid model of the entire steam generator.

- Because of the continuative outflow boundary condition, THEDA-1 does not accurately model the flow distribution at the exit of the bundle. This deficiency does not affect either overall performance predictions or local condition predictions at other locations because little heat transfer takes place in the affected region. However, the local cross-flow velocities at the tube bundle exit are inaccurate and cannot be used in a flow-induced vibration analysis. The THEDA-1 analysis should be extended to include the steam annulus region eliminating the limitation imposed by the present boundary condition.

9.3 REFINED TWO-PHASE FLOW MODEL

- The velocity and enthalpy distributions in untubed regions of the steam generator were found to be significantly affected by the assumed degree of slip between the liquid and vapor phases when using the THEDA-1 algebraic slip model for two-phase flow. Comparable runs should be performed with a separated flow model to determine if steam conditions in the untubed regions are affected when the slip between phases is allowed to vary in all three directions as opposed to being assumed constant as is the case with THEDA-1.

- Low load performance should also be calculated with a separated flow model since the buoyancy effects are dominant and might affect velocity and enthalpy distributions in the tube bundle.
- Since conditions in the untubed regions of the OTSG are significantly dependent on the void fraction model, experimental data will be required to verify the two-phase flow models used in the analysis.

9.4 TUBE SUPPORT PLATE MODELING

- Steam conditions in the untubed region of the OTSG are significantly affected by the amount of flow blockage at the tube support plates and how the blockage is modeled. Experimental data should be obtained for both the peripheral gap region and the untubed lane to verify the blockage models used in THEDA-1.

9.5 SENSITIVITY STUDIES

- The grid spacing sensitivity runs for this study were made with the regular tube support plate model. The grid spacing requirements for the fine grid tube support plate model should be established after an accurate model for porosity and area changes is added. The radial grid spacing requirements should also be determined both for the regular support plate model and the fine grid tube support plate model.
- The circumferential open lane model could be used to establish grid spacing requirements perpendicular to the open lane.
- Sensitivity studies, similar to the one reported herein, should be conducted for a steam generator with flow blockages at the gaps between the tube support plates and the shroud.

Section 10

REFERENCES

1. S. V. Patankar and D. B. Spalding, "A Calculation Procedure for Heat, Mass, and Momentum Transfer in Three-Dimensional Parabolic Flow", Int. Journal of Heat and Mass Transfer, Vol. 15, 1972, pp. 1787-1806.

2. S. V. Patankar and D. B. Spalding, "A Calculation Procedure for the Transient and Steady-State Behavior of Shell-and-Tube Heat Exchangers", Imperial College, Mechanical Engineering Dept., Report EF/TN/A/48, July, 1972.

3. S. V. Patankar, "The Numerical Prediction of Three-Dimensional Flows", Studies in Convection : Theory and Applications, Academic Press, London, 1975.

4. R. T. Lahey and F. J. Moody, The Thermal/Hydraulics of a Boiling Water Nuclear Reactor, American Nuclear Society, 1977.

5. S. L. Smith, "Void Fractions in Two-Phase Flow: A Correlation Based on an Equal Velocity Head Model", Proc. Inst. Mech. Engrs., Vol. 184, Pt. 1, No. 36, 1969-1970.

6. J.R.S. Thom, "Prediction of Pressure Drop During Forced Circulation Boiling of Water", Int. Journal Heat Mass Transfer, Vol. 7, 1964, pp. 709-724.

7. N. Zuber, et al., "Steady-State and Transient Void Fraction in Two-Phase Flow Systems", Final Report for the Program of Two-Phase Flow Investigation, EURAEC, GEAP-5417, January, 1967.

8. "Heat Transfer in Rod Bundles", Symposium on Heat Transfer in Rod Bundles, Winter Annual Meeting of ASME, New York, December 3, 1968.

9. D. L. Katz and J. G. Knudsen, Fluid Dynamics and Heat Transfer, New York, McGraw-Hill, 1958, p. 176.

10. I. E. Idelchik, Handbook of Hydraulic Resistance, AEC-tr-6630, 1966.

11. M. Jakob, Trans. ASME, 60, 1938, pp. 384-386.

12. W. M. Kays, Convective Heat and Mass Transfer, New York, McGraw-Hill, 1966, p. 173.

13. J. C. Chen, "A Correlation for Boiling Heat Transfer to Saturated Fluids in Convective Flow", ASME Paper 63-HT-34, 1963.

Appendix A

MAIN NODE LOCATIONS AND TUBE SUPPORT PLATE LOCATIONS

Appendix A

MAIN NODE LOCATIONS AND TUBE SUPPORT PLATE LOCATIONS

TABLE A.1

BEST ESTIMATE ANALYSIS – AXIAL NODES

Node Number	Height (ft)		Node Number	Height (ft)	
	TMI-2	DB-2		TMI-2	DB-2
1	0**	*	29	31.818	31.777
2	1.198	*	30	32.151	32.193
3	2.396	*	31	32.484	32.609
4	3.729	*	32	32.979	*
5	3.771	*	33	33.021	*
6	3.896	*	34	33.146	*
7	3.938	*	35	33.188	*
8	4.654	*	36	33.771	*
9	6.198	*	37	35.313	*
10	7.802	*	38	36.854	*
11	9.427	*	39	38.469	*
12	11.073	*	40	40.031	*
13	12.760	*	41	41.573	41.614
14	14.406	*	42	43.094	43.052
15	16.042	*	43	44.594	44.354
16	17.625	*	44	46.073	45.646
17	19.125	*	45	47.531	46.934
18	20.708	*	46	48.146	48.066
19	22.344	*	47	48.188	49.023
20	23.990	*	48	48.313	49.427
21	25.677	*	49	48.354	49.469
22	27.323	*	50	48.926	49.594
23	28.938	*	51	49.498	49.636
24	29.646	*	52	50.070	50.139
25	29.688	*	53	50.642	*
26	29.8125	*	54	51.40	*
27	29.854	*	55	52.115	*
28	30.836	*			

*Same as TMI-2 value
**Lower tubesheet face

TABLE A.2

TUBE SUPPORT PLATE HEIGHTS*

TSP Number	Height (ft)	
	TMI-2	DB-2
1	3.833	**
2	7.000	**
3	10.25	**
4	13.583	**
5	16.833	**
6	19.917	**
7	23.167	**
8	26.50	**
9	29.75	**
10	33.083	**
11	36.083	**
12	39.25	**
13	42.333	**
14	45.333	45.0
15	48.25	47.5
16	--	49.531

*Distance from lower tubesheet face to the tube support plate mid-point

**Same as TMI-2 value

TABLE A.3

SENSITIVITY STUDY AXIAL NODES –
NOMINAL AND 115 AXIAL NODE CASES

Node Number	Nominal Nodes (ft)	Added Nodes (ft)	Node Number	Nominal Nodes (ft)	Added Nodes (ft)	Node Number	Nominal Nodes (ft)	Added Nodes (ft)
1	0		40	19.125		79		36.340
2		0.599	41		19.653	80	36.854	
3	1.198		42		20.180	81		37.392
4		1.797	43	20.708		82		37.931
5	2.396		44		21.253	83	38.469	
6		2.840	45		21.799	84		38.990
7		3.287	46	22.344		85		39.510
8	3.729		47		22.893	86	40.031	
9	3.771		48		23.441	87		40.545
10	3.896		49	23.990		88		41.059
11	3.9375		50		24.552	89	41.573	
12		4.296	51		25.115	90		42.080
13	4.654		52	25.677		91		42.587
14		5.169	53		26.226	92	43.094	
15		5.683	54		26.774	93		43.594
16	6.198		55	27.323		94		44.094
17		6.733	56		27.861	95	44.594	
18		7.267	57		28.399	96		45.087
19	7.802		58	28.9375		97		45.580
20		8.344	59		29.292	98	46.073	
21		8.885	60	29.646		99		46.559
22	9.427		61	29.6875		100		47.045
23		9.976	62	29.8125		101	47.531	
24		10.524	63	29.854		102		47.839
25	11.073		64		30.345	103	48.146	
26		11.635	65	30.836		104	48.1875	
27		12.198	66		31.327	105	48.3125	
28	12.760		67	31.818		106	48.354	
29		13.309	68	32.151		107		48.640
30		13.857	69	32.484		108	48.926	
31	14.406		70	33.021		109		49.212
32		14.951	71	33.146		110	49.498	
33		15.497	72	33.1875		111		49.784
34	16.042		73		33.479	112	50.070	
35		16.570	74	33.771		113	50.642	
36		17.097	75		34.285	114	51.40	
37	17.625		76		34.799	115	52.115	
38		18.125	77	35.3125				
39		18.625	78		35.826			

TABLE A.4

SENSITIVITY STUDY AXIAL NODES – 41 AXIAL NODE CASE

Node Number	Height (ft)
1	0
2	1.198
3	2.396
4	3.729
5	3.771
6	3.896
7	3.9375
8	5.4166
9	8.625
10	11.917
11	15.208
12	18.375
13	21.542
14	24.833
15	28.125
16	29.646
17	29.6875
18	29.8125
19	29.854
20	30.836
21	31.818
22	32.151
23	32.484
24	33.021
25	33.146
26	33.1875
27	34.583
28	37.667
29	40.792
30	43.833
31	46.792
32	48.146
33	48.1875
34	48.3125
35	48.354
36	48.926
37	49.498
38	50.070
39	50.642
40	51.40
41	52.115

TABLE A.5

SENSITIVITY STUDY AXIAL NODES – 99 NODE WITH 15 FGSP MODELS

Node Number	Height (ft)	Node Number	Height (ft)	Node Number	Height (ft)
1	0	34	19.812	67	36.021
2	1.198	35	19.854	68	36.146
3	2.396	36	19.979	69	36.187
4	3.729	37	20.021	70	36.854
5	3.771	38	20.708	71	38.469
6	3.896	39	22.334	72	39.146
7	3.938	40	23.063	73	39.188
8	4.654	41	23.104	74	39.313
9	6.198	42	23.229	75	39.354
10	6.896	43	23.271	76	40.031
11	6.938	44	23.99	77	41.573
12	7.063	45	25.677	78	42.229
13	7.104	46	26.396	79	42.271
14	7.802	47	26.438	80	42.396
15	9.427	48	26.563	81	42.437
16	10.146	49	26.604	82	43.094
17	10.188	50	27.323	83	44.594
18	10.313	51	28.938	84	45.229
19	10.354	52	29.646	85	45.271
20	11.073	53	29.688	86	45.396
21	12.76	54	29.813	87	45.438
22	13.479	55	29.854	88	46.073
23	13.521	56	30.836	89	47.531
24	13.646	57	31.818	90	48.146
25	13.708	58	32.151	91	48.188
26	14.406	59	32.484	92	48.313
27	16.042	60	32.979	93	48.354
28	16.729	61	33.021	94	48.926
29	16.771	62	33.146	95	49.498
30	16.896	63	33.188	96	50.07
31	16.938	64	33.771	97	50.642
32	17.625	65	35.313	98	51.40
33	19.125	66	35.979	99	52.115

TABLE A.6

BEST ESTIMATE ANALYSIS RADIAL NODES

Node Number	Radius (ft)	
	TMI-2	DB-2*
1	0.0	0.0
2	0.2	0.2
3	0.3	0.3
4	1.397	1.397
5	2.494	2.494
6	3.110	3.110
7	3.873	3.176
8	4.255	3.241
9	4.636	3.873
10	4.876	4.505
11	4.914	4.570
12	4.932	4.636
13	--	4.876
14	--	4.914
15	--	4.932

*Also used for the 2-D Sensitivity Study

TABLE A.7

BEST ESTIMATE ANALYSIS AND SENSITIVITY STUDY CIRCUMFERENTIAL NODES

Node Number	Angle (°)		
	TMI-2	DB-2	Sensitivity Study
1	0.0	0.0	0.0
2	0.301	4.5472	60.0
3	0.592	9.0943	120.0
4	1.108	9.9057	180.0
5	3.910	10.717	
6	15.0	15.0	
7	47.5	47.5	
8	82.5	82.5	
9	117.5	117.5	
10	150.0	150.0	
11	180.0	180.0	

TABLE A.8

SENSITIVITY STUDY RADIAL NODES* – 11, 21, AND COL RADIAL NODES

Node Number	Radius (ft)		
	11 Radial	21 Radial	COL
1	0.0	0.0	0.0
2	0.2	0.1	0.2
3	0.3	0.2	0.3
4	1.397	0.3	1.144
5	2.494	0.4	1.988
6	3.873	0.6	2.4103
7	4.570	0.866	2.4474
8	4.636	1.397	2.4846
9	4.876	1.946	2.5217
10	4.914	2.494	2.944
11	4.932	3.184	3.79
12	--	3.873	4.636
13	--	4.200	4.876
14	--	4.447	4.914
15	--	4.570	4.932
16	--	4.636	--
17	--	4.716	--
18	--	4.796	--
19	--	4.876	--
20	--	4.914	--
21	--	4.932	--

*Nominal 2-D Sensitivity Study radial nodes are given in Table A.6

Appendix B

SENSITIVITY STUDY QUALITY CONTOURS AND THE NOMINAL MASS VELOCITY VECTOR PLOT

Appendix B

SENSITIVITY STUDY QUALITY CONTOURS AND THE
NOMINAL MASS VELOCITY VECTOR PLOT

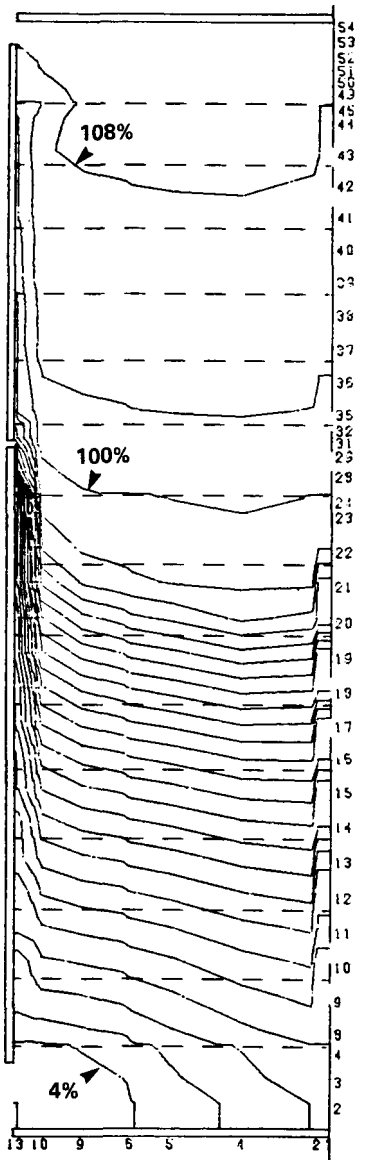

FIGURE B.1 NOMINAL RUN,
QUALITY CONTOUR
(4% QUALITY INCREMENTS)

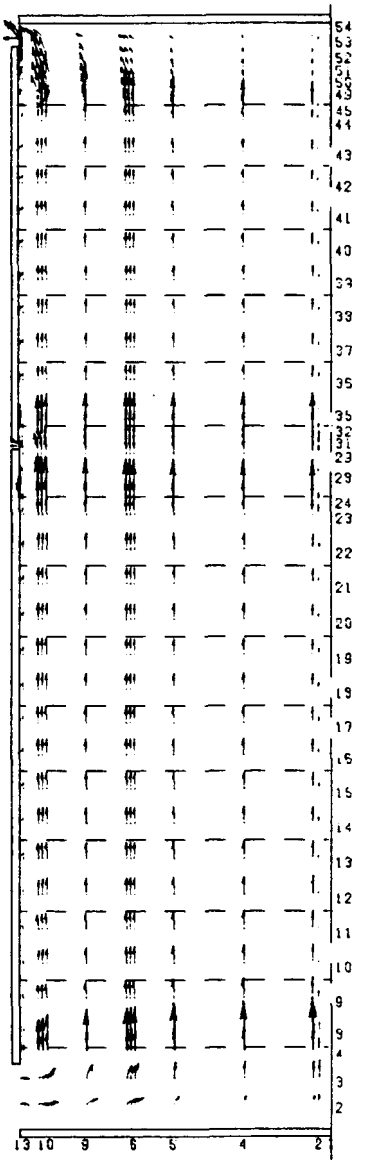

FIGURE B.2A NOMINAL RUN,
MASS VELOCITY

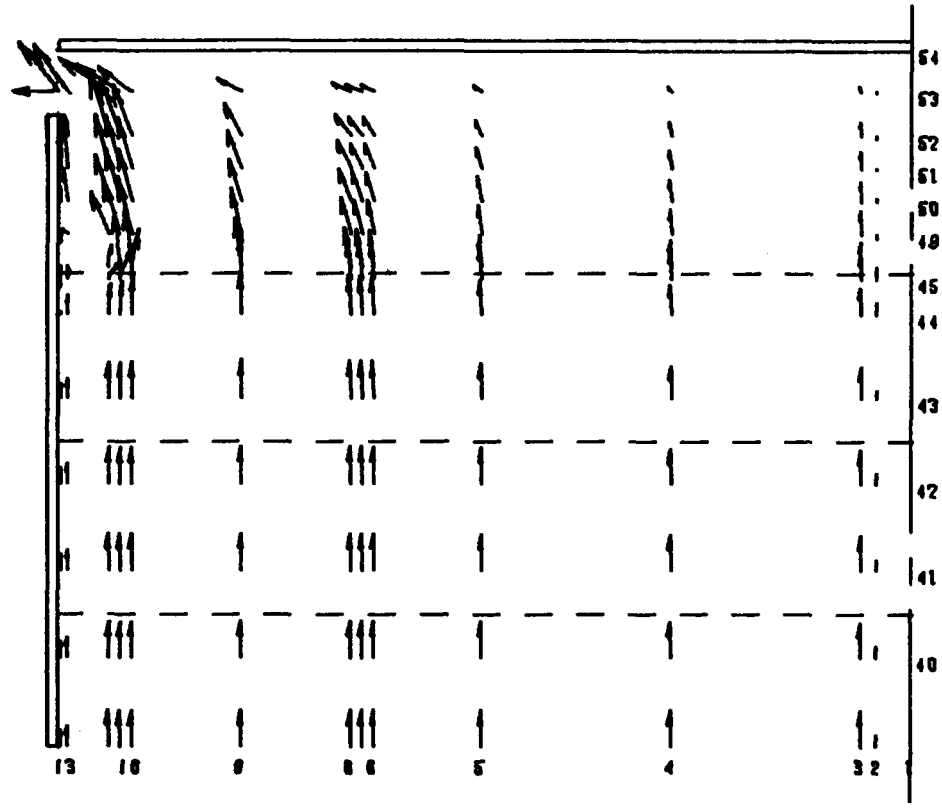

FIGURE B.2B NOMINAL RUN MASS VELOCITY ENLARGED
NEAR THE STEAM OUTLET REGION
(VECTORS ORIGINATE AT THE MAIN NODE POINTS)

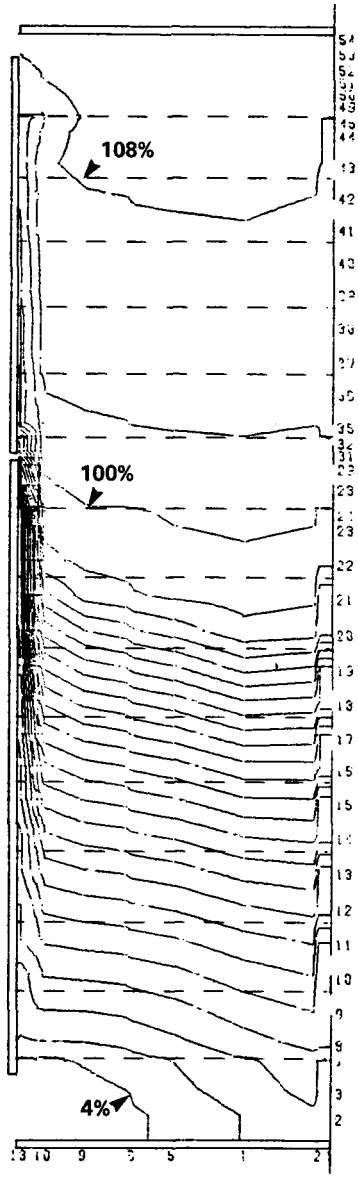

FIGURE B.3 THOM SLIP MODEL
(4% QUALITY INCREMENTS)

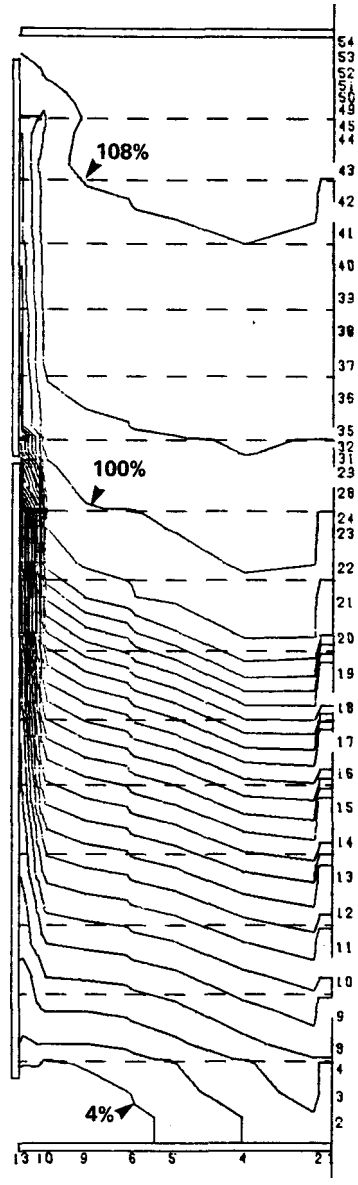

FIGURE B.4 HOMOGENEOUS MODEL
(4% QUALITY INCREMENTS)

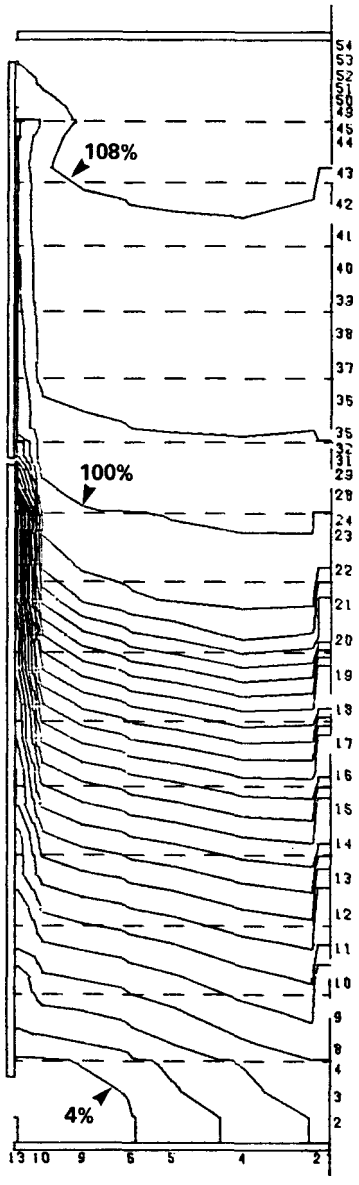

FIGURE B.5 TURBULENT MIXING
TIMES 0.2
(4% QUALITY INCREMENTS)

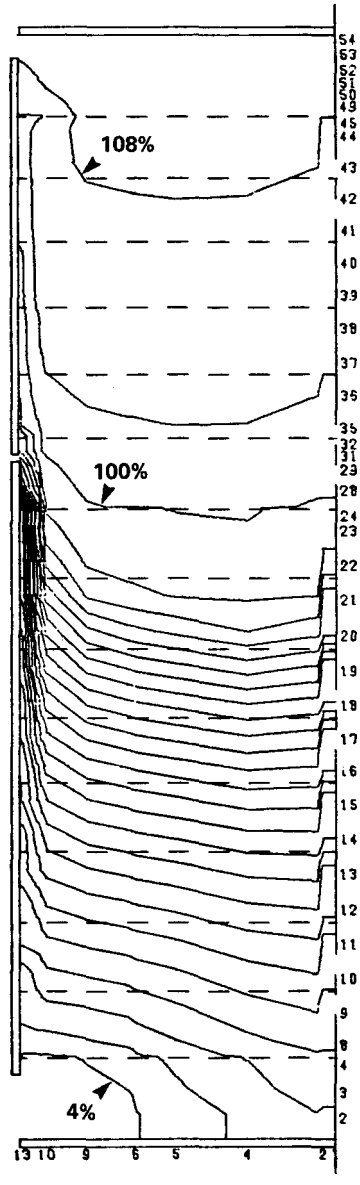

FIGURE B.6 TURBULENT MIXING
TIMES 5
(4% QUALITY INCREMENTS)

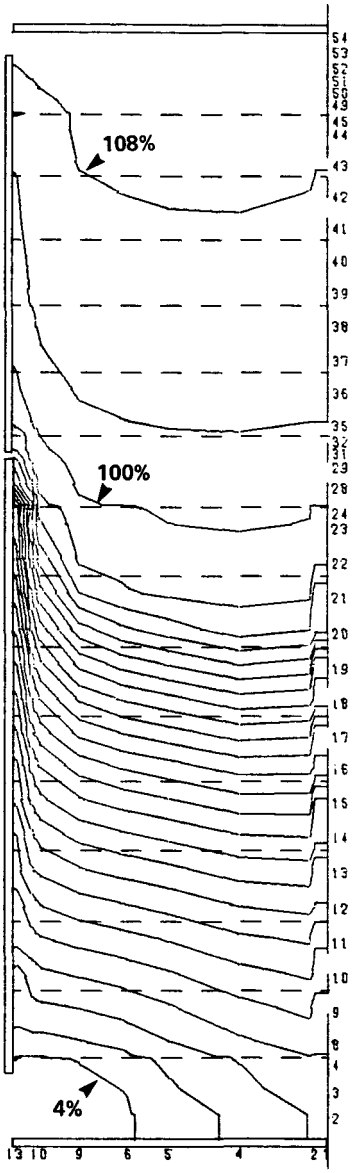

FIGURE B.7 MIXING COEFFICIENT
TIMES 15
(4% QUALITY INCREMENTS)

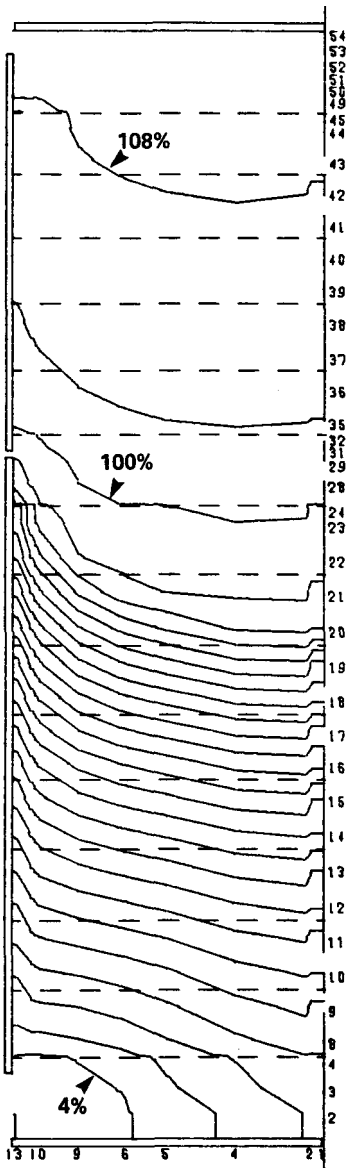

FIGURE B.8 MIXING COEFFICIENT
TIMES 50
(4% QUALITY INCREMENTS)

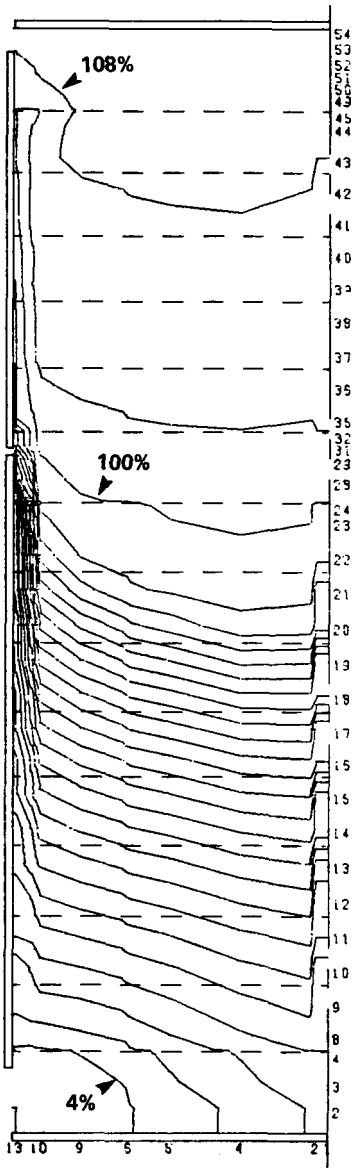

FIGURE B.9 TSP RESISTANCE
TIMES 0.75
(4% QUALITY INCREMENTS)

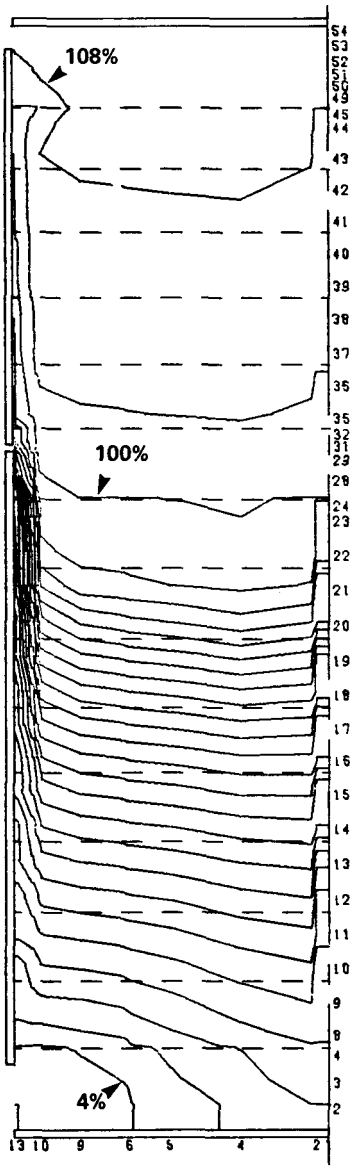

FIGURE B.10 TSP AXIAL RESISTANCE
TIMES 1.25
(4% QUALITY INCREMENTS)

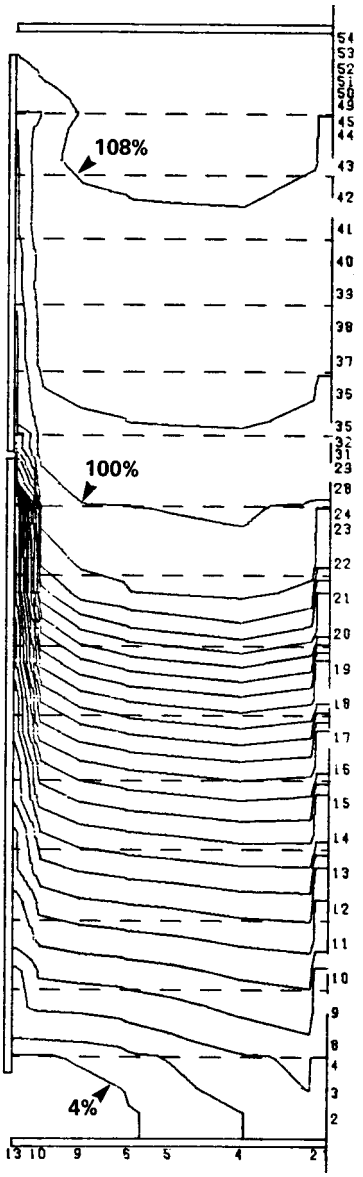

FIGURE B.11 CROSS-FLOW RESISTANCE TIMES 0.5 (4% QUALITY INCREMENTS)

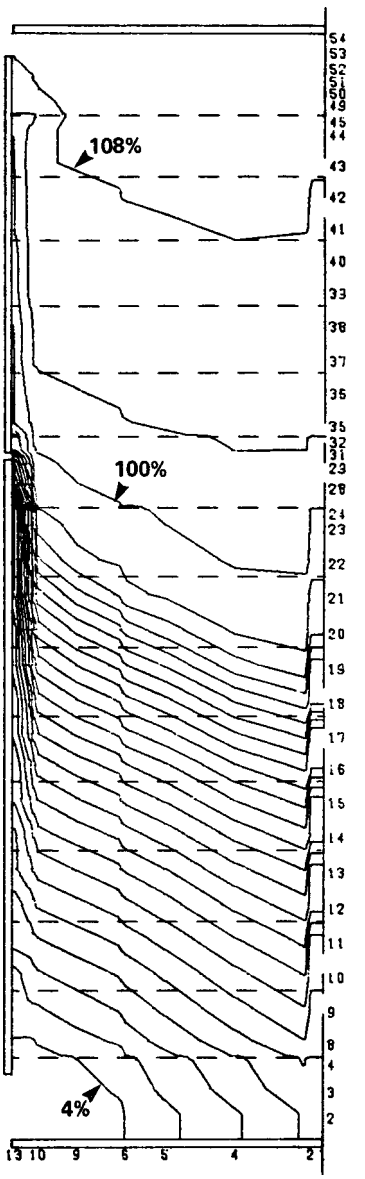

FIGURE B.12 CROSS-FLOW RESISTANCE TIMES 3.0 (4% QUALITY INCREMENTS)

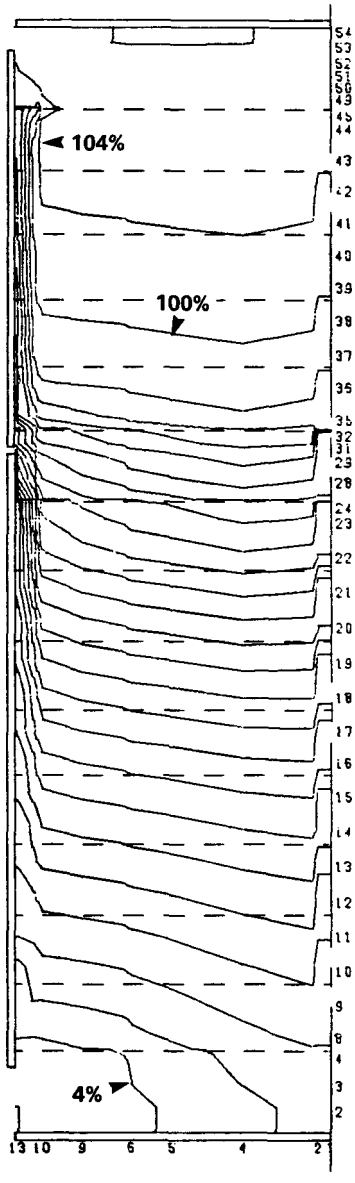

FIGURE B.13 CHEN NUCLEATE BOILING COEFFICIENT
(4% QUALITY INCREMENTS)

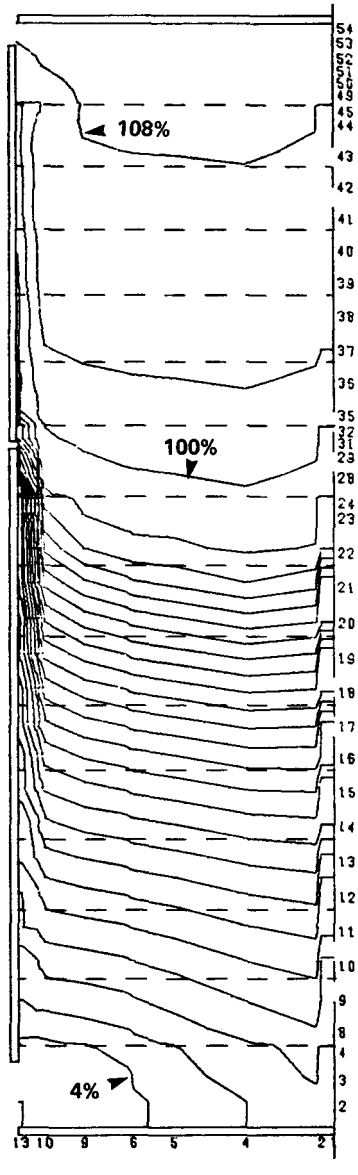

FIGURE B.14 NUCLEATE BOILING COEFFICIENT TIMES 0.5
(4% QUALITY INCREMENTS)

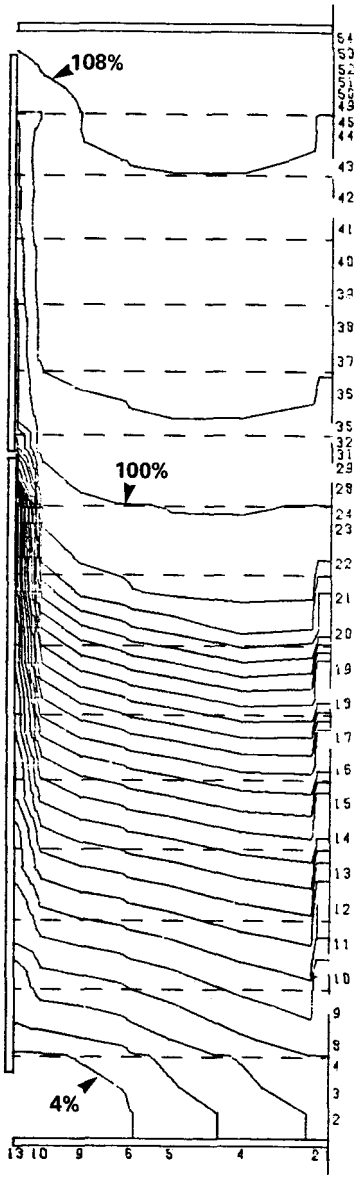

FIGURE B.15 SUPERHEATED STEAM COEFFICIENT TIMES 0.9 (4% QUALITY INCREMENTS)

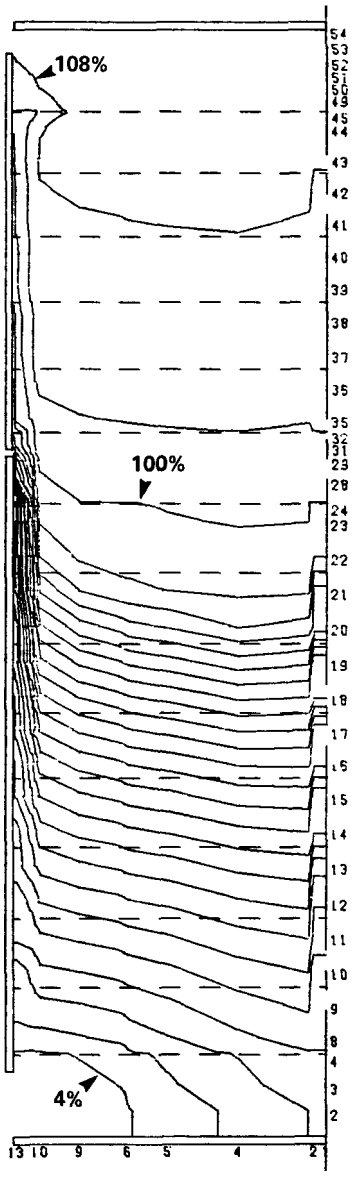

FIGURE B.16 SUPERHEATED STEAM COEFFICIENT TIMES 1.10 (4% QUALITY INCREMENTS)

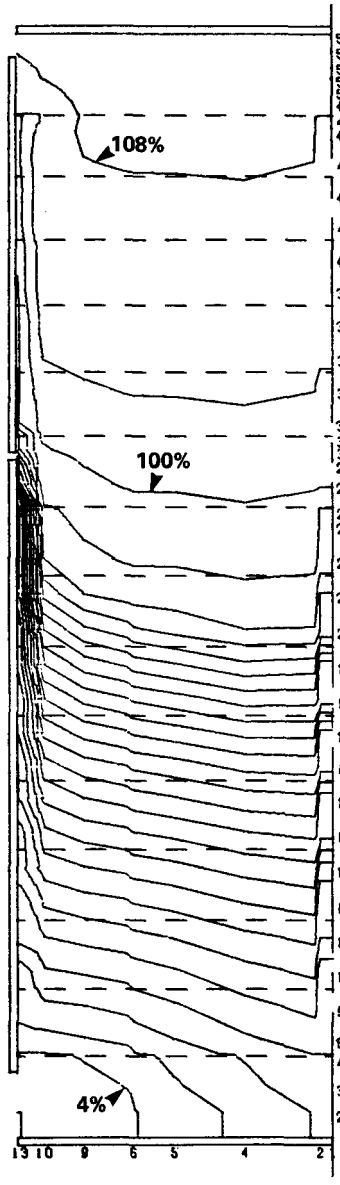

FIGURE B.17 DNB QUALITY = 0.92
(4% QUALITY INCREMENTS)

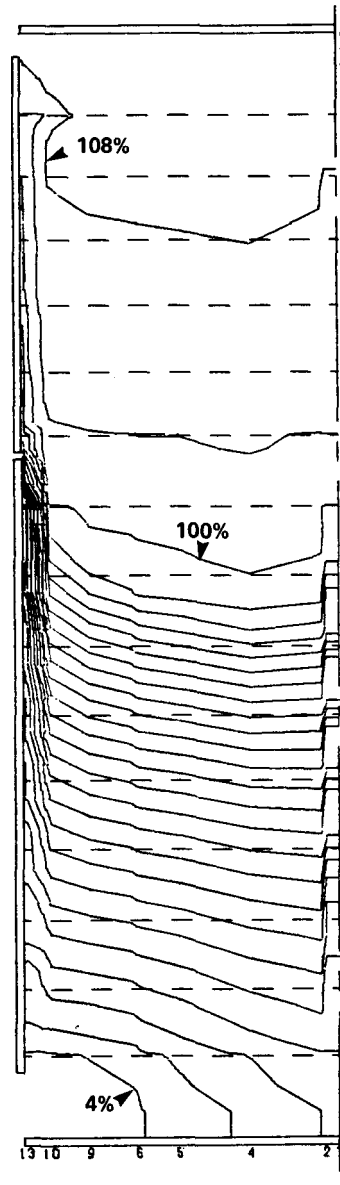

FIGURE B.18 DNB QUALITY = 0.98
(4% QUALITY INCREMENTS)

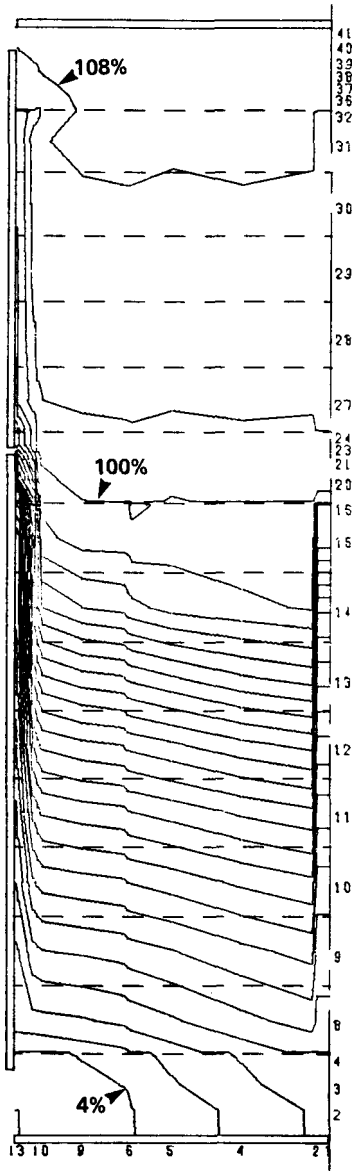

FIGURE B.19 41 AXIAL NODES
(4% QUALITY INCREMENTS)

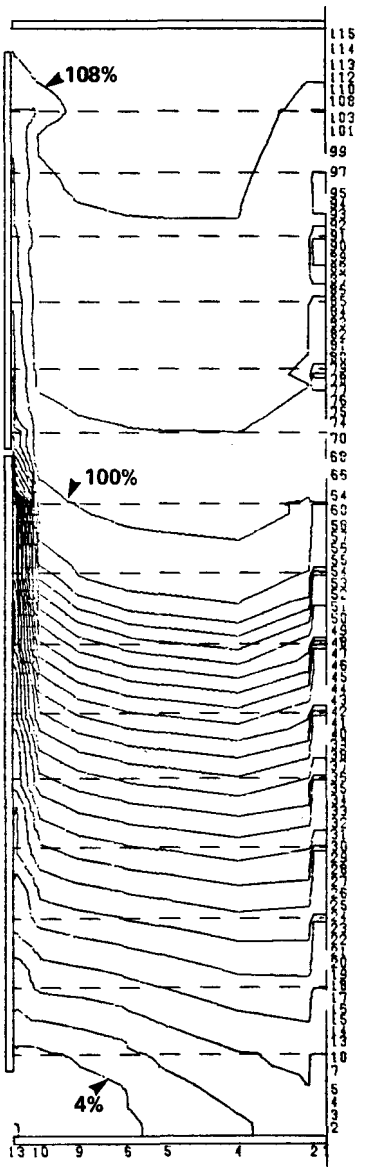

FIGURE B.20 115 AXIAL NODES
(4% QUALITY INCREMENTS)

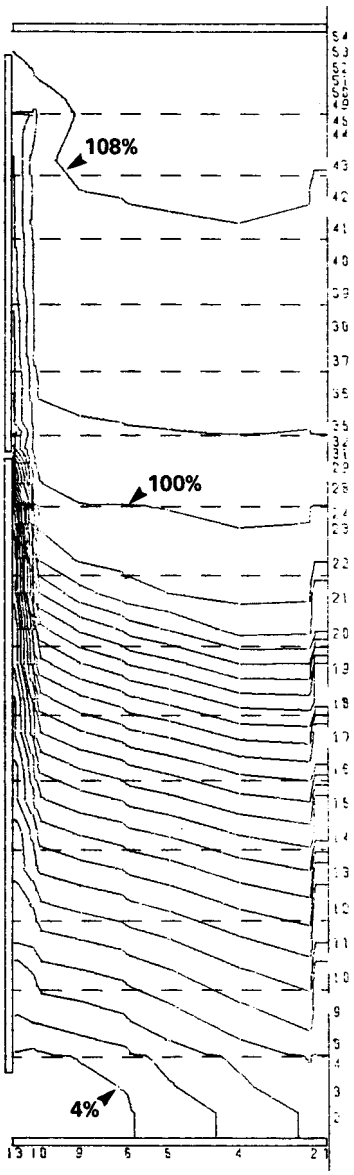

FIGURE B.21 NOMINAL RUN CORRECTED TSP POROSITIES (4% QUALITY INCREMENTS)

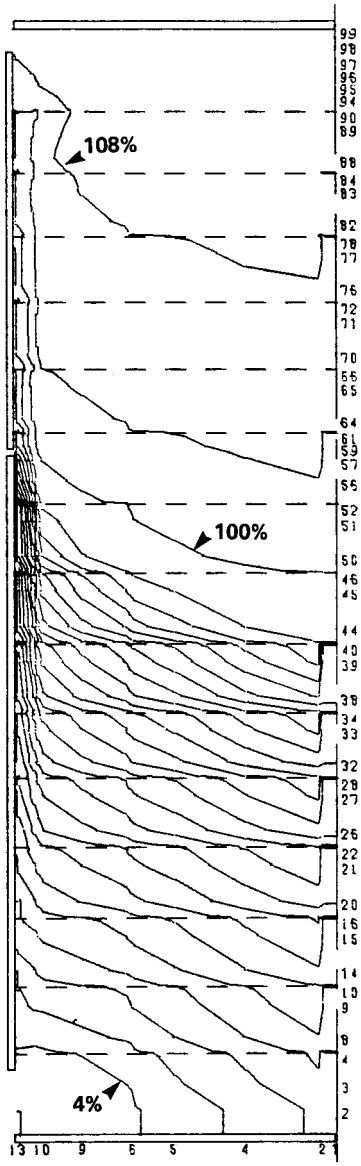

FIGURE B.22 CORRECTED TSP POROSITY MODEL WITH 99 AXIAL NODES (4% QUALITY INCREMENTS)

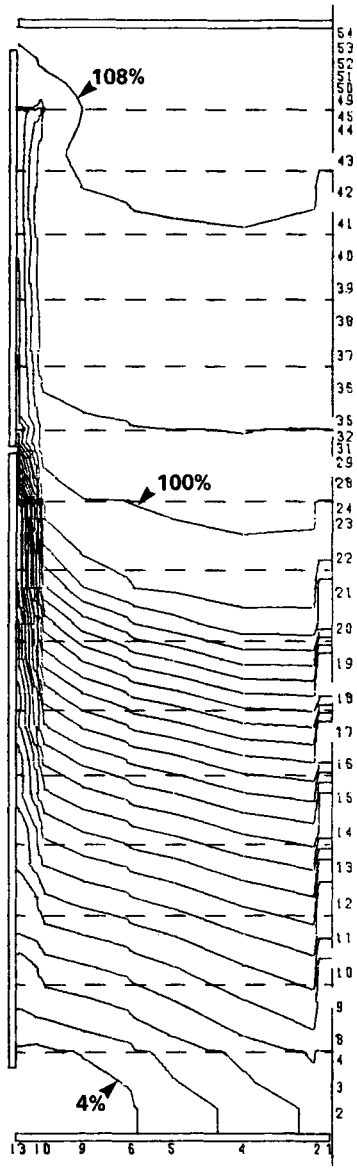

FIGURE B.23 PERIPHERAL GAP RESISTANCE -50% (4% QUALITY INCREMENTS)

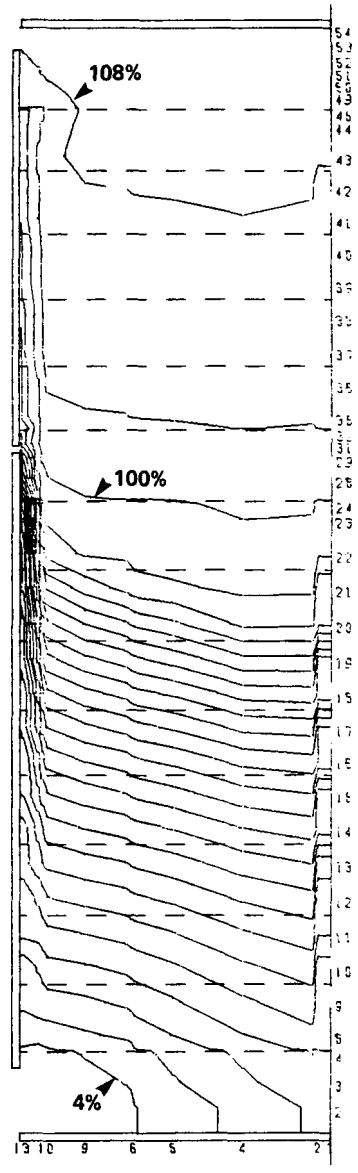

FIGURE B.24 PERIPHERAL GAP RESISTANCE +50% (4% QUALITY INCREMENTS)

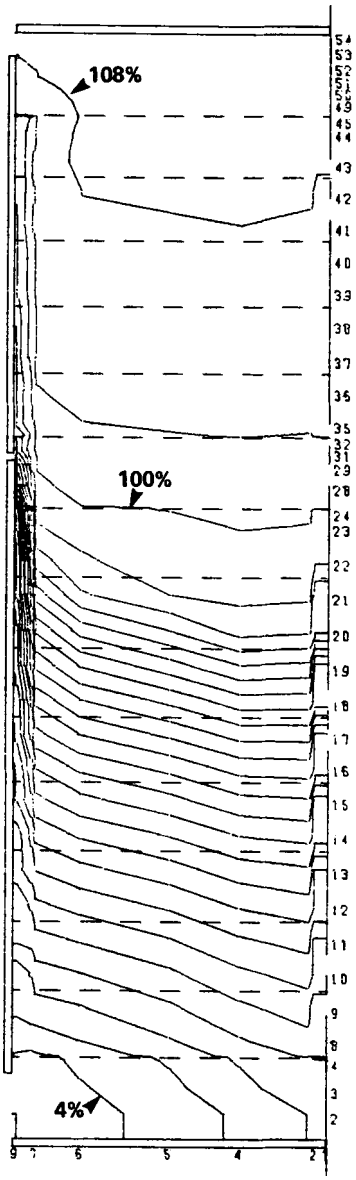

FIGURE B.25 11 RADIAL NODES
(4% QUALITY INCREMENTS)

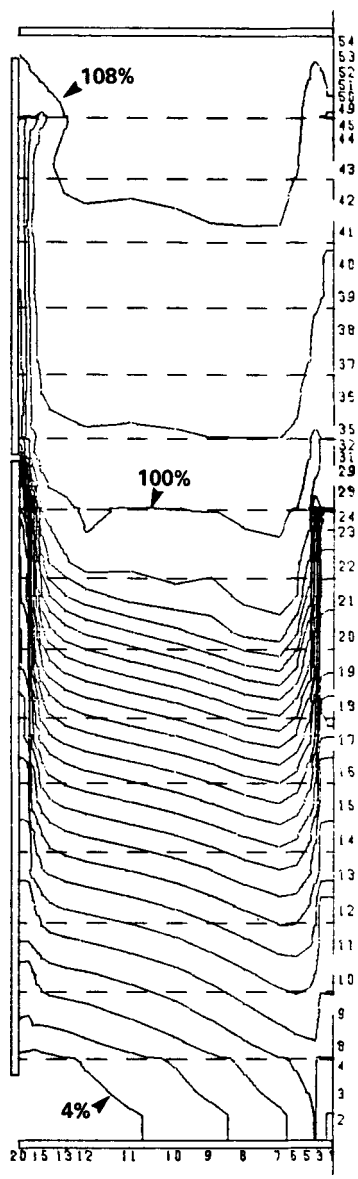

FIGURE B.26 21 RADIAL NODES
(4% QUALITY INCREMENTS)

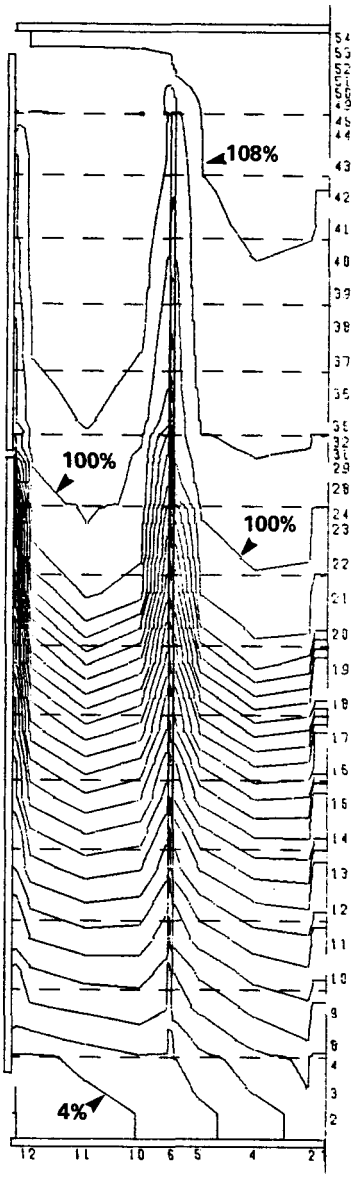

FIGURE B.27 CIRCUMFERENTIAL OPEN LANE NOMINAL RUN (4% QUALITY INCREMENTS)

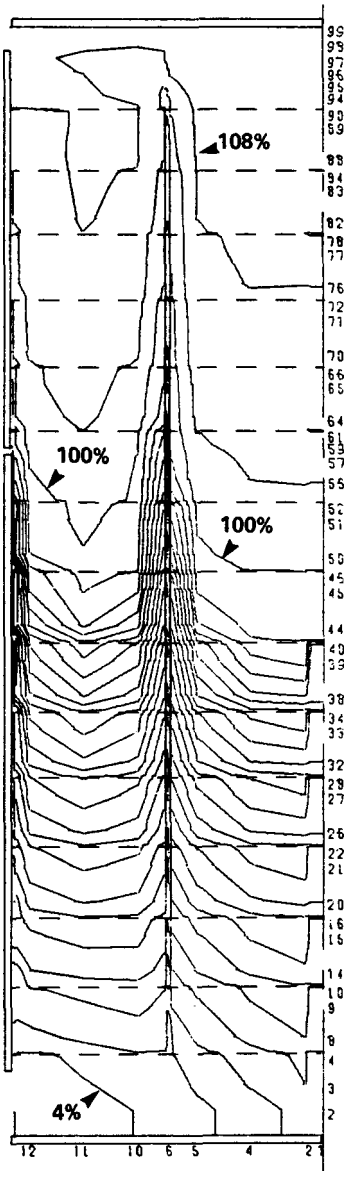

FIGURE B.28 CIRCUMFERENTIAL OPEN LANE WITH 99 NODE FINE TSP MODEL (4% QUALITY INCREMENTS)

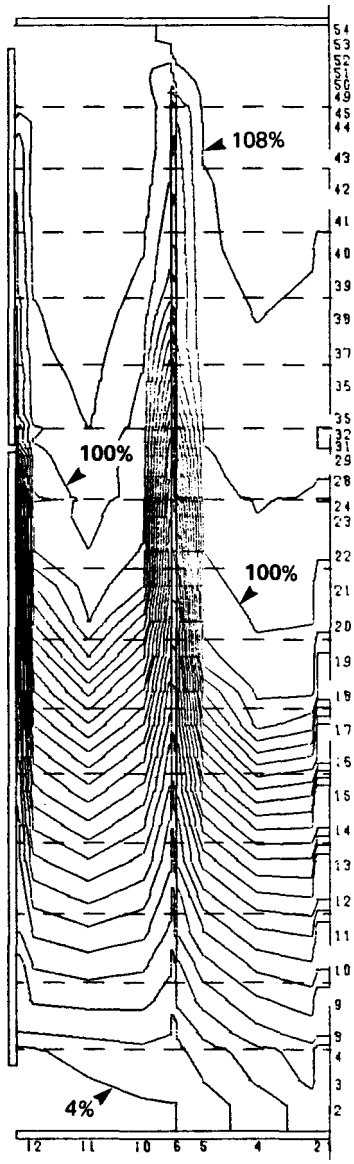

FIGURE B.29 CIRCUMFERENTIAL OPEN LANE WITH HOMOGENEOUS MODEL (4% QUALITY INCREMENTS)

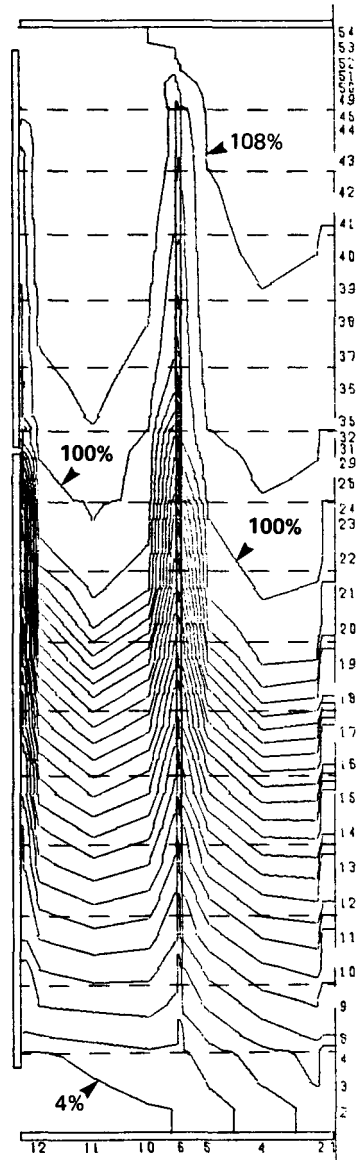

FIGURE B.30 CIRCUMFERENTIAL OPEN LANE WITH ZUBER VOID FRACTION (4% QUALITY INCREMENTS)

Appendix C

THEDA-1 INPUT AND OUTPUT

Appendix C

THEDA-1 INPUT AND OUTPUT

INPUT FILES FOR THEDA-1

Table C.1 shows the listing of the input data file for the THEDA-1 analysis of the TMI-2 OTSG at 100% power. With exception to lines 1 and 2 of the input data file, the remaining lines define two NAMELISTS -- INPUT and VALUES. The format and rules for construction and using the NAMELIST statements can be found in a Fortran IV Language Manual and will not be repeated here. Table C.2 gives a description of the variables, format, and required units for those variables appearing in the data file of Table C.1.

TABLE C.1

SAMPLE INPUT DATA FILE FOR THEDA-1

```
                                                                        LINE
TMI-2 OTSG 55*12*11 100% POWER ..........................................  1

$INPUT
RELAX = 3*0.6, 0.1, 6*0.8,
PRP=2200., PRS=924.9, NDIMEN=3, ITOT=20, ................................  5
TINT=607.5, TFW=466.,
L1=55, M1=12, N1=11,
STFLOW=5.916E06, TUFLOW=68.95E06,
PITCH=0.875, DIA=0.625, THICK=3.8E-2,
IBUPP=4, 7*1, 3, 3, 4*1, 5, NSUP=15, NCHECK=2, ..........................  10
IAXS=6, 10, 12, 14, 16, 18, 20, 22,
    26, 34, 38, 40, 42, 44, 48,
X=0.0, 1.198, 2.396, 3.729, 3.771, 3.896, 3.9375,
  4.654, 6.198, 7.802, 9.427, 11.073, 12.760, 14.406,
  16.042, 17.625, 19.125, 20.708, 22.334, 23.990, 25.677, ...............  15
  27.323, 28.9375, 29.646, 29.6875, 29.8125, 29.854, 30.836,
  31.818, 32.151, 32.484, 32.979, 33.021, 33.146, 33.1875, 33.771,
  35.3125, 36.854, 38.469, 40.031, 41.573, 43.094, 44.594,
  46.073, 47.531, 48.146, 48.1875, 48.3125, 48.354, 48.926,
  49.498, 50.070, 50.642, 51.400, 52.115, ...............................  20
R=0.0, .20, .30, 1.39703, 2.49405, 3.10995, 3.873,
  4.2545, 4.636, 4.876, 4.914, 4.932,
TH=0.0, 0.301, 0.592, 1.108, 3.910, 15., 47.5, 82.5, 117.5,
    150., 180.,
NINLET=2, IB=30, NEXIT=1, ...............................................  25
PRIFAC=12*1.0,
KLANE=3*5, 2*4, 3*3, 4*2,
KINIT=1,
AKSUP(3)=25.3, AKSUP(8)=25.3, AKSUP(9)=417.0,
$ .......................................................................  30
$VALUES
PORX(3,5)=0.69,    TUFAC(3,5)=0.67,
PORX(4,4)=0.77,    TUFAC(4,4)=0.50,
PORX(5,4)=0.56,    TUFAC(5,4)=0.95,
PORX(5,3)=0.95,    TUFAC(5,3)=0.11, .....................................  35
PORX(6,3)=0.75,    TUFAC(6,3)=0.54,
PORX(7,3)=0.66,    TUFAC(7,3)=0.73,
PORX(8,3)=0.56,    TUFAC(8,3)=0.95,
```

TABLE C.2

INPUT DESCRIPTION FOR THEDA–1

Line	Variable	Format	Description	Units
1	HEAD(I)	20A4	Title of analysis; columns 1-80	NA
2	RESTRT	A8	Blank line denotes run is starting from scratch without restart file.	NA
3			INPUT NAMELIST statement. First character in line is blank followed by $INPUT.	NA
4	RELAX	Real	Relaxation factors (used to reduce the change at a given variable from one iteration to the next) for: RELAX(1) axial velocity ∿ 0.4 RELAX(2) radial velocity ∿ 0.4 RELAX(3) circumferential velocity ∿ 0.4 RELAX(4) pressure ∿ 0.1 RELAX(5) secondary enthalpy ∿ 0.6 RELAX(6) primary enthalpy ∿ 0.6 RELAX(7) not used RELAX(8) not used RELAX(9) density ∿ 0.6	None
5	PRP	Real	Primary flow inlet pressure	PSIA
5	PRS	Real	Secondary flow exit pressure	PSIA
5	NDIMEN	Integer	Problem dimension (not used since THEDA-1 has only a 3-D option)	None
5	ITOT	Integer	Total number of iterations desired where 1 iteration sweeps the full length of the OTSG.	None
6	TINT	Real	Primary flow inlet temperature	^{o}F
6	TFW	Real	Feedwater inlet temperature	^{o}F
7	L1	Integer	Number of axial main nodes	None
7	M1	Integer	Number of radial main nodes	None
7	N1	Integer	Number of circumferential main nodes	None
8	STFLOW	Real	Exit secondary flow (steam flow) per steam generator	LBM/HR
8	TUFLOW	Real	Primary flow (tube flow) per steam generator	LBM/HR
9	PITCH	Real	Distance between tube centers	IN
9	DIA	Real	Tube outside diameter	IN
9	THICK	Real	Tube wall thickness	IN

TABLE C.2

INPUT DESCRIPTION FOR THEDA–1 (CONT'D)

Line	Variable	Format	Description	Units
10	ISUPP	Integer	Parameter used to define tube support plate type. Total of NSUP values. ISUPP — Description* 1 — RSP model, peripheral gap open 2 — RSP model, peripheral gap blocked 3 — FGSP model, peripheral gap open 4 — FGSP model, peripheral gap blocked 5 — FGSP model, peripheral gap blocked, drilled only region 6 — FGSP model, peripheral gap blocked, preferentially broached 7 — FGSP model, peripheral gap blocked, circumferential open lane blocked	None
10	NSUP	Integer	Total number of tube support plates in model	None
10	NCHECK	Integer	NCHECK ≠ 0 or 1 prints convergence parameters after each iteration. NCHECK = 0 or 1 bypasses convergence print.	None
11	IAXS	Integer	Axial main node immediately downstream from actual location of TSP for RSP TSP model. Axial main node at upper surface of TSP for FGSP TSP model.	None
13-20	X	Real	Elevation of the L1 axial main nodes	FT
21-22	R	Real	Radial location of the M1 radial main nodes	FT
23-24	TH	Real	Circumferential location of the N1 circumferential main nodes	DEGREES
25	NINLET	Integer	Number of axial main nodes between the lower tubesheet and the top of the inlet port (or the number of radial momentum control volumes at the inlet port)	None
25	IB	Integer	Axial main node located at the bleed port	None
25	NEXIT	Integer	Number of axial main nodes between the upper surface of the shroud and lower surface of the upper tubesheet (or the number of radial momentum control volumes at the exit port)	None

*See Section 5.2 of the main body of this report for a discussion of the RSP and FGSP models.

TABLE C.2

INPUT DESCRIPTION FOR THEDA-1 (CONT'D)

Line	Variable	Format	Description	Units
26	PRIFAC	Real	Weight factor applied at each of the M1 radial main nodes to define a radial distribution of the primary flow. (NOTE: The integrated average value for PRIFAC does not have to equal 1.0. The code computes the radial flow distribution for each control volume so that total primary flow equals TUFLOW.)	
27	KLANE	Integer	M1 values (one for each radial node) denoting the circumferential nodes in which the main control volumes are located totally or partially in the lane. If control volumes are only partially in the lane, then data should appear in VALUES NAMELIST defining PORX (porosity) and TUFAC (both of which are defined in VALUES).	None
28	KINIT	Integer	Parameter used to call subroutine INIT to set up porosity field and/or change TINT. KINIT = 1 calls subroutine INIT KINIT = 0 bypasses INIT	
29	AKSUP	Real	Support plate resistance factor dependent upon TSP geometry and TSP model (RSP or FGSP) $AKSUP \equiv \frac{\Delta P\ g_c}{1/2\rho\ U\|U\|}$ AKSUP(1) TSP with tubes: RSP model — Default 4.178 AKSUP(2) TSP with no tubes: RSP model — Default 0.500 AKSUP(3) Outer periphery tube free: RSP model — Default 25.3 AKSUP(4) TSP with tubes: FGSP model — Default 0.846 AKSUP(5) TSP with no tubes: FGSP model — Default 0.257 AKSUP(6) Inner pref. broaching, FGSP model — Default 0.846 AKSUP(7) Outer pref. broaching, FGSP model — Default 1.337 AKSUP(8) Untubed TSP periphery: RSP model — Default 25.3 AKSUP(9) Untubed bundle centerline region: RSP model — Default 417.0	None
30			End of INPUT NAMELIST	

TABLE C.2

INPUT DESCRIPTION FOR THEDA–1 (CONT'D)

Line	Variable	Format	Description	Units
31			VALUES NAMELIST statement. VALUES is read only if KINIT=1 and allows the user to override any of the following field variables at any i, j, k node:	NA
			• axial, radial, and circumferential velocities (U,V,W)	FT/SEC
			• pressure ($P = (P_L^* - PRS) \times 144 \times 32.2$)	LBM/FT-SEC^2
			• primary and secondary enthalpies (HT,HS)	BTU/LBM
			• porosity (POROS)	None
			• mixing coefficient (GAM)	LBM/FT^2-SEC
			• density (RHO)	LBM/FT^3
			• heat flux (FLX)	BTU/HR-FT^2
			• secondary quality (QLTY)	None
			• TUFAC which defines the percentage of a control volume that is tubed. $TUFAC = \frac{1 - POROS}{1 - POROST}$ POROST = tube bundle porosity POROS = control volume porosity	None
32-38	PORX	Real	Defines J,K porosity values at an axial plane that does not include a TSP.	None
32-38	TUFAC	Real	See line 31 description.	None
39			End of VALUES NAMELIST	

*P_L = local static pressure (psia)

TABLE C.2

INPUT DESCRIPTION FOR THEDA–1 (CONT'D)

Line	Variable	Format	Description	Default	Units
			Following are variables in the INPUT NAMELIST not appearing in the sample data file used in THEDA-1.		
	ISUP	Integer	ISUP = ISUPP + 1 Used to change support plate type during RESTART.		None
	KPRINT	Integer	Parameter for output control KPRINT = 0 Prints variables at all I & J, but only K = 2 and N1-1. KPRINT = 1 Prints variables at all I, J, K.	0	None
	QDNB	Real	Dryout quality	0.95	None
	TUBES	Real	Number of tubes in OTSG. Used only for initial estimate of boiling length in bundle.	15400	None
	UBOIL	Real	Overall heat transfer coefficient in boiling regime. Used only for initial estimate to calculate boiling length.	1600	BTU/HR-FT^2-°F
	UCONV	Real	Overall heat transfer coefficient in superheat heat transfer regime. Used only for initial estimate of the heat flux.	200	BTU/HR-FT^2-°F

OUTPUT DESCRIPTION

The output from THEDA-1 is divided into three areas and includes:

- Listing of the variables and values assigned to each in the INPUT NAMELIST
- Output of convergence parameters, secondary axial velocity and enthalpy at the L1/2 axial node elevation, and heat balance between primary and secondary fluids
- Final output listing of the overall steam generator performance and the thermal/hydraulic variables of the primary and secondary flows

The following discussion will describe the output in detail:

INPUT NAMELIST

A listing of the user's input, defined in the INPUT NAMELIST, is provided for each job submitted. Table C.1 shows a sample of the INPUT NAMELIST and the variables contained within.

OUTPUT FOR EACH ITERATION

Table C.3 shows the output for iterations 290, 291, and 292 from the TMI-2 OTSG run at 100% power. The definitions of the output, labeled A-U, are given in the following listing:

Label	Variable	Description	Units
A	ITER	Current iteration	None
B	SRMAX	[SRMAX/STFLOW*] where SRMAX is the largest continuity residual for all control volumes	None
C	SRSUM	[SRSUM/STFLOW/Number of control volumes] where SRSUM is the summation over all control volumes of the absolute value of the continuity residual for each control volume	None

*Defined in input file as the exit steam flow per steam generator.

Label	Variable	Description	Units
D	U1(L1/2,M1/2,N1/2)	Secondary flow axial velocity for node L1/2,M1/2,N1/2	FT/SEC
E	HS(L1/2,M1/2,N1/2)	Secondary flow enthalpy for node L1/2,M1/2,N1/2	BTU/LBM
F	QPRIM	$\dot{m}_t \ (h_{in} - \overset{\sim t}{h}_{ex})$	BTU/HR
G	QSEC	$\dot{m}_{FW} \ (\overset{\sim s}{h}_{ex} - h_{FW})$	BTU/HR
H	DELQ	$100 \left\lvert \frac{QSEC-QPRIM}{QSEC} \right\rvert$	None
I	RSMAX(1)	Maximum U-momentum residual of all control volumes normalized by the exit momentum	
J	RSSUM(1)	Summation over all control volumes of the U-momentum residuals divided by the total number of control volumes and normalized with respect to the exit steam momentum	None
K	RSMAX(2)	Same as I for V-momentum	None
L	RSSUM(2)	Same as J for V-momentum	None
M	RSMAX(3)	Same as I for W-momentum	None
N	RSSUM(3)	Same as J for W-momentum	None
O	FLOIN	Feedwater flow per one-half of the OTSG	LBM/SEC
P	FLOBLD	Bleed flow per one-half of the OTSG	LBM/SEC
Q	FLOEX	Exit steam flow per one-half of the OTSG	LBM/SEC
R	FACTX(1)	Not used since multiple exit planes are not allowed	None
S	FACTRX	Factor applied to the exit plane velocity profile so that global continuity is identically satisfied	None
T	SRPL	Summation of the net continuity residual across an entire plane of the modeled OTSG	LBM/SEC
U	III,JJJ,KKK	I,J,K node of SRMAX	None

TABLE C.3

TYPICAL OUTPUT AFTER EACH ITERATION

This output was generated by setting NCHECK equal to 2. For NCHECK equal to 0 or 1, labels I thru M would have been omitted except for the last iteration of the run.

OUTPUT AFTER LAST ITERATION

Table C.4 shows a portion of the output following the TMI-2 100% power run. The listing of overall performance parameters and water inventory is printed. The output that follows these preliminary prints gives a listing of the primary and secondary flow variables at all I,J nodes. Circumferential nodes (K) are controlled by the KPRINT parameter:

KPRINT = 0: first and last circumferential values for each variable are listed

KPRINT = 1: all circumferential values for each variable are listed

The variables that are printed and the order in which each appears in the output is summarized below:

Secondary axial velocity	(FT/SEC)
Secondary radial velocity	(FT/SEC)
Secondary circumferential velocity	(FT/SEC)
Secondary axial mass flux	(LBM/SEC-FT^2)
Secondary radial mass flux	(LBM/SEC-FT^2)
Secondary flow enthalpy	(BTU/LBM)
Secondary flow temperature	(°F)
Primary flow temperature	(°F)
Secondary tube wall temperature	(°F)
Secondary flow quality	
Secondary flow density	(LBM/FT^3)
Relative secondary pressure	(PSI)
Local heat flux	(BTU/HR-FT^2)
Overall heat transfer coefficient	(BTU/HR-FT^2-F)

TABLE C.4

FINAL OUTPUT AFTER LAST ITERATION

OVERALL PERFORMANCE OF THE STEAM GENERATOR

STEAM FLOW RATE = 5.916E+06 LB/HR

BLEED FLOW RATE = 9.459E+05 LB/HR

FEEDWATER TEMPERATURE = 4.660E+02 F

STEAM PRESSURE = 9.249E+02 PSIA

SECONDARY EXIT TEMPERATURE = 5.932E+02 F

SECONDARY EXIT SUPERHEAT = 5.800E+01 F

SECONDARY EXIT ENTHALPY = 1.252E+03 BTU/LBM

SECONDARY EXIT QUALITY = 1.085E+02 PER CENT

PRIMARY FLOW RATE = 6.895E+07 LB/HR

PRIMARY PRESSURE = 2.200E+03 PSIA

PRIMARY EXIT TEMPERATURE = 5.569E+02 F

PRIMARY EXIT ENTHALPY = 5.558E+02 BTU/LBM

PRIMARY EXIT FLOW (CALC) = 6.895E+07 LBM/HR

PRIMARY INLET TEMPERATURE = 6.075E+02 F

PRIMARY AVERAGE TEMPERATURE = 5.822E+02 F

WATER INVENTORY

VOLUME OF GENERATOR = 2.268E+03 CU FT

TOTAL WATER MASS = 1.332E+04 LBM

AXIAL VELOCITY FT/SEC

K = 2

J	I = 2	3	4	5	6	7	8	9	10	11	12	13
11	0.	-3.15E-02	-6.44E-01	-1.47E+00	-4.55E-08	6.69E-08	3.56E+00	3.47E+00	1.86E+00	1.91E+00	2.82E+00	2.79E+00
10	0.	-1.49E-01	2.73E-01	4.26E-01	1.23E-08	-2.85E-08	1.60E+00	3.44E-01	1.07E+00	3.25E-01	2.11E+00	2.26E+00
9	0.	-1.37E-01	4.01E-01	1.72E+00	2.85E+00	2.44E+00	1.60E+00	-4.41E-01	2.62E+00	9.14E-01	5.12E+00	3.48E+00
8	0.	-1.78E-01	3.92E-01	2.04E+00	3.19E+00	2.71E+00	1.62E+00	-2.37E-01	3.11E+00	1.45E+00	5.27E+00	3.61E+00
7	0.	-3.12E-01	3.52E-01	2.29E+00	3.69E+00	3.10E+00	1.84E+00	-6.41E-02	3.53E+00	1.81E+00	5.51E+00	3.74E+00
6	0.	-8.18E-01	1.73E-02	2.70E+00	4.56E+00	3.80E+00	2.33E+00	2.49E-01	3.95E+00	2.10E+00	6.00E+00	4.11E+00
5	0.	-1.50E+00	-1.20E-01	3.33E+00	5.74E+00	4.81E+00	3.35E+00	4.51E+00	4.56E+00	2.63E+00	6.73E+00	4.74E+00
4	0.	-2.19E+00	-2.66E-01	4.29E+00	7.43E+00	6.23E+00	4.60E+00	2.87E+00	5.78E+00	3.62E+00	7.60E+00	5.36E+00
3	0.	-2.74E+00	5.95E-01	5.62E+00	9.78E+00	8.20E+00	5.83E+00	3.87E+00	7.71E+00	5.37E+00	9.69E+00	7.00E+00
2	0.	-2.69E+00	2.00E+00	1.47E+00	5.02E-09	-3.39E-06	3.08E+00	2.09E+00	6.22E-01	3.86E+00	8.41E-01	5.42E+00

J	I = 14	15	16	17	18	19	20	21	22	23	24	25
11	2.77E+00	5.38E+00	3.99E+00	6.85E+00	4.97E+00	7.63E+00	6.40E+00	1.09E+01	7.91E+00	1.16E+01	1.32E+01	1.85E+01
10	2.51E+00	3.06E+00	2.97E+00	3.64E+00	3.69E+00	4.94E+00	4.92E+00	9.79E+00	6.46E+00	1.21E+01	1.37E+01	1.16E+01

LIMITATIONS AND MACHINE REQUIREMENTS

- The program language is Fortran.
- A maximum of 9126 main nodes is allowed without exceeding the small and large core capacity of B&W's CDC 7600. The required field length is:

  Small Core Field Length -- 102365 Octal words

  Large Core Field Length -- 324500 Octal words

- The steam table routines used in THEDA-1 are identical to those used in certified B&W computer codes. The steam table routines are valid over the following range:

  Temperature -- 35° - 665°F

  Pressure -- 600 - 2600 psia

- A disc file is required for storage of the restart data which contains the field variables and other variables stored in the program common blocks.
- Re-dimensioning of the program is accomplished by the editing of the appropriate common blocks.